DESIGN, MICROFABRICATION, AND TESTING OF ALL-PMMA, NANOPORE-BASED ELECTROPHORETIC FLOW DETECTORS FOR BIOMEDICAL APPLICATIONS

A Thesis Submitted to the

College of Graduate Studies and Research

in Partial Fulfillment of the Requirements for the Degree of

Doctor of Philosophy

in the Department of Electrical and Computer Engineering

University of Saskatchewan

Saskatoon, Saskatchewan

by

MANOUCHEHR HASHEMI

PERMISSION TO USE

In presenting this thesis in partial fulfillment of the requirements for a Postgraduate degree from the University of Saskatchewan, I agree that the Libraries of this University may make it freely available for inspection. I further agree that permission for copying of this thesis in any manner, in whole or in part, for scholarly purposes may be granted by the professor or professors who supervised my thesis work or, in their absence, by the Head of the Department or the Dean of the College in which my thesis work was done. It is understood that any copying or publication or use of this thesis or parts thereof for financial gain shall not be allowed without my written permission. It is also understood that due recognition shall be given to me and to the University of Saskatchewan in any scholarly use which may be made of any material in my thesis.

Requests for permission to copy or to make other use of material in this thesis in whole or in part should be addressed to:

Head of the Department of Electrical and Computer Engineering

University of Saskatchewan

3B48 Engineering Building

57 Campus Drive, Saskatoon, SK

S7N 5A9

ABSTRACT

Detection of and discrimination between different nanoparticles and biomolecules are vital steps in analytical, biochemical, and diagnostic biomedical procedures used in life sciences. Synthetic micro/nanopores in solid-state membranes form an emerging class of single-molecule detectors capable of detecting and probing the properties of particles and biomolecules with high throughput and resolution: The particles or biomolecules to be analyzed are added to an electrolyte solution in one of the two reservoirs of the detector system separated by a thin membrane containing a single micro/nanopore. An outer electric field induces an open-pore ionic current (I_{open}) through the pore, dragging the particles with itself. Transient changes occur when a particle slightly smaller than the pore translocates through the pore. This electrical signal can be analyzed to derive information regarding to the particle or biomolecule size and even its morphology, concentration in the solution, and the affinity for the pore. Many detectors are based on self-assembled, naturally occurring protein pores in lipid bilayer membranes. Most solid-state pore-based detectors reported in literature use artificial pores in silicon nitride or silicon oxide membranes. Applying polymers as a membrane potentially offers advantages over the aforementioned types, including good electrical insulation, improved wettability thanks to higher hydrophilicity, and long-term stable yet low-cost and disposable devices. The present study aims at exploiting such advantages by developing the proof-of-concept for a single-material, all-polymer, nanopore detector allowing the continuous variation of target pore size in the range from micrometers to a few nanometers for best pore size adaption to the biomolecules to be investigated. The research comprises materials selection, system design, development of a fabrication and assembly sequence, device fabrication, and functional device testing. Poly

(methyl methacrylate) (PMMA) was selected as it combines advantageous microfluidic properties know from competing materials, such as polyimide, polystyrene, polycarbonate, or polyethylene terephthalate, with outstanding micropatterning capabilities. The membrane thickness is set to be 1 µm, based on a compromise between robustness during fabrication and operation on one side, and electrochemical performance on the other. After spincoating the membrane onto a sacrificial wafer, pores with diameters of typically several hundred nanometers are patterned by electron beam lithography. In combination with thermal post processing leading to polymer reflow, diameters one order of magnitude smaller can be achieved. The present study focuses on 450 nm and 22 nm pores, respectively. Besides these pores fabricated in a top-down approach, self-assembled α-hemolysin protein pores of 1.5 nm diameter are integrated in a combined top-down and bottom-up approach so that single digit, double digit, and triple digit nanometer pores are available. Systems integration is achieved by capillary-forced based release from the sacrificial substrate and the application of UV-initiated glue.

Test sequences proved and qualified the device functionality: Electrical characterization was performed in aqueous KCl electrolyte solution. The devices exhibit a stable, time-independent ionic current. The current-voltage curves are linear and scale with the electrolyte concentration. System verification was performed using silica nanospheres of 100 nm and 150 nm diameter as known test particles. Translocation through a 450 nm pore induced current blockades for about 1 ms with an amplitude of 30 pA to 55 pA for 100 nm particles and in excess of 70 pA for 150 nm particles. This is in close agreement with results obtained by a mathematical model used in this study. Biomolecules relevant to many life science applications, *double-stranded DNA* (dsDNA) and *bovine serum albumin* (BSA) were subsequently analyzed to prove the device concept. Post-processed pores of 22 nm diameter were used at 600 mV driving voltage and

0.1 molar electrolyte in a slightly acidic regime of pH = 6. Typical current blockade amplitudes for complete translocations of dsDNA are $I_{block} = 22\ pA$ for a translocation time of $t_D = 0.2\ ms$, and an almost threefold current blockade ($I_{block} = 60\ pA$) for the larger BSA molecules, respectively. The results demonstrate that the PMMA-based nanopores are sensitive enough to not only detect translocating biomolecules, but to also sense them by distinguishing between different biomolecules.

The molecule-specific and distinct translocation signals through the pores using both, standardized silica nanoparticles and biomolecules of different dimensions, prove the concept of an all-PMMA electrophoretic flow detector with adjustable pore diameters. Devices with pore diameters covering three orders of magnitude in the nanometer range were successfully built, tested, and characterized. The results suggest such detectors are promising candidates for biomolecule detecting applications.

ACKNOWLEDGMENTS

First of all, I am greatly indebted to my supervisor, Dr. Sven Achenbach, for his constant support, great guidance, valuable suggestions, and encouragements extended throughout the course of my study, without which this thesis would not have been possible. His mentorship and support had a great impact on both my study and life, and made my past years a very special time.

I would like to take this opportunity to express my gratitude to my committee members Dr. David Klymyshyn, Dr. Anh van Dinh, Dr. Li Chen, and Dr. Kevin Stanley for their support, time and consideration in reading my thesis, and for their advice in defining and completing my thesis.

I also sincerely thank the support and assistance provided by Garth Wells during my detector device fabrication and experimentation period at TRTechs and the Synchrotron Laboratory for Micro and Nano Devices (SyLMAND) at the Canadian Light Source (CLS). I would like to appreciate all the personnel of the Edmonton NanoFAB Lab at the University of Alberta in Canada, as well as the personnel of the Institute for Microstructure Technology (IMT) at the Karlsruhe Institute for Technology (KIT) in Karlsruhe, Germany, for their contributions towards making the fabrication of my polymer-based electrophoretic flow detector device possible.

I acknowledge the financial assistance for this project provided by the Natural Sciences and Engineering Research Council of Canada (NSERC) and TRTechs. I also appreciate the Travel grant provided by the College of Engineering, Department of Electrical Engineering and Computer Science at the University of Saskatchewan (U of S), as it provided me a wonderful experience and enhanced my graduate knowledge immensely.

Last, but not least, I would like to thank my family for being always there for me. In particular, I appreciate my wife, Banafsheh Moazed and my son, Arian, for their kind support, love, patience, understanding, and self-sacrifice. Special thanks go to my parents, Ashraf and Abolhassan, who deserve a very special mention. Finally, I would like to thank my sisters, Farahnaz, Farzaneh, and Raheleh for their patience, understanding, and encouragements during my program of study.

TABLE OF CONTENTS

LIST OF FIGURES

LIST OF TABLES

LIST OF ABBREVIATIONS

A	adenine
AFM	atomic force microscopy
BioMEMS	biomedical micro-electro-mechanical systems
βLGa	β-lactoglobulin
BS	bovine serum albumin
C	cytosine
Cis	negatively charged electrolyte detector reservoir
CAD	computer aided design
DNA	deoxy-ribonucleic acid
Cl^-	chloride ion
dsDNA	double-stranded DNA
EBL	electron beam lithography
HPr	histidine-containing phosphocarrier
EOF	electroosmotic flow
FEM	finite element method
G	guanosine
HF	hydrofluoric acid
IBL	ion beam lithography
K^+	potasium ion
kbp	kilo base pairs
KCl	potassium chloride

KOH	potassium hydroxide
M	molar
MBP	maltose-binding protein
MEMS	micro-electro-mechanical systems
MIBK-IPA	methyl isobutyl keton and isopropanol alcohol
PC	polycarbonate
PC	personal computer
PCR	polymerase chain reaction
PET	polyethylene trephthalate
pH	negative decadic logarithm of the hydrogen ion activity a_{H+}
PI	polyimide
pI	isoelectronic point
pK_a	negative decadic logarithm of the acid dissociation constant K_a
PMMA	poly (methyl methacrylate)
RNA	ribonucleic acid
SEM	scanning electron microscopy
Si	silicon
Si_3N_4	silicon nitride
SiO_2	silicon oxide
ssDNA	single-stranded DNA
T	thymine
TEM	transmission electron microscopy
T_g	glass transition temperature

Ti	titanium
Trans	positively charged electrolyte detector reservoir
UV	ultraviolet
XRL	X-ray lithography
2D	two dimensional

LIST OF VARIABLES

A	pore cross section
D	sphere diameter
dV/dt	acceleration
D	pore diameter
D_m	cross section of the pore equal to the maximum bulge
$D_{(z)}$	cross section of an electric field streamline in a pore
E_z	electric field along z axis
F_D	viscose drag force
F_E	electro osmotic force
F_R	random drag force
G	Gibbs free energy
H	electrolyte head
I	current through the pore
I_{block}	ionic current reduction or blockade
I_{open}	open-pore ionic current
K	electrolyte specific conductivity
K'	constant based on voltage and electrolyte resistance
L	pore length
M	molecule mass
M_W	molecular weight
P	head pressure

P'	uniaxial tension
R_p	pore resistance
R	pore radius
R_1	pore resistance without sphere
R_2	pore resistance with sphere
ΔR	increase in resistance
t_D	translocation time
V	potential across the pore
V'	Volume
X	distance from the central axis
Z	axis along pore length
ρ_{eff}	electrolyte effective resistivity
ρ'	electrolyte resistivity
ρ	density
γ	surface energy density
θ	angle measured from z axis
w/v	percentage of surfactant weight per volume of electrolyte
σ_v	Von Mises stress
$\sigma_{1,2,3}$	stress along x, y, z axes

1. Introduction

1.1. Motivation

Cells are fundamental units of all living organisms. Any living organism is the result of cell proliferation and cell differentiation processes. Biomolecules are molecules that are produced by the cells of living organisms. *Nucleic acids* (*deoxy-ribonucleic acid* (DNA) and *ribonucleic acid* (RNA)) and *proteins* are two major classes of biomolecules. Deviations in the concentration of specific cells and biomolecules within the cells, as well as structural and functional changes from normal values, have shown to be closely linked to many diseases and disorders in animals and the human body. Therefore, accurate detection, counting, and structural characterization of various cells and biomolecules have always been crucial steps for biomedical scientists and clinicians in order to be able to precisely diagnose diseases, discover and/or develop new drugs, conceive proper treatments, or even prevent different human diseases and disorders.

Nowadays, several conventional methods are widely used in clinical and molecular biology laboratories for detection and counting cells and biomolecules and to electrochemically interact with them. These methods are, however, prone to human error. More importantly, they are not able to concurrently provide scientists and clinicians all the necessary information regarding detection, counting, as well as structural analysis of specific cells and biomolecules. The available methods are also very time-consuming, and usually need lots of preparation or require to be complemented by other lengthy and complex techniques prior to the actual detection and counting process. DNA, for instance, usually needs to be amplified using a *polymerase chain reaction* (PCR) process, before it can be detected by *Gel Electrophoresis* in the laboratory.

The complicated, lengthy, and often two-step conventional detection and counting processes, therefore, give rise to world-wide research interest in the development of new techniques which are faster, more reliable, more accurate, and more sensitive. Some of these research endeavours have already led to commercialized patch clamp detector systems, including those of Nanion (Munich, Germany), Ionera (Freiburg, Germany), or Sophion (Copenhagen, Denmark). The research presented here develops and studies miniaturized, sensitive, easily applied, potentially reusable devices. The focus is to provide the proof-of-concept for a single-material, all-polymer detector which allows to directly detect, and potentially analyze, different cells and biomolecules of interest without performing any lengthy procedures and preparations before the actual detection and counting process can be conducted.

1.2. Overview of DNA and Protein Structures

Deoxy-ribonucleic acid (DNA) is a biomolecule that carries all the genetic information used in the development and function of a living organism. DNA is formed from subunits called *nucleotides*. Four different types of nucleotide make up the entire DNA molecule within the cells: *Adenine* (A), *Thymine* (T), *Guanine* (G), and *Cytosine* (C). DNA molecules are naturally occurring as *double-stranded* (dsDNA) molecules with two complementary nucleotide strands twisting around each other in the form of a double-helix structure. In this context, Adenine and Thymine are considered complementary, as are Guanine and Cytosine. In a dsDNA molecule, Guanine in one strand therefore always pairs with Cytosine as the complementary nucleotide in the other strand, and Adenine in one strand always pairs with Thymine in the other strand (Figure 1.1). The genetic information is encoded by the exact sequence of the allowed nucleotide pairs. Within a human cell, the entire dsDNA molecule comprises about $6 \cdot 10^9$ of these

nucleotide pairs, also referred to as *base pairs*. In terms of physical size, a dsDNA molecule has a diameter of approximately 2.0 nm.

The twisted DNA double-helix molecules can twist even more like a rope in a process called *DNA super-coiling*. The twists can occur in the direction of the helix, holding nucleotides more tightly together, or can occur in the opposite direction, making nucleotides more apart from each other. DNA double-helix molecules can exist in many alternative molecular or structural arrangements called *conformations*, depending not only on the amount and direction of super-coiling, but also on the level of hydration, DNA nucleotide sequences themselves, chemical modifications of individual nucleotides, and the type and concentration of metal ions in the solution in which they are maintained [1, 2]. DNA molecules, in any possible conformation, can also fold back on themselves to form an array of two- and three-dimensional scaffold nano-structures [3].

dsDNA molecules are usually overall linearly arranged and have two free ends. Besides, dsDNA molecules may also occur as circular molecules without free ends. *Plasmids*, for example, are usually small circular dsDNA molecules that are most commonly found in bacterial cells. The molecular size of plasmid molecules vary from 1 to over 1,000 kilo-base pairs (kbp) in length.

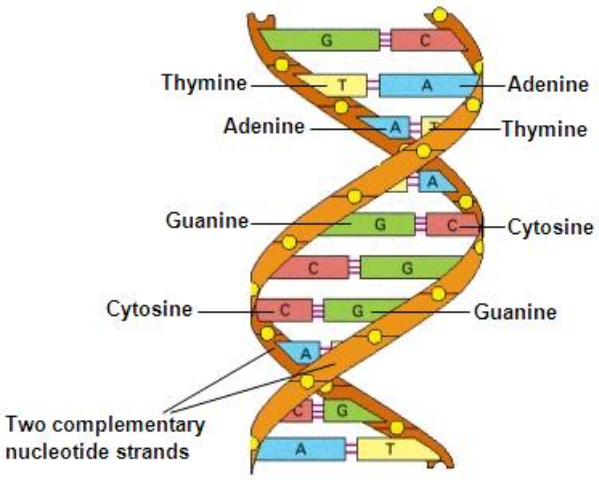

Figure 1.1: Schematic of the double-helical structure of double-stranded deoxy-ribonucleic acid (dsDNA): Excerpt of a single dsDNA molecule highlighting the two backbones and the four types of nucleotide subunits (A, T, C, G) connecting the backbones, as well as a potential sequence based on complementary nucleotide pairs [4].

Proteins, another major class of biomolecules, are also an essential part of any living organism. They participate in every process within living cells, including structural or mechanical functions, metabolism, cell cycle, cell adhesion, and immune response. Proteins are formed by various combinations of 20 different subunits called *amino acids* that are held together in a linear sequence by *peptide bonds*. Individual amino acids are all composed of a carboxyl group (-COOH) and an amino group ($-NH_2$) bound to a central carbon atom. A hydrogen atom occupies the third bonding site of the carbon atom, and a variable side chain called the *R group* occupies the fourth bonding site. The R group is specific to each amino acid. The peptide bonds form between the carboxyl group of one amino acid and the amino group of the next, resulting in an amino group at one far end of the protein, and a carboxyl group at the

other far end (Figure 1.2). Proteins range in size from tens to several thousand amino acid subunits. Their physical size of 1 nm to 100 nm in diameter classifies proteins as nanoparticles [5]. Proteins usually form into one or more specific structural arrangements or *spatial conformations*, involving complex *folding* processes driven by a number of non-covalent interactions such as hydrogen bonding, ionic interactions, and hydrophobic packing. Folding is an essential process for proteins, by which a protein structure gains its biological functional ability. Proteins may undergo reversible structural changes in performing their biological functions. The transitions between different structural arrangements are called conformational changes.

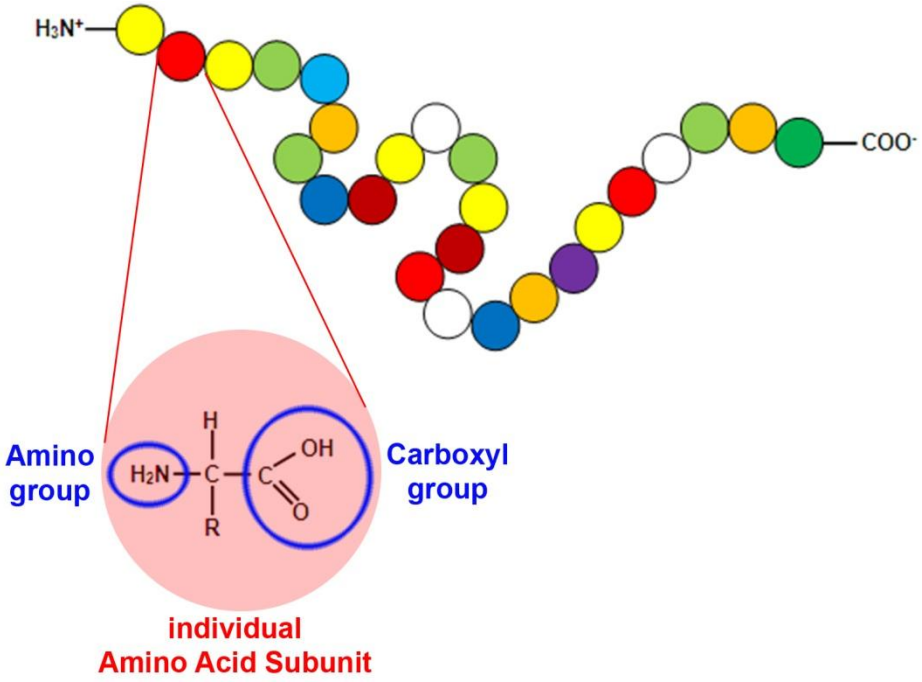

Figure 1.2: Schematic of the structure of a protein molecule: Sequence of individual amino acid subunits, each represented as a colored circle. Each amino acid subunit consists of a central

carbon atom with an amino group, a carboxyl group, a hydrogen atom, and a side chain *R* specific to each amino acid.

1.3. Review of Conventional Detection Methods for Cells and Biomolecules

Conventional methods for detection and counting specific cells and biomolecules are classified into two categories: manual methods, which do not require any special equipment, and equipment-based methods, which rely on specialized electronic devices. Subsequently, some of the manual and equipment-based methods that are most widely used in clinical and molecular biology laboratories are described.

Manual methods are based on optical microscopy of a sample. Through these methods, cells are detected and manually counted by looking directly at a sample through a microscope. Detection and Counting cells through these methods take a long time, and their efficiency is dependent on the resolution and magnification power of the microscope.

- *Homocytometer*, also known as counting chamber invented by Louis-Charles Malassez, is a microscope slide that is especially designed to enable manual counting of non-adherent cells suspended in a proper solution. The slide has a sink in its middle, the area of which is marked with a grid. A drop of a solution containing suspended non-adherent cells is placed in the sink. Looking at the sample under an optical microscope, the number of cells in a certain area is manually counted using the grid. Homocytometers are cheap, and the method is relatively fast as no sample preparation is needed. However, cell counting is practically only feasible at small absolute numbers of cells in the sample. Therefore, the cell solution to be evaluated usually needs to be diluted prior to the actual counting process otherwise the high number of cells would make counting impossible and susceptible to

error. The need for dilution is a disadvantage, as every dilution adds inaccuracy to the measurement.

- *Plating* became a common laboratory technique in the mid-1905 that enables detection and counting of the number of adherent cells in a cell culture plate. Adherent cells are first plated on a cell culture plate where they are kept so that they start to adhere and then grow in a cell growth medium. Only then can they be detected and manually counted under an optical microscope. Plating is the slowest method of detection and counting, as most cells need at least 12 hours to adhere and grow in a cell culture plate.

Equipment-based methods usually exploit physicochemical characteristics of cells and biomolecules to be detected. Using such methods, specific cells and biomolecules can be detected and counted, for instance, by measuring the amount of light that they absorb or reflect when they are labelled with specific fluorescent dyes. Detection through these methods usually needs time-consuming sample preparation steps and therefore takes a long time.

- *Spectrophotometry*, involving the use of spectrophotometers invented by Arnold J. Beckman in 1940, is a method to determine the concentration of specific cells and biomolecules in a sample solution (their abundance in given volume of a solution) by measuring the amount of light absorption (absorbance). DNA, for instance, absorbs ultraviolet (UV) light at the wavelength of 260 nm. In a spectrophotometer, a sample solution containing DNA molecules is exposed to UV light at 260 nm, and a detector measures the light that is absorbed by the molecules. The more UV light gets absorbed, the higher is the DNA concentration in the sample solution: Using the Beer–Lambert law, it is possible to correlate the amount of light absorbed to the concentration of DNA molecules.

For instance, an absorbance of 1, at a UV wavelength of 260 nm, corresponds to a concentration of 50 µg/ml of dsDNA. Spectrophotometers are the fastest, and the most straightforward electrical devices used for detection and 'counting' cells and biomolecules. They have, however, a limited accuracy: When measuring concentration of dsDNA molecules in a solution, for example, the amount of absorbance measured should be within the range of 0.1 to 1 in order for the numbers to be reliable.

- *DNA Gel Electrophoresis* invented by Fred Sanger in 1975 is another method to detect and estimate the amount and concentration of specific DNA molecules in a sample solution. To use this method, a horizontal gel electrophoresis tank with an external power supply and an appropriate buffer along with a DNA-binding dye are required. A sample solution containing DNA molecules is loaded into a well of the gel and is then exposed to an electric field. The negatively-charged DNA molecules move toward the anode and, as smaller molecules move faster, the DNA molecules migrate on the gel depending on their size. In order to visualize specific DNA molecules in the gel, a staining step with a DNA-binding dye is required. In addition, to use this method, specific DNA molecules usually need to be first amplified by a *polymerase chain reaction* (PCR) process before they can be detected on the gel, as 50 ng is the minimum amount of DNA that can be visualized on a DNA gel.
- *Flow Cytometry*, involving the use of flow cytometers developed by Wolfgang Gohde in 1968, is a laser-based technology employed not only in detecting and counting the cells and biomolecules, but also in their structural characterization. In a flow cytometer, cells and biomolecules to be detected flow in a narrow stream in front of a laser beam. The beam hits the cells and biomolecules one by one, and a light detector picks up the light that

is reflected from each individual cell and biomolecule. Flow cytometry is by far the most sophisticated and expensive method for cell and biomolecule detection, counting, and characterization. Flow cytometers generally involve complex optical, fluidic, and electronic components. For precise measurements, the quality of sample preparation and the design of the optical, electrical, and fluidic components of the flow cytometer are very important.

1.4. Review of Pore-Based Detection Methods for Cells and Biomolecules

1.4.1. Coulter Counter

The original *Coulter counter* device was first introduced by Wallace Coulter in 1953 [6]. The device was developed mainly for the purpose of counting blood cells. A schematic representation of the device and its working principle is illustrated in Figure 1.3: The set up consists of an aperture of 100 µm diameter in a glass tube filled with a conducting electrolyte solution. When a voltage is applied across two electrodes positioned in the electrolyte on either side of the aperture, an electric current gets established dependent on the electrolyte conductivity. The aperture introduces only a small additional resistance. The blood cells to be counted are added to the electrolyte solution on one side. The cells are naturally covered by a lipid bi-layer membrane. This is a thin membrane, made of two layers of lipid molecules, that forms a continuous barrier around the cell. While the membrane is intact, it effectively isolates the contents of the cell from the surrounding conducting electrolyte. The cell can therefore be regarded as a highly resistive sphere. When it eventually passes through the aperture, this highly resistive sphere displaces the conducting electrolyte in the aperture by an amount equal to its volume, increasing the resistance of the aperture. The increase in the resistance of the aperture is known as a *resistive-pulse*, which can be detected by instrumentation circuits and be analyzed by a computer. Since the amount of

electrolyte displaced by a cell in the aperture depends on its size, differently-sized cells produce different increases in the resistance of the aperture or, in other words, produce different resistive-pulses with different amplitudes. The number of observed resistive-pulses is proportional to the cell number in the solution.

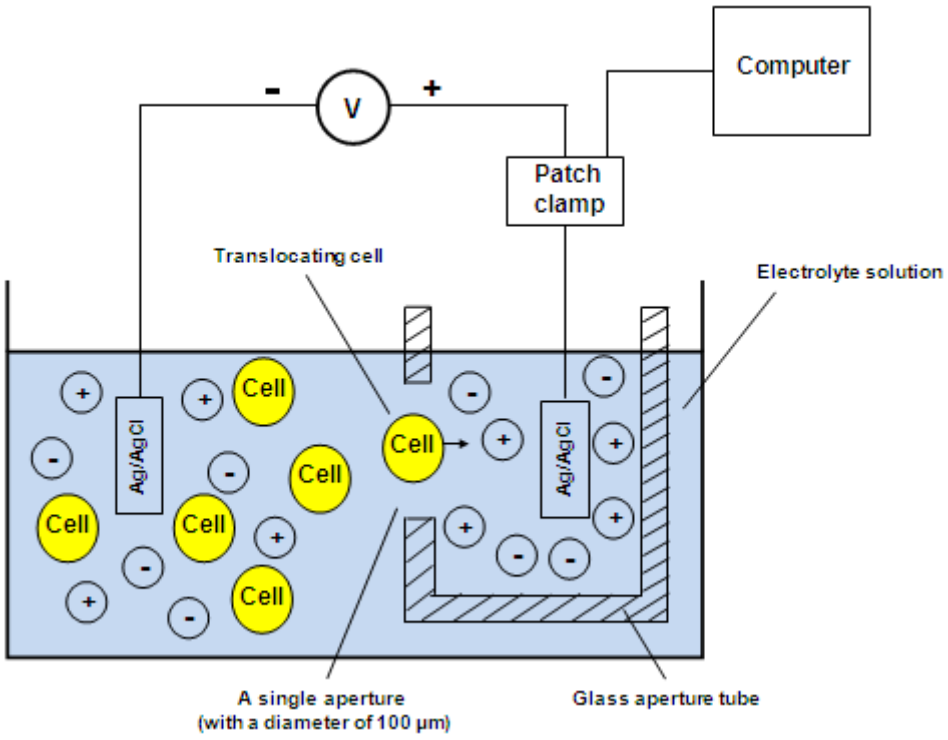

Figure 1.3: Schematic representation of a Coulter counter device with Ag/AgCl electrodes in an electrolyte solution in two compartments connected by a single 100 µm wide aperture. ⊕ and ⊖ represent positive and negative electrolyte ions, respectively.

Coulter counters were a great success in their own time, speeding up the process of detection and counting blood cells. However, the large aperture size produced unreliable results when analyzing much smaller particles, such as small cells, many biomolecules, and nanometer-scale

particles. These produce very tiny changes in the amount of resistance as they pass through the aperture, which are impossible to be detected by a large aperture. Original Coulter counters also were not aimed at evaluating topographies or conformations. Structural information about the detected cells could therefore not get retrieved.

In order to be able to more accurately detect and count the number of cells and biomolecules with micro-/nano-scale dimensions in a sample, and also to determine their structural characteristics, scientists intended to improve the features of initial Coulter counter apertures. Following the discovery of biological protein pores and significant improvements in micro/nanofabrication techniques, scientists have been able to invent electrophoretic flow detector devices that contain either nm-sized protein nanopores embedded in lipid bi-layer membranes or synthetic micro-/nano-scale pores fabricated in solid-state membrane materials. The structure and properties of both, protein nanopores and solid-state micro/nanopores, are described in subsequent sections. Their general detection approach is, however, based on the working principle of original Coulter counters.

In these further miniaturized, micro/nanopore-based approaches, cells, charged particles, or biomolecules are electrophoretically driven through a µm- or nm-sized pore by a constant bias voltage (V) applied through identical electrodes across the pore. The micro/nanopore is embedded in a thin, insulating membrane consisting of either a natural lipid bi-layer in the case of biological protein nanopores, or a synthetic solid-state material in the case of artificially fabricated micro/nanopores. The membrane separates an electrochemical chamber into two compartments or reservoirs. Both reservoirs and the pore connecting the two contain a conducting electrolyte solution. The *cis* reservoir is on the side of membrane containing the negative electrode, and the *trans* reservoir is on the side of membrane containing the positive

electrode. A patch clamp set up is used to provide a constant voltage between the electrodes. The generated voltage induces a basal ionic current through the pore, from one reservoir to the other. In the absence of any cell, charged particle, or biomolecule, the stable basal ionic current of the electrolyte solution flowing through the open pore is called *open-pore ionic current* (I_{open}). Typical I_{open} values are on the pico-ampere scale (pA). To avoid parasitic effects including electromagnetic noise deteriorating the measurement results, the patch clamp system and the electrochemical chamber are both usually housed inside a grounded Faraday cage. When particles to be detected, such as cells or charged biomolecules, are added to one reservoir, the ionic flow through the pore will also drag the particles to the other reservoir. This is called a *translocation event* that will temporary reduce the basal flow of electrolyte ions, or current, through the pore. A significant reduction or even complete blockage of I_{open} occurs if the particle size is only slightly smaller than the pore. The *ionic current reduction* or *blockade* is represented as I_{block}, and the time it takes for a translocation event to happen through the pore (i.e. *translocation time*) is represented as t_D. Typical amplified signal values for I_{block} are within a pA range on a millisecond (ms) time scale. Figure 1.4 gives a schematic representation of an electrophoretic flow detector device, containing a micro/nanopore in a thin, insulating natural or synthetic artificial membrane, and its general detection approach.

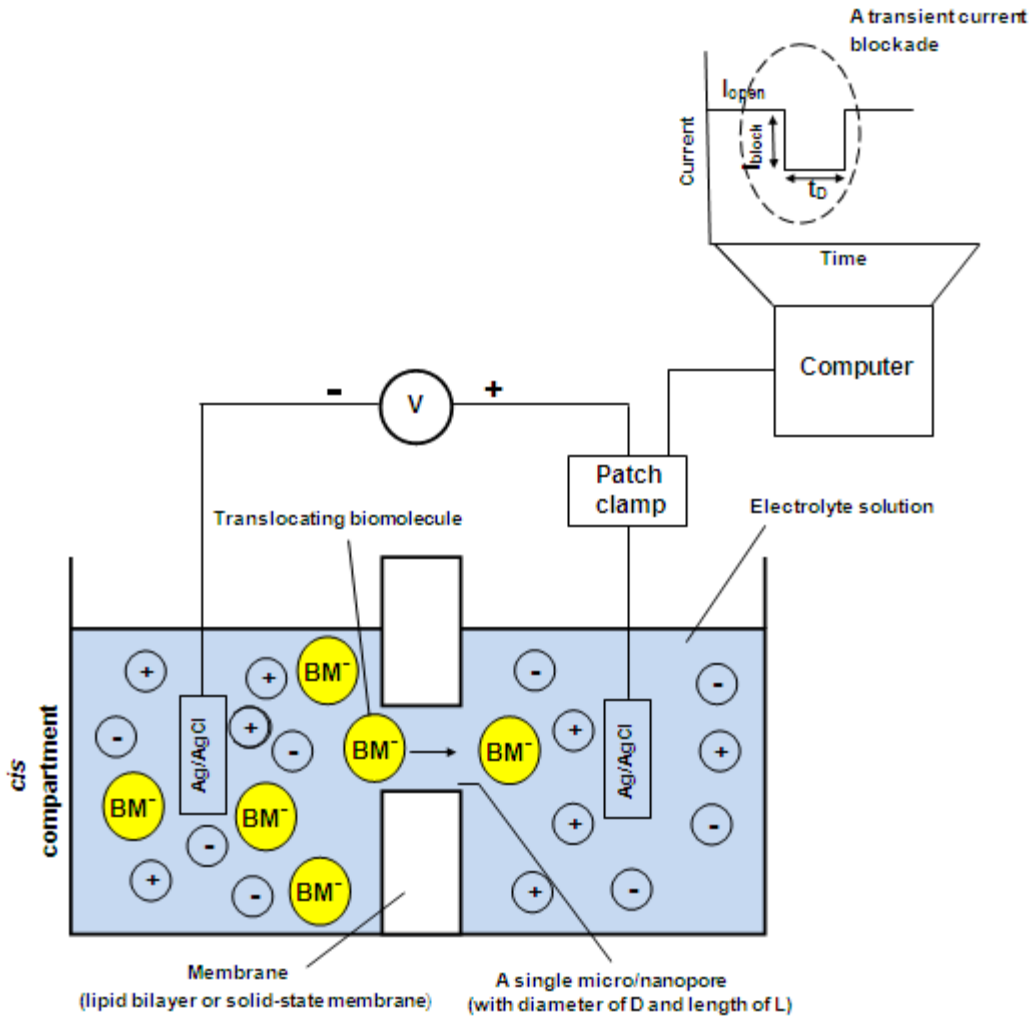

Figure 1.4: Schematic illustration of an electrophoretic flow detector device containing a single micro/nanopore, and its transient current blockade during a translocation event. BM represents the passing biomolecules through the pore, and ⊕ and ⊖ represent positive and negative electrolyte ions, respectively.

Translocation events result in distinct ionic current signals with signs, amplitudes, and durations directly corresponding to the structural properties of the passing particles [7]. Different particles with different sizes and geometries will lead not only to specific ionic current signals, but also to specific time structures of the recorded ionic current signals. Careful analyses of the

recorded signals, therefore, fundamentally allow to structurally characterize the translocating particles. This nanopore-based approach has, therefore, extended the original Coulter counter concept from simply counting the passing molecules to analyzing the resultant ionic current signals in order to obtain further structural information on the passing particles. Such structural information could potentially even lead to DNA sequencing [8, 9], which is a method for determining the order in which DNA nucleotides occur on a single DNA strand. The theory behind nanopore sequencing is that, under an applied voltage, the size of the nanopore ensures that the DNA is forced through the pore, one nucleotide at a time, like a thread through the eye of a needle. Each nucleotide on a DNA strand obstructs the nanopore to a different characteristic degree. Therefore, the amount of ionic current that can pass through the nanopore at any given moment varies depending on whether the nanopore is blocked by an Adenine, a Cytosine, a Guanine, or a Thymine nucleotide (Figure 1.5). The temporal changes in the ionic current represent direct recordings of the DNA sequence. The first experimental verification of nanopore DNA sequencing is dated back to 1996, when Kasianowicz's group demonstrated the transport of individual single-stranded DNA molecules (ssDNA) through an α-hemolysin protein nanopore [10]. DNA nanopore sequencing, however, is currently still under development. It is a promising theoretical method with limited lab bench results and needs to be improved [11, 12].

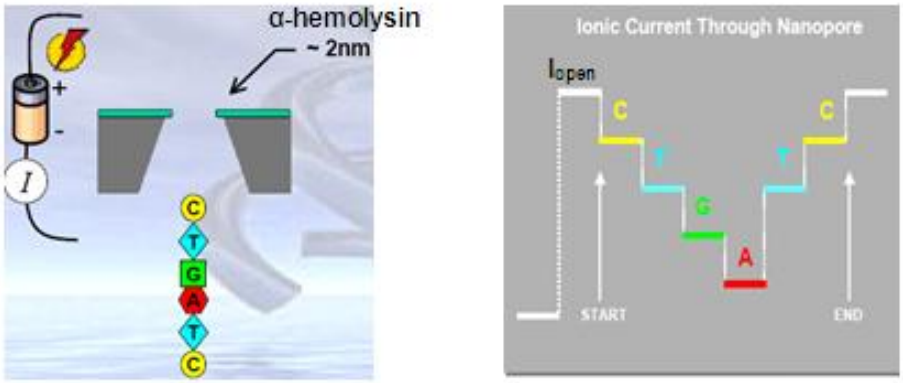

Figure 1.5: Schematic representation of single-stranded DNA sequencing using an α-hemolysin protein nanopore with a diameter of approximately 2.0 nm [10].

Generally speaking, though, miniaturized pores based on natural or artificial fabrication sequences have a great potential as electrophoretic flow detectors. Both categories will get further discussed in the subsequent two chapters.

1.4.2. Miniaturized Electrophoretic Flow Detectors: Natural Protein Nanopores

All living cells synthesize and carry various types of *protein pores* that enable them to communicate both chemically and electrically between their intracellular organelles, as well as between their intracellular and extracellular environments [4]. Most of these protein pores have open diameters on the nanometer scale. *Ion channels* are an example of such nano-scale pores that are naturally located in the lipid bi-layer membrane, transporting ions to the inside or the outside of the cell. Bacterial cells are known to synthesize and secrete proteins that can spontaneously form into pore-like shapes when inserted into a lipid bi-layer membrane. α-hemolysin, for example, is the most widely studied biological protein pore of this kind. The monomer protein is secreted by the human pathogen *Staphylococcus Aureus* bacterium as a

toxin. α-hemolysin monomers have then the ability to spontaneously self-assemble into a heptamer (seven monomers bonding together), when inserted into a human lipid bi-layer cell membrane. The heptamer forms a mushroom-like, aqueous pore across the lipid cell membrane [13]. Figure 1.6 is a schematic representation of such a heptametrical protein pore. It consists of a vestibule (top part in Fig. 1.6) connected to a transmembrane β-barrel (bottom part in Fig. 1.6). The pore is narrowest at the vestibule-transmembrane domain junction with a diameter of approximately 1.5 nm [13]. It can act as a Coulter counter when the membrane-embedded pore is immersed into an electrolyte solution and a voltage is applied across the pore. It can detect various particles and biomolecules with a diameter smaller than its own. α-hemolysin has become the nanopore of choice for detection of ssDNA and RNA biomolecules [9, 11].

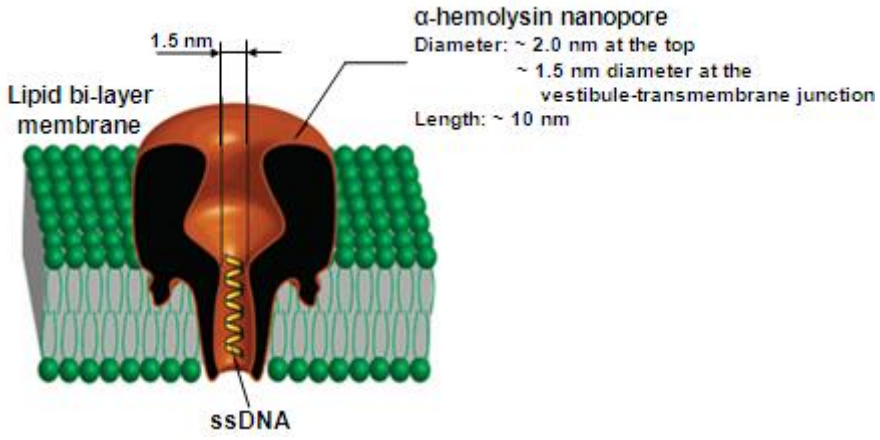

Figure 1.6: Schematic representation of an α-hemolysin protein pore embedded within the lipid bi-layer membrane of a cell [14].

Most biological protein pores, such as α-hemolysin, are very robust and durable at room temperature and neutral pH value [15, 16, 17]. They are produced by cells in large amounts with

an atomic level of precision, can be simply purified employing standard molecular biology techniques, and are able to easily self-assemble into lipid bi-layer membranes based on well-established laboratory protocols. They usually exhibit a detectable ionic current passing through the pore with a low level of background electrical noise [10]. The structure of protein nanopores can be determined by X-ray crystallography. The pores can also be chemically engineered and modified via advanced molecular biology techniques to produce pores for desired applications [12, 18, 19].

A major drawback of protein nanopores, though, is their limited stability in all environments unlike the natural cell environment. They are often susceptible to variations in electrolyte solution conditions such as pH value, ionic strength (i.e. salt concentration of the solution), and temperature. In practical applications, they get easily disrupted by, for example, strong salt solutions required to maintain DNA molecules in their single-stranded state. Besides the pores, the lipid bi-layer membranes, in which the pores are usually assembled, are also another weak spot. Lipid membranes are mechanically fragile due to weak intermolecular interactions. Furthermore, these membranes strongly limit the tolerable range of electrical parameters [18].

Besides operation, geometry also limits the versatility of protein nanopores. Protein nanopores exhibit a fixed pore diameter and length. This makes them very selective electrophoretic detectors, and restricts their application to the detection of only certain particles with the right geometry compared to nanopores [9, 18]. To overcome these limitations, fabrication of artificial synthetic micro/nanopores in solid-state membranes has become a very important area of research.

1.4.3. Miniaturized Electrophoretic Flow Detectors: Artificial Micro/Nanopores

Some of the limitations of biological protein nanopores could be overcome if μm- or nm-sized pores were artificially fabricated in thin film membranes. The advent of BioMEMS has started a wide variety of research in this field, and selected devices are already commercially available, e.g. from Nanion, Munich, Germany, or Oxford Nanopore, Oxford, UK.

Micro-electromechanical systems (MEMS) are micro-scale devices which combine mechanical and electrical components for, e.g., sensing and/or actuation. MEMS technology has been largely adapted from the integrated circuit industry and applied to the miniaturization of systems beyond electronics. MEMS applications are diverse and include many sub-fields such as optical MEMS, radio frequency MEMS, and BioMEMS. BioMEMS stands for biomedical micro-electromechanical systems and focuses on applications in medicine, biology, and biomedical research. In recent years, development of electrophoretic flow detector devices containing single artificial micro- and nanometer-sized pores fabricated in synthetic membranes is one of the major focuses of considerable research efforts in BioMEMS.

Micro- and nanometer-sized pores in solid-state membranes are now the basis for a promising class of electrophoretic detectors for rapid electrical detection and structural characterization of various cells and biomolecules. They were first employed for DNA sensing in early 2001 [20]. From then, they have been studied by different groups for detection and structural characterization of different lengths and even conformations of dsDNA, proteins, DNA/protein complexes, and nanoparticles [21, 22, 23, 24, 25, 26, 27, 28, 29]. Nanopores in solid-state membranes offer several advantages over their biological protein counterparts in lipid bi-layer membranes, including:

- Artificial pore geometries and shapes are tunable over a wide range from nanometers to micrometers to suit the desired applications;
- the membranes are mechanically, chemically, thermally, and electrically highly stable over a broad range of experimental conditions such as various pH values, temperatures, and different types of solvents;
- pores and membranes often feature adjustable surface properties;
- systems are stable for extended periods and potentially even re-usable, and thus cost-effective;
- artificial pores can be readily integrated into different micro- and nano-devices.

Artificial micro/nanopores have been fabricated in a variety of membrane materials. Electrophoretic applications require the membrane material to be electrically insulating. Silicon and organic polymers are the two most widely used groups of membrane materials for the fabrication of solid-state micro/nanopores in electrophoretic flow detector devices [30, 31]. Silicon is chosen as a membrane material as its micro/nanofabrication sequences are best developed and established. These sequences start with single crystalline silicon wafers, and in most of the cases, a number of thin membrane layers such as silicon oxide (SiO_2) or silicon nitride (Si_3N_4), and eventually even metal or organic layers are deposited by various chemical and physical deposition techniques [18, 20, 32, 33, 34]. Although silicon-based micro/nanofabrication processes have gained tremendous interest in many areas of applications, the use of silicon-based materials as an electrophoretic flow detector membrane has some drawbacks due to the limited hydrophilicity (i.e. limited wettability of the pore), the complicated control of structural details at nanometer lateral resolution and comparatively great thicknesses

required for stability, corresponding long processing times, as well as biocompatibility issues in selected material combinations [35].

With advances in the synthesis and production of different polymer materials and polymer-based micro/nanofabrication technologies, the use of organic polymers is the most recent innovation in the development of electrophoretic flow detector devices. Polymers are large molecules formed through the linkage of many repeating subunits called *monomers*. They are a large family of materials exhibiting a wide range of specific properties, which make them good alternatives to silicon for the fabrication of individual micro/nanopores in membranes [36, 37, 38]. In comparison to silicon, polymers offer several advantages, including:

- They exhibit different degrees of optical transparency, with many of them used in micro/nanofabrication being transparent;
- they are compatible with a diverse range of micro/nanofabrication techniques using simple processing steps;
- using replication/nano imprint technologies, polymer-based structures might be produced at high production rates and moderate costs;
- they present good rigidity and mechanical strength, high electrical insulation, and good thermal and chemical properties;
- they are often more hydrophilic (i.e. can be wetted more easily), and show good biocompatibility; and
- their surface properties (e.g. wetting ability/hydrophilicity, adhesion, and reactivity) can be modified using a number of different surface modification techniques.

1.5. Review of Fabrication Processes for Micro/Nanopores

Fabrication of high quality artificial micro- and nanometer-sized pores in thin membranes is a challenging task and requires lengthy processing sequences.

Most such pores are fabricated in silicon, silicon nitride, or silicon oxide. Fabrication is generally based on the toolbox known from microelectronics: It typically involves patterning of a thin photoresist by means of ultra violet lithography or electron beam lithography to generate an etch mask for subsequent plasma-based dry etching. The thin membrane is typically obtained by one-sided wet-chemical back-etching of a sacrificial silicon substrate. Drawbacks of this approach include limited fabrication alternatives and materials properties not ideally suited for electrophoretic applications, as stated in the previous chapter [22, 32, 39].

Many emerging pore-based systems are fabricated using polymers [40, 41], such as polyimide (PI), polystyrene (PS), polycarbonate (PC), polyethylene terephthalate (PET), or polydimethylmethylsiloxane (PDMS, often referred to by its trade name Sylgard, Dow Corning, Midland, USA). Such materials are good electrical insulators and comparatively cheap, allowing for disposable systems. Most importantly, however, can polymers be patterned by a wider selection of processes. These include primary patterning processes based on various lithographic or random etching techniques, as well as replication and nano imprint techniques that are particularly suitable for cheap mass production:

Latent Ion Track Etching is a rather exotic alternative to lithographic patterning described further down. It can be used to fabricate single pores, as well as commercially-available multiple pore membranes based on a randomized exposure of a polymer film by heavy ions. These tracks are only a few nanometers wide and can selectively get etched. The randomized nature of this

process and the lack of availability to the research group, however, determined that it is not pursued in this research [40, 41].

Lithography is the standard microfabrication technique for the patterning of a polymer film, referred to as the *resist*. Unlike in silicon-based processes mentioned above, here, the patterned resist is not used as a processing mask for subsequent etch processes, but is rather used as the microstructure directly. The resist is chemically modified upon local exposure by energetic radiation. Exposure is controlled by applying masks, or by serially writing with a focused beam. Subsequently, the resist gets selectively removed in a wet chemical *developer*. For positive tone resists, exposed resist areas become soluble in the developer. For negative tone resist, exposed areas become insoluble. Depending on the energetic radiation used, lithographic processing is divided into ultra violet (UV) lithography, electron beam (EB) lithography, focused ion beam (FIB) lithography, and X-ray lithography, to name the most important variations. UV lithography is limited by diffraction and does not readily allow for deep submicrometer patterning [42, 43]. X-ray lithography is a powerful alternative and theoretically allows for the patterning of sufficiently small pores, even in a parallel approach. However, it requires very expensive masks and therefore is not appropriate for a proof-of-concept as pursued in this research. FIB are a very suitable tool, but are not available for the present research. Therefore, EB lithography is applied as the most appropriate technique.

Once the concept has been proven and an optimized layout has been determined, future studies might include a more parallel, or higher throughput, polymer patterning approach that justifies the additional tools required. These could include masks in X-ray lithography or stamps in replication, including small features down to about 15 nm as demonstrated with different variations of nanoimprint lithography [42, 43, 44].

Certain structures in polymers, such as pores, can get post-processed to decrease the feature size beyond typical technology limits. To produce pores with a diameter of about 1 nm to 20 nm, for example, standard lithography techniques can be complemented using non-conventional techniques further modifying the polymer by minimizing the surface tension energy. Such an approach is often referred to as a polymer reflow process. A Transmission Electron Microscopy (TEM)-based approach not only further modifies the pore size, but also provides real-time visual feedback [32]. This technique was originally proposed by Storm et al. Another post processing method uses laser power as a heat source [45] to initiate a surface tension-driven mass flow mechanism, reshaping micropores to nanopores under suitable conditions. Wu et al. has demonstrated that initial pores of hundreds of micrometers in diameter can be reduced to a few hundred nanometers.

1.6. Objectives

The previous chapters identified nanopore-based devices as powerful tools for detecting and analyzing biomolecules. Polymer materials are promising candidates for such devices because they tend to be cost-effective and disposable, well-suited for electrophoretic applications, and can get micropatterned by a variety of processes tailored at various pore sizes. These considerations derive the overall goal of the present research to develop all-polymer, micro/nanopore-based flow detector devices that are suitable for biomedical applications.

Specifically, the objectives are:

1. Develop a concept for an all-polymer nanopore detector allowing the continuous variation of the pore size in the range from about a micrometer down to a few nanometers for best pore-size adaption to the biomolecules to be investigated.

2. Built, test, and characterize the detector and prove its use in electrophysiological experiments using DNA and BSA biomolecules.

1.7. Thesis Organization

This thesis is divided into six chapters. Chapter 1 provides an introduction to the need of analyzing biomolecules and explains key properties of important biomolecules. Changes in concentration and morphology of biomolecules are mentioned as a key motivation for this research as they can be indicative of specific diseases in the body. Conventional methods of detection of biomolecules are described, and the need for developing faster, more accurate, and more cost-efficient detection methods is presented. Electrophoretic detectors based on micro/nanopores fabricated in solid-state membranes are then compared to their biological counterparts, and commonly applied classes of membrane materials and the respective patterning processes are discussed.

Chapter 2 focuses on the models and theories that are used for geometrical layout and characterization of single cylindrical pores fabricated in this work. A surface energy density model is introduced to identify potential regimes and boundary conditions and to control a microfabrication postprocessing method for fine-tuning the size of submicron pores fabricated in this study. Finally, the Deblois resistance variance model is applied for the investigation of particles translocating through nanometer-sized pores.

Chapters 3 and 4 focus on the design and fabrication of novel all-polymer electrophoretic flow detectors that contain either a single submicron- or nanometer-scale pore. Design concerns in Chapter 3 comprise the selection of proper materials for both, membrane and detector device components, in particular assessing the suitability of poly (methyl methacrylate) (PMMA), and the determination of geometrical dimensions of membrane and pores to be fabricated. Some of

the geometry considerations are supported by FEM analyses. Auxiliary detector device components are also introduced in this chapter.

Chapter 4 describes the fabrication sequence that was developed, tested, and improved. Process parameters for all fabrication steps involved are given, starting with patterning of the PMMA membrane using electron beam lithography and post processing sequences. Development and implementation of a process- and biocompatible, hermetic sealing and systems integration concept for an all-PMMA-device is the next focus. The chapter concludes with a description of an alternative, bottom-up nanopatterning approach exploiting self-assembly of α-hemolysin pores into lipid membranes.

Chapter 5 presents test results of the detectors fabricated. It starts out with determining the actual functional dimensions of the detector devices. This is followed by the electro-chemical characterization of submicron pores. The third subsection deals with functional analyses of the micro/nanopores developed: In a first step, the detection and discrimination of test particles, two populations of differently-sized silica nanoparticles with diameters of 100 nm and 150 nm, are proven. In a second step, self-assembled protein pores are applied to detect translocation events of linear single stranded DNA molecules. Finally, translocation dynamics are studied for electron-beam written and post processed nanopores. Two different biomolecules are analyzed, evaluated and compared: double stranded DNA and Bovine Serum Albumin protein.

Chapter 6 presents a summary and conclusions, and lists the contributions of the current research, along with an outlook on suggested future work.

2. Theory of an All-PMMA Electrophoretic Flow Detector

The basic concept of the electrophoretic flow detector system pursued in this research is derived from considerations in chapter 1.4 and is illustrated in Figure 2.1. It consists of a membrane with the nanopore clamped between two electrolyte reservoirs. All of these components are made of polymers. In the process of designing and fabricating these components, the stability of the thin membrane is particularly critical, and its behavior is best analyzed by numerical simulations. Electrodes in the reservoirs are connected to a voltage source, and induced ionic currents and the processes inside the pore should be properly understood and modeled. These tasks are approached in the subsequent chapter 2:

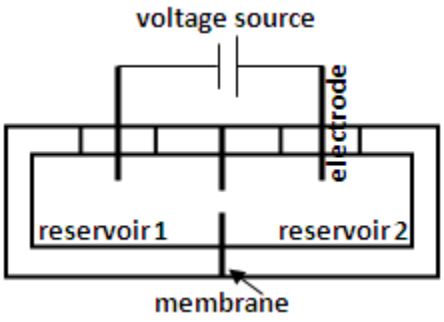

Figure 2.1: Schematic layout of Electrophoretic Detector System.

A variety of challenges need to be considered before any actual microfabrication procedure can be performed. These challenges include the selection of the polymer membrane material to be used and its biocompatibility and process compatibility, the pore general layout and its size optimization, and the membrane stability against the forces exerted. Based on the simulation results and analytical analyses in this chapter, a detailed detector concept and design will get developed in subsequent chapters. A further model developed and discussed in this chapter and

used in the applications chapters later on is a surface energy density model to identify potential regimes and boundary conditions and to control a microfabrication postprocessing method for fine-tuning the size of fabricated submicron pores. Finally, the Deblois resistance variance model is introduced for the investigation of particles translocating through nanometer-sized pores in chapter 5.

2.1. Membrane mechanical Properties and Design Limitation

Geometrical dimensions of the patterned polymer membrane will have a major impact on the microfabrication processes applicable for the patterning, the allowable systems integration tolerances, and the stability of the membrane during fabrication and operation. In these considerations, the geometrical parameters of membrane thickness (or pore length) and the freely suspended membrane diameter face opposing requirements that need to be optimized: Thinner membranes are simpler to micro-/nano-pattern, and they can be wetted more easily, but they are also more susceptible to failing under mechanical stress during microfabrication and operation. A larger membrane diameter allows for larger assembly tolerances, but, again, is more susceptible to rupture under mechanical stress. In this context, a minimum requirement is stability against the differential pressure exerted by different electrolyte levels on either side of the membrane while the first reservoir gets filled.

The parameter optimization is performed numerically using the finite element method (FEM). The thickness of a spincoated membrane can be varied to the desired value, but this value will then be more or less constant across the entire device. It will also be much thinner than its lateral size. Therefore, a 2-dimensional FEM model can be applied.

The quantity simulated to ensure that the final design does not fail against the applied forces is the *von Mises stress* [46]. If its maximum value induced in the material exceeds the material

yield stress, the material starts to deform permanently or fail. The von Mises stress is derived from distortion energy failure theory, which is defined as the minimum energy required to deform a material's shape without changing its volume. It serves as a model for calculating an equivalent stress in a generalized, three-dimensional load case. The von Mises stress σ_v can be written as

$$\sigma_v = \left[\frac{(\sigma 1 - \sigma 2)^2 + (\sigma 2 - \sigma 3)^2 + (\sigma 3 - \sigma 1)^2}{2}\right]^{1/2} \tag{2.1}$$

in which $\sigma_{1,2,3}$ correspond to the normal stress values along the *x*, *y*, and *z* axes, respectively.

Varying the geometrical parameters, the von Mises stress is simulated as a function of membrane thickness and diameter. In this simulation, different thicknesses will not be implemented by additional layers in the mesh, but are considered input parameters. The shape of the membrane is always assumed to be round as a circular shape can tolerate higher loads at a constant membrane thickness when compared to a rectangular one. Furthermore, manual alignment and sealing during the fabrication process will be facilitated by a circular shape.

Figure 2.2 represents the FEM mesh used in the simulations. The mesh is a single layer of elements applied in the 2-dimensional discretization.

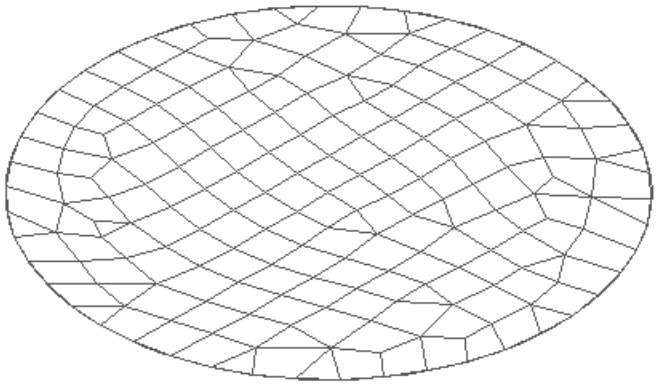

Figure 2.2: Discretization model in isometric view: Schematic of the membrane mesh used for the 2D FEM simulation.

The number of elements used in numerical methods always is a compromise between accuracy achieved and processing time needed. An increased number of elements and nodes results in a more accurate solution, but takes longer to converge. In this membrane, based on system automization due to minimum residual value, it is defined that 165 elements and 178 nodes satisfy the accuracy needed for the design. The next step is to define the constraints, or boundary conditions. The membrane is fixed at its perimeter since this is where the actual membrane will be glued to a housing, and no movements will occur in reality. Figure 2.3 illustrates these conditions.

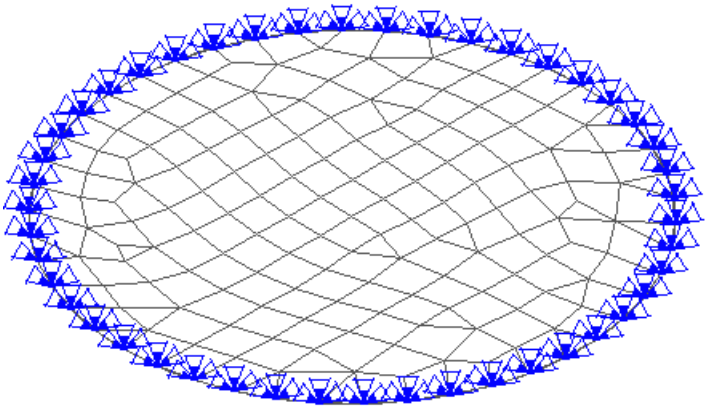

Figure 2.3: Schematic of the constraints for the membrane in isometric view.

The last step in preparation of the simulations is to define the load case. In our case, constant distributed force acting orthogonally on the membrane is assumed, representing the geodetic pressure arising from the electrolyte head.

$$P = \rho \cdot g \cdot h \tag{2.2}$$

where P is the head pressure, ρ is the electrolyte density, g is the gravitational constant, and h represents the electrolyte head.

This load case immediately illustrates that a smaller membrane diameter will result in reduced forces acting on the membrane, assuming a constant geodetic pressure. Figure 2.4 graphically represents the case considered. In a real experiment, this pressure is eventually counterbalanced from the opposite side of the membrane if both reservoirs are filled identically. During the filling, however, the full differential pressure is experienced by the membrane, which therefore is assumed as the worst-case scenario.

The full differential pressure is derived based on equation 2.2, using the room temperature water density of $\rho = 0.998\ g/cm^3$, the gravitational constant of $g = 9.81\ m/s^2$, and a maximum geodetic height of 3.68 mm. The latter is given by the inner radius of the PMMA tube applied as the reservoirs ($\varnothing_{tube,\ inner} = 6.35\ mm$, see chapter 3.2.3) plus the radius of the anticipated freely suspended membrane ($\varnothing_{membrane} = 1.0\ mm$, see below). Together, a pressure of up to $P = 36\ Pa$ is anticipated.

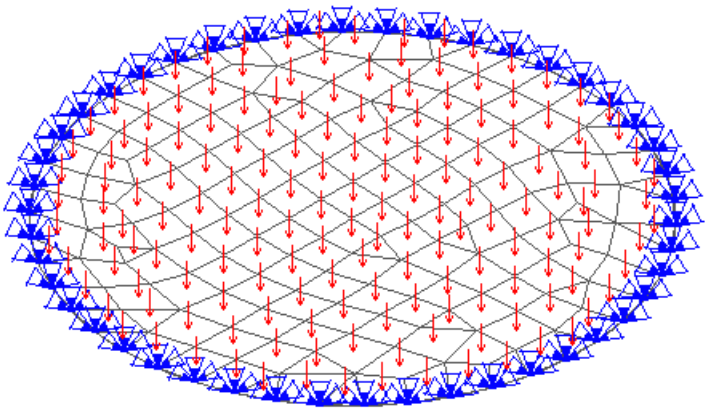

Figure 2.4: Illustration of geodetic pressure evenly applied to one side of the membrane.

Material properties of a polymer membrane at the example of PMMA are assumed to be the *yield strength, Y=73 MPa; Module of Elasticity, E=3200 GPa; Poisson Ratio, v=0.4* as taken from *ISO 527*. Initial geometry and load parameters are set to be a membrane diameter of $D = 1000\ \mu m$, a membrane thickness of $T = 250\ nm$, and an applied pressure of $P = 36\ Pa$ as explained above. The simulated von Mises stress is shown in Figures 2.5. In chapter 3, such results will be further commented on and the geometry be optimized to derived design parameters for the detector.

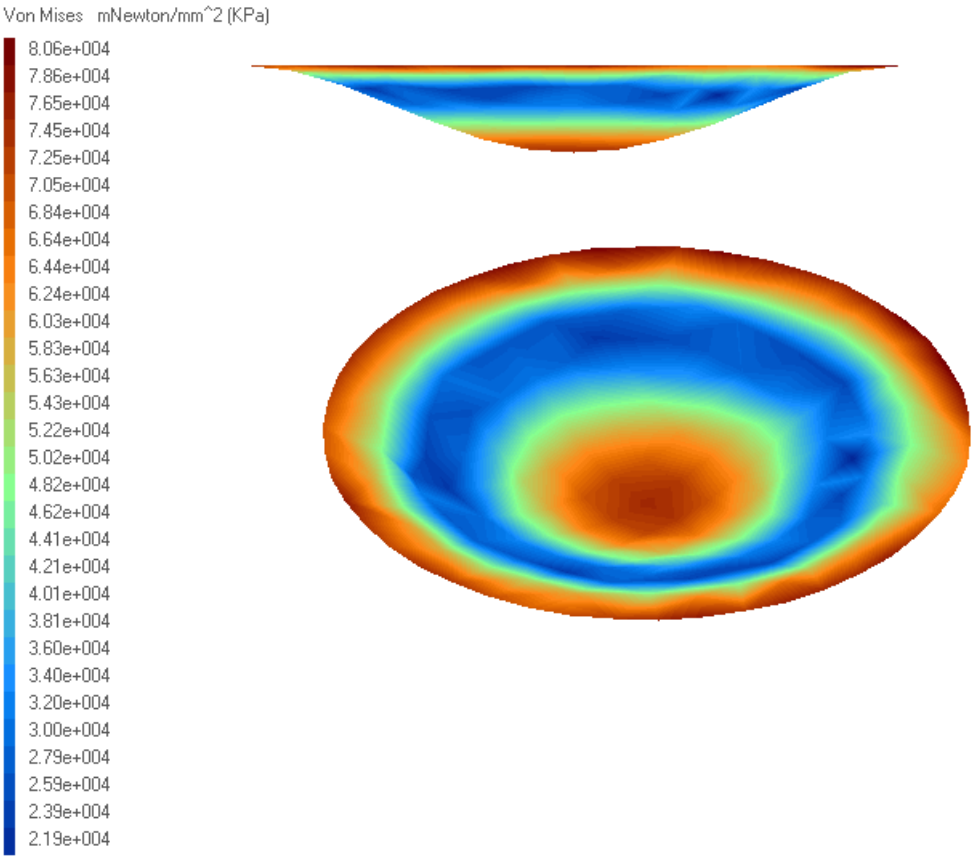

Figure 2.5: Simulation of von Mises stress resulting from a uniform pressure of 36 Pa in a PMMA membrane with a diameter of 1 mm and a thickness of 250 nm. Side view (top) and the isometric view (bottom).

Under these conditions, the maximum von Mises stress amounts to about 80 MPa and therefore slightly exceeds the PMMA yield stress of 73 MPa. Stress peaks occur in the center as well as at the perimeter of the membrane. These results indicate that the membrane parameters need to be modified for safe operations.

2.2. Surface Energy Density Model applied for Post Processing of the Pore to fine tune the Diameter

According to chapter 1.5, electron beam lithography was selected for patterning the membrane. Lower acceleration voltage machines accessible within this research are not necessarily capable of patterning pores down to a few dozen nanometers in diameter in membranes of at least several hundred nanometers thickness. In the context of the research goal, being able to fabricate pores with variable sizes, a two-step nanopatterning sequence can be pursued: The first step comprises lithographic patterning of the smallest pore possible, and on the second step augments the result applying additional postprocessing techniques. These could involve adding a coating to the pore walls, or reshaping the pore in a reflow process.

The latter is the approach taken since thermoplastic membranes fundamentally allow for reshaping. UV exposure can be applied to reduce the pore diameter by minimizing the surface energy of the solid. This approach is based on a model by Storm et al. [32]: At high temperatures, many solids start to deform. For instance, when exposed to high-energy beams and, thus high temperatures, membranes have a tendency to deform and lower their surface free energy by changing their surface area. In membranes containing a pore, changes in surface area will cause the pore to either shrink or expand in diameter, while the pore volume remains constant. In Storm's original model, electron beams are applied. We do not have the appropriate instruments available for experiments, and use broadband UV light as the energetic radiation instead. This approach has additional benefits as pertaining to the control of surface charges on the PMMA membrane, which will be discussed in later chapters.

Since pores can either expand or contract upon exposure, Storm's model will be briefly discussed in terms of a single-pore layout [53]: A membrane with a single cylindrical pore of

radius r and constant length L is kept under constant uniaxial tension P' and at a high temperature. The pore has an overall surface A, consisting of the actual pore walls as well as the imaginary top and bottom lids. With the surface energy density of the membrane γ, the variation of total Gibbs free energy at equilibrium ∂G is given by

$$\partial G = -P'\partial L + \gamma \partial A = 0 \tag{2.3}$$

This change in free energy therefore delivers

$$P'\partial L = \gamma \partial A \tag{2.4}$$

in which the overall pore surface A described above is given as

$$A = 2\pi r^2 + 2\pi rL \quad \text{and} \quad \partial V' = 0 \tag{2.5}$$

The surface energy density γ can then be written as:

$$\gamma = P'L/2\pi r(L - r) \tag{2.6}$$

This delivers geometrical constraints for a membrane with a pore, lowering its surface free energy when exposed to high-energy beams: The membrane will reduce the pore radius r if the pore has an original radius $r < L/2$. However, it will increase the pore radius if the pore has an original radius $r > L/2$ [32, 53]. In other words, only selected pores will laterally shrink upon this

kind of post processing: the original pore needs to be at least twice as long (deep) when compared to its radius. In terms of aspect ratio, which is the feature height divided by the minimum lateral feature size, the length-to-diameter ratio must exhibit an aspect ratio of at least one.

Due to the geometrical constraints in this research, aspect ratios larger than one are applied, and a reflow post processing sequence can therefore theoretically be applied to optimize the diameter.

2.3. Theoretical Model for the Electrophoretical Derivation of Pore Dimensions

The performance of the electrophoretic detector system will primarily be determined by the actual dimensions of the pore. These dimensions can get established via metrology techniques, but many of them do not provide sufficiently precise data or do not necessarily deliver the diameter at the minimum cross section. An alternative is to use the detector properties themselves to derive the dimensions electrochemically, using the ionic resistance/conductance of the pore as follows [49, 45, 50]:

Geometrical parameters are evaluated by measuring the ionic resistance of the device under its intended operation. Subsequently, the results are referenced to each other and to simulated data. Assuming ohmic conductance, the open pore current I_{open} through a pore can be correlated to the pore diameter D and length L by

$$I_{open} = K'(D^2)/L \tag{2.7}$$

where K' is a constant dependent upon the voltage and electrolyte resistance [48]. An approximations for the resistance of a pore can be obtained as [51]

$$R = \frac{1}{K}\int \frac{dL}{A(L)} \tag{2.8}$$

where *A(L)* is the pore cross sectional area perpendicular to its length *L*, and *K* is the specific conductivity of the electrolyte inside the pore.

Integration of equation 2.8 under the restriction of cylindrical pore shapes, which can be approximated by small pore diameters *D* compared to their length, or high aspect ratios as already stipulated in the preceding chapter (*L>>D*), delivers [52]

$$R = \frac{V}{I} = \frac{4L}{\pi K \mathrm{D}^2} \tag{2.9}$$

which can be solved for the pore diameter *D* as

$$D = \sqrt{\frac{4LI}{\pi KV}} \tag{2.10}$$

The unknowns in this equation can exactly be obtained: The pore length *L* corresponds to the membrane thickness and is determined by stylus profilometry or similar techniques. *V* is the voltage applied across the membrane, and *I* is the current through the pore. Both electrical parameters *V* and *I* are well controlled using a high precision patch clamp test setup. The electrolyte conductivity *K* determines the resistance of the pore itself and is measured by the steady-state ionic current flowing through the pore at a given applied external voltage.

The pore diameter D derived from equation 2.10 is an exact solution for cylindrical pores. For symmetric pores, it can serve as an approximation of the effective diameter. For all pores of similar cross section, it is a powerful tool to compare pore diameters relative to each other.

2.4. Deblois Resistance Variance Model for Analytical Predictions of Electrophoretic Current Blockades

Developing a model to theoretically predict the electrophoretical performance of a pore has many benefits: Results can be implemented in the design of the required geometry. They can also be used to compare theoretical and experimental results in order to better understand experimental results or to discriminate between measured translocation effects and artefacts. The model can be verified by comparing predicted and measured data when analyzing translocations of known particles through the pore.

Translocation events are often associated with an increase in resistance ΔR due to the presence of nanoparticles inside the pore. This additional resistance leads to a temporarily reduced current or current blockade I_{block}, which is also denoted as ΔI in some of the formulas. A variety of models have been proposed in literature to estimate the resistance variance exerted by a single particle translocating through a pore. None of them, however, are proven valid for all kinds of pores in terms of various shapes and dimensions. In other words, there is not yet an exact single model described in literature by which translocation events of single particles passing through all different kinds of pores could be evaluated. For example, Maxwellian theory employs an ingenious argument, by which a simple model was obtained using the effective resistivity ρ_{eff} of a diluted suspension of insulating spheres in a solution of original resistivity ρ'. The effective resistivity is a function of the volume fraction of the spheres in suspension [51]. The Maxwellian expression of resistance variance can be used either to size the particles or to

measure the pore diameter. However, although the expression is correct for a small sphere in comparison to the pore diameter, it estimates lower ΔR values than the actual experimentally measured ones. This is because the model considers the total current with uniform distribution inside the pore [51].

Another approach to look at the resistance variance induced by a translocating particle is to consider a translocating sphere in a uniform electric field instead of investigating the current [52]. Deblois proved that this assumption can generate a model that is valid over a broad range of pores with different shapes and dimensions. In this model, the applied constant potential difference across the pore creates tubular current streamlines that slightly bulge around the translocating sphere. Compared to other previously proposed models, these assumptions and descriptions seem to be closer to what really occurs in a pore with a translocating particle. This model gives rise to higher values of resistance increase induced by a translocating particle compared to the Maxwellian model [54]. Figure 2.6 represents the cross section of a pore with diameter D_m and length L. The broken lines symbolize two electric field lines with a separation of $D(z)$ varying along the axis z along the pore. Inserting a non-conducting sphere of diameter d modifies the originally uniform field and leads to bulging of the field lines. The pore walls at D_m limit the maximum bulge the field lines can experience [55].

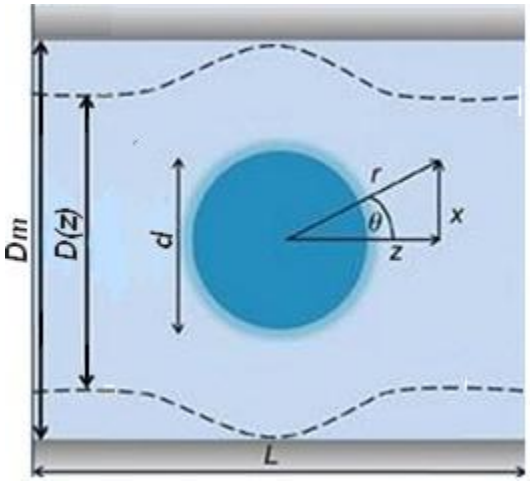

Figure 2.6: Schematic of the cross section of a pore with a non-conducting sphere and electric field lines [55]**.**

To satisfy the spherical boundary conditions, Deblois proposed a solution of Laplace's equation of the first odd zonal harmonics, i.e.

$$V(r,\theta) = (Ar + B/r^2)\cos\theta \tag{2.11}$$

V is the applied potential. r is the distance and θ is the angle measured from the *z*-axis, as illustrated in Figure 2.6. *A* and *B* are constants and will be determined based on the boundary condition at the sphere surface that changes in the field normal to the insulating sphere surface must be zero:

$$-\delta V/\delta r|_{r=d/2} = 0 \quad \text{and} \quad B = d^3A/16 \tag{2.12}$$

Inserting equation (2.12) into equation (2.11) delivers

$$V(r,\theta) = A(r + d^3/16r^2)\cos\theta \tag{2.13}$$

This potential describes tubular current field lines that slightly bulge around the sphere as shown in Figure 2.6. It is an exact solution for such a bulge shape inside the pore. Experimental verification by Deblois further showed that the bulge shape size depends on the proportionality between the sphere diameter *d* and the pore diameter D_m. The bigger the sphere, the bigger is the bulge size. If $d/D_m=0.5$, for instance, the bulge size is only 7% [52].

Based on this bulged field, the variation in pore resistance ΔR can be approximated by comparing the resistance in the center of the bulge R_2 to a situation in the absence of a particle at all, the unobstructed case with open pore resistance R_1. R_1 therefore constitutes a lower limit of the pore resistance and the distribution of the total current can be assumed uniform across the cross section in this case.

Integration of the electric field from the center line to the pore walls will deliver the potential difference. Using the electrolyte's resistivity ρ', Ohm's law translates this into the total current along the *z* axis through any cross section with diameter *D* and distance *z* from center of sphere as

$$I = \frac{2\pi}{\rho'}\int^{D/2} E_z\, x dx \tag{2.14}$$

where *x* is the distance from the central axis, and E_z is the component of the electric field along the *z* axis. E_z can be written as

$$E_z = \frac{-\delta V}{\delta r}\cos\theta + \frac{1}{r}\frac{\delta V}{\delta \theta}\sin\theta \tag{2.15}$$

The lower limit of the integration in equation 2.14 can vary between zero and *d/2*. The first case represents the pore center line as the integration limit, in areas where there is no sphere, corresponding to |*z*| values larger than *d/2*. The second case puts the integration limit right to the full radius of the sphere, corresponding to a |*z*| value of zero. Equation 2.14 therefore turns into

$$I(Z) = (-\pi A D^2/4\rho')\{1 - [d^3/(D^2 + 4Z^2)^{3/2}]\} \tag{2.16}$$

as a general case. When *z = 0* at the bulge, the equation simplifies into

$$I(0) = (-\pi A {D_m}^2/4\rho')[1 - (d/D_m)^3] \tag{2.17}$$

Continuity demands that a given current through the pore is constant along the pore, no matter whether a region with the sphere |*z*| < *d/2* is considered, or an area beyond the sphere |*z*| > *d/2*. Equating equations 2.16 and 2.17 therefore results in an implicit expression for *D(z)*

$$D^2[1 - d^3/(D^2 + 4Z^2)^{3/2}] = {D_m}^2[1 - (d/D_m)^3] \tag{2.18}$$

Ohm's law, using equations (2.13) and (2.17), deliver the pore resistance in the presence of a sphere R_2

$$R_2 = [V(-L/2) - V(L/2)]/I = \frac{4\rho' L}{\pi {D_m}^2}\left[1 + \frac{1}{2}(\frac{d}{L})^3\right]\left[1 - (\frac{d}{D_m})^3\right]^{-1} \tag{2.19}$$

The resistance variance is limited by the lowest resistance R_1 in the completely unobstructed case. This case is much easier to derive and is based on the most useful approximations for the resistance of a tube of varying cross section (equation 2.8). This leads to an approximation for R_1

$$R_1 = \frac{8\rho'}{\pi}\int_0^{L/2}\frac{d_z}{D^2} \tag{2.20}$$

Since the physical size of the pore does not change, and since the field lines resemble streamlines continuously linking the areas without and with a sphere, the expression developed for D in equation 2.18 can be substituted for D^2 in equation 2.20, delivering R_1 as

$$R_1 = \frac{4\rho'}{\pi {D_m}^2}\left[1 - (\frac{d}{D_m})^3\right]^{-1}\left[L - 2\int_0^{L/2}\frac{d^3 d_z}{(D^2 + 4z^2)^{3/2}}\right] \tag{2.21}$$

Equations 2.19 and 2.21 determine the resistance variance ΔR as

$$\Delta R = R_2 - R_1 = \frac{4\rho'}{\pi {D_m}^2}\left[1 - (\frac{d}{D_m})^3\right]^{-1} \times \left[\frac{d^3}{2L^3} + 2\int_0^{L/2}\frac{d^3 d_z}{(D^2 + 4z^2)^{3/2}}\right] \tag{2.22}$$

This equation constitutes an upper limit of the resistance variation if D is substituted from equation 2.18. When $d \ll D_m$, $D=D_m$ is a valid approximation, and equation 2.22 can be integrated as [52]

$$\Delta R_{(d/D_m)\ll 1,(D_m/L)<1} \rightarrow \frac{4\rho' d^3}{\pi {D_m}^4}\left[1+\frac{3}{8}\left(\frac{D_m}{L}\right)^4+\cdots\right] \tag{2.23}$$

This model has preserved the Maxwellian value as its limit and seems to be the most appropriate for the pore diameter of 454 nm in [52] where the sphere size is smaller than the pore size. In this model, ΔR also shows a high independency of the pore length, which means it can determine D_m quite locally. The expression for the variation in resistance ΔR derived in equation 2.23 can be simplified using series expansion, which delivers the following approximation:

$$\Delta R = \frac{4\rho' d^3}{\pi D_m^4}\left(1+1.26\frac{d^3}{D_m^3}+1.1\frac{d^6}{D_m^6}\right) \tag{2.24}$$

Using this model, the magnitudes of the current blockage spikes $I_{block} = \Delta I$ can be determined as follows [54]

$$\Delta I = I_{open}\frac{\Delta R}{R_{open}+\Delta R} \tag{2.25}$$

where I_{open} represents open pore current, R_{open} is the pore resistance in the absence of particles, previously introduced as R_1, and ΔI is the current blockade I_{block}.

3. Design of an All-PMMA Electrophoretic Flow Detector

As discussed in chapter 1, single synthetic micro-/nano-meter-sized pores embedded in an insulating membrane are the basis for a promising class of detectors for rapid electrical detection and characterization of biomolecules. Like their biological counterparts, these detectors can quantify and eventually identify biomolecules based on the conductance of current through the pores [56]. Fabrication of synthetic micro- or nanopores offers several obvious advantages over biological nanopores. These include flexibility in pore diameter and length; high stability against external parameter variations such as the pH value of the solutions, salt concentration, temperature, and mechanical stress; adjustable surface properties of the pore; as well as integration possibilities into devices and arrays [18, 57].

To fabricate such an electrophoretic flow detector, fundamental design considerations need to be made before proceeding to the microfabrication stage. These considerations include the selection of the membrane material and the definition of the geometry of the membrane and the pore itself.

3.1. Material Selection

3.1.1. Membrane

The selection of the membrane material requires precise consideration of its mechanical, electrical, physiochemical, and biological properties in order to provide optimal performance, both from a manufacturing and an operational point of view. Some of the characteristics that determine the suitability of a material as a membrane for the detector, such as polyimide (PI), polystyrene (PS), polycarbonate (PC), polyethylene terephthalate (PET), or polymethylmethacrylate (PMMA), are listed below [58, 59, 35]:

- *Mechanical Strength and Stability* – The membrane material needs to be able to withstand the typical forces that are generated during fabrication (e.g. thermal stress or point forces) and operation (e.g. differential pressure caused by the electrolyte). It should also be able to flexibly deform rather than rupture.
- *Membrane Durability and Lifetime* - The material needs to allow for a long device lifetime in order to be used in long-term experiments and be re-used for multiple experiments and analyses.
- *Optical Transparency* - Several microfabrication steps, such as alignment for systems integration, and many aspects of operations, such as filling the reservoirs with electrolyte, are facilitated significantly if the detector system is optically transparent. This allows for inspection under a microscope or for working with the device under a stereo microscope. In some cases, fine-tuning processes of the micro/nanopore are based on optical approaches. These require the chosen membrane material to be transparent.
- *Biocompatibility* -Biocompatibility is a vital issue to any medical and biomedical device or implant. It describes the suitability of a material for exposure to the body or bodily fluids. In the case of implants, a material will be considered biocompatible, if it allows the body to function without any complications such as allergic reactions or other adverse effects. In the case of biomedical detector systems, none of the biomolecules to be detected may be altered, degenerated, or even only change their conformation upon contact with the material, or else the measurements would be falsified. Biocompatibility requirements reduce the choice of membrane materials significantly.
- *Chemical Resistivity* - Chemical resistivity is required to ensure that the membrane does not alter in its intended operation. The environment is potentially aggressive including the

electrolyte solution or body fluids, and many materials could temporarily take up some water and swell, or permanently dissolve, causing loss of structure accuracy or even structure collapse.

- *Hydrophilicity* – From Greek 'loving water', or attracting water, such that the device can be wetted. This is a key requirement specific to the electrophoretic detector application and has proven to be one of the hardest conditions to meet in past studies: With decreasing pore sizes, it is increasingly difficult to ensure that the pore is at all, and entirely, filled with electrolyte, which would be the precondition for electrophoretic measurements. To support wetting of the membrane and its pore, the chosen material must be sufficiently hydrophilic. Good membrane hydrophilicity not only fundamentally allows any measurements, but also supports transport of the expected molecules through the pore, and helps to prevent their adherence or absorption onto its surface and pore wall.
- *Process Compatibility* - Manufacturing of a detector device entails a lengthy process chain, consisting of patterning, cleaning, and systems integration steps. Lithographic microfabrication of micro/nanopore in the membrane material, for instance, includes the exposure to energetic radiation and wet chemical development, the application of chemical rinsing and stripping agents, the exposure to elevated temperature, and possibly various postprocessing sequences. Systems integration exposes the membrane to glues and etchants. The membrane must withstand all of these in order to support the pore and warrant its fabrication with high geometrical accuracy and reproducibility.
- *Compatibility with optional Surface Modification Techniques* - After fabrication of the micro/nanopore, the membrane might be exposed to chemical modifications or chemical enhancement of its surface to increase its hydrophilicity/wettability or to introduce an

immobile phase. Another goal of surface modification might be to covalently attach different bioactive compounds which catalyze or elicit a specific response within a given biological system, for instance to capture elements such as antibodies. Therefore, stable and diverse modification of surface chemistry must be supported by the membrane material.

- *Thermal Properties* - To minimize thermal defects caused during the fabrication process, the material needs to possess good thermal properties, such as a high glass transition temperature T_g or a comparatively high thermal conductivity.
- *Electrical properties* - To minimize dielectric-breakdown effects when operating at modest to high electric field strengths, the membrane material needs to possess good electrical insulating properties.
- *Surface Charge Density* - The surface of a chosen membrane material needs to be homogenous in terms of the density of the charge that it is carrying; surface heterogeneity observed in some materials creates *spots* with non-uniform surface charge densities on the dielectric membrane, causing localized changes in the ionic current through the pore, affecting the electrophoretic efficiency.
- *Ionic Current Carrying Capability* - The membrane material needs to support the passage of a steady and stable ionic current through the pore, in order for the pore to be able to reliably detect the changes in the ionic current that are caused by the translocation of molecules through the pore. The surface charge of the membrane might be changed during the fabrication process, such as a UV-exposure for reflow-based post processing, or even during the operation of the detector system, depending on the pH value of the electrolyte solution. It must be possible to neutralize these charges on the membrane either

permanently using processes compatible with the material, or temporarily, to warrant the passage of a steady and stable ionic current through the pore [31, 38, 50, 60].

Polymer materials are promising candidates to meet most of the requirements mentioned above. Polymethylmathacrylate in particular has the additional advantage that it can be excellently micro- and nanopatterned. In the present research, PMMA is therefore applied as the membrane material for the fabrication of micro/nanopores forming part of an electrophoretic flow detector. In more detail, this selection is due to the following material properties:

PMMA can directly be patterned as the structural material. Other materials often just serve as a processing mask for subsequent etching, or get etched by themselves using a different processing mask. This eliminates the need for an etching step and therefore increases the potential structure accuracy and reduces potential minimum feature sizes. PMMA is compatible with different lithographic techniques, and has a proven and outstanding track record of high resolution patterning by electron beam lithography (EBL) and X-ray lithography (XRL) [42]. It is a transparent thermoplast, allowing for an optical feedback during fabrication (alignment steps) and operation (filling of reservoirs, electrode positioning, etc.). This is a benefit almost exclusive to PMMA, when compared to other competing materials. PMMA can not only be micro/nanopatterned, but it is also rigid and ductile enough to get machined. This allows for an almost unique opportunity to fabricate not only the membrane, but also all supporting components of PMMA. On a systems concept level, this enables integration in to the detector structure made of the same material (single-material integration). PMMA is rated excellent for its biocompatibility, several commercial grades (e.g. Plexiglas®) are even officially assigned US Pharmacopeia (USP) Class VI biocompatibility. It has therefore been used in many biomedical applications and microchip electrophoretic systems [31]. Its comparatively high hydrophilicity

(contact angle with de-ionized water was reported to be between 71.7° ± 1.5 and 73.7° ± 1 for comparable PMMA grades) supports wetting properties in the micro-fluidic domain [43]. PMMA, like many other micro-patterned polymers, tends to build up a negative surface charge during fabrication process, likely to a larger extent than observed in silicon-based materials. This could be disadvantageous for its intended uses. The charge build-up in PMMA can be alleviated, however, by a variety of different surface modification techniques, such as wet chemical methods, X-ray and UV-irradiation, and oxygen or air plasma treatment. The available surface modification techniques are able to not only neutralize the negative surface charges created on the PMMA membrane, but to also make the PMMA surface even more hydrophilic. These methods, however, can cause material damage and compromise the thermo-mechanical properties.

These properties made PMMA the preferred membrane material in this research. The monomer *methyl meth acrylate* has a molar mass of about 100 g/mol and a molecular structure as shown in Figure 3.1.

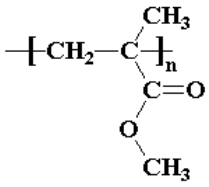

Figure 3.1: Molecular structure of methyl methacrylate, the monomer of PMMA.

Polymerization of these monomer units forms PMMA. PMMA can consist of up to tens of thousands of monomer units per macro molecule, with typical molecular weights M_w around 1 million g/mol. Table 3.1 highlights its advantages and disadvantages when compared to

competing, already published, non-polymer pore-based detector approaches. The competitors in the list are artificial pores in a silicon membrane, and natural protein pores in a lipid bi-layer. Trends highlighted in the table are based on a literature search [18, 33, 42].

Table 3.1: Summary of important flow detector properties based on different membrane materials, taking into account typical fabrication approaches.

Characteristics	PMMA-Based	Silicon-Based	Protein Pore-Based
Nano-patterning of membrane	Direct lithography	Etching	Self assembly
Single-Material Integration	Yes	Not usually	No
Optical Transparency	Yes	No	No
Pore Size Range/Tunability	Wide	Wide	None
Minimum Pore Size	Nanometers	Nanometers	Nanometers
Lifetime	Months/multi-usage demonstrated	Not reported	Hours/single use
Known Drawbacks	• Minimum pore size demonstrated • Surface charging	• Wettability • Noise levels • Reproducibility	• Tolerable environment (e.g. temp., pH)
Sensitivity of Pore Surface Properties to Processing Conditions	High	Low (can be increased by Self-Assembled Monolayers)	Low (can be increased by enzymes/proteins)

3.1.2. Detector System

While the membrane is the key component in the detector device, it is only one component in a larger system. The system needs to provide electrolyte compartments and an adequate support for the membrane as well as structures for assembly. The system also needs to provide a hermetic seal between the various components to avoid fluidic leakage. This is best ensured by minimizing the potential amount of thermal stress due to thermal expansion coefficient mismatches of different materials. Therefore, a single-material approach which uses the same

material with identical properties for all system components is desirable. Consequently, PMMA is chosen for all auxiliary components as well.

3.2. Geometry of the micropatterned Membrane

The dimensions of the membrane, the dimensions and the shape of the micro/nanopore itself, and the dimensions of the auxiliary components must be determined. They will all affect the overall performance of electrophoretic detector device, including its accuracy of detection and the quality of analyses of particles and molecules. In a first step, the membrane dimensions will be determined, ignoring the pore itself. As discussed in chapter 2, 2-dimensional finite element methods (2D FEM) are an appropriate tool to analyze the mechanical behaviour under different load cases for possible geometries. Results will be evaluated to determine best dimensional characteristics of the whole detector device.

3.2.1. Membrane Dimensions

As discussed in chapters 1.5 and 2.1, the membrane diameter D and the membrane thickness L have a strong impact on the patterning process and the structure quality of the pore as well as on mechanical stability, integration tolerances, and on the electrophoretic performance of the device. These aspects impose opposing requirements on D and L:

- A thinner membrane alleviates the micro-/nano-patterning processes, and the patterned pore can be wetted more easily. It will also result in an increased open pore current I_{open} under otherwise similar conditions, and therefore allows for a highersignal to noise ratio. But a thin membrane is more susceptible to failing under mechanical stress during fabrication and operation.

- A larger membrane diameter allows for less precise alignment during systems integration, which might enable manual processing without the need for additional equipment or active feedback. Larger membranes, however, are again more vulnerable to mechanical stress.

Therefore, a compromise between sufficient stability (thick, small membrane) and alleviated processing (thin, large membrane) as well as device performance needs to be determined.

PMMA membrane thickness and diameter are therefore numerically studied. For different geometrical setups, the von Mises stress is simulated as explained in chapter 2.1 as a model for the equivalent stress in a three-dimensional load case. Figure 3.2 illustrates a typical simulation result for a membrane in its critical situation. The load case is based on the geodetic pressure of only one entirely filled electrolyte reservoir, which is a typical temporary situation during filling the detector. The water pressure head can amount to a maximum of 3.68 mm (compare chapter 2.1), corresponding to a pressure of 36 Pa. For a membrane with 1 mm diameter, a thickness of at least 265 nm is required. In this case, the membrane would just barely survive the load, but no safety margins are available: The maximum von Mises stress is about 72 MPa, which is very close to the yield stress of 73 MPa taken from *ISO 527*. The yield stress is the material property associated with the load under which the PMMA membrane will start to rupture.

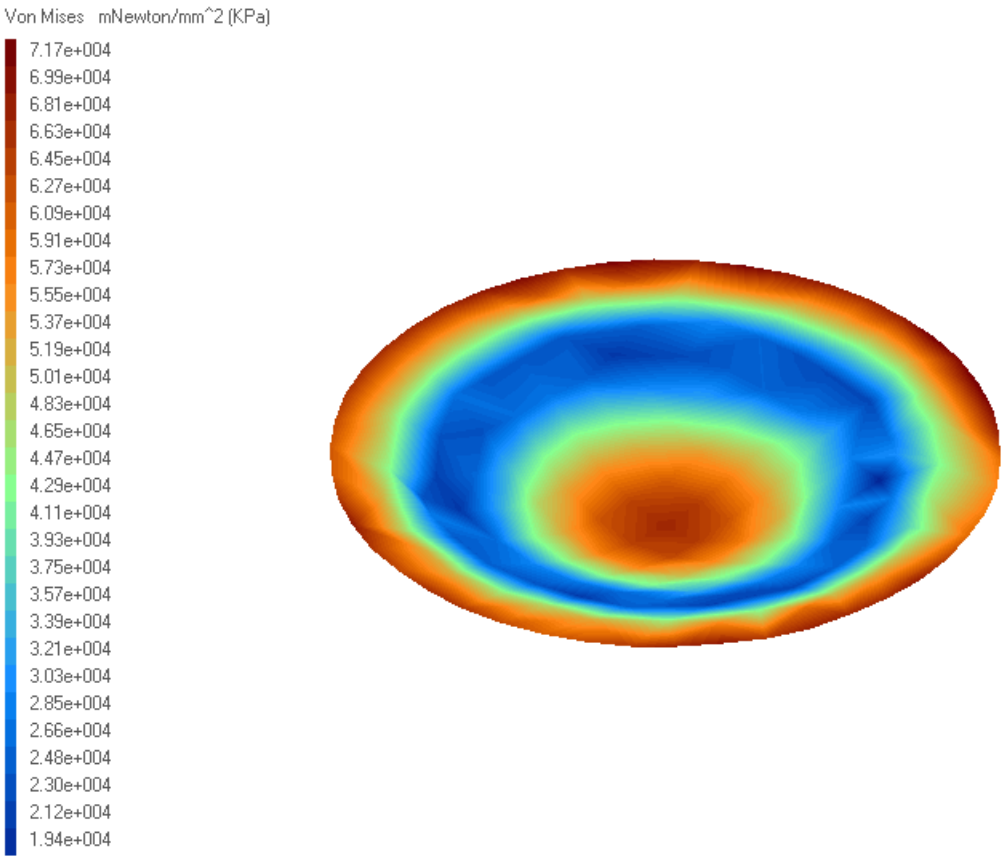

Figure 3.2: Simulated von Mises stress for a PMMA membrane with 1 mm diameter and 265 nm thickness under a pressure of 36 Pa.

Geometrical parameters are subsequently varied to find an optimum combination of thickness and diameter. Figure 3.3 illustrates how the maximum von Mises stress increases with decreasing membrane thickness and increasing membrane diameter respectively. The load case of an assumed electrolyte level of 3.68 mm is kept constant. At a fixed diameter of 1 mm, a membrane thickness of at least 265 nm is required, which is the specific case illustrated above. At a fixed thickness of 1000 nm, the maximum diameter is close to 4 mm. Further decreasing the

thickness or increasing the diameter would lead to a mechanical stress exceeding the yield stress of PMMA.

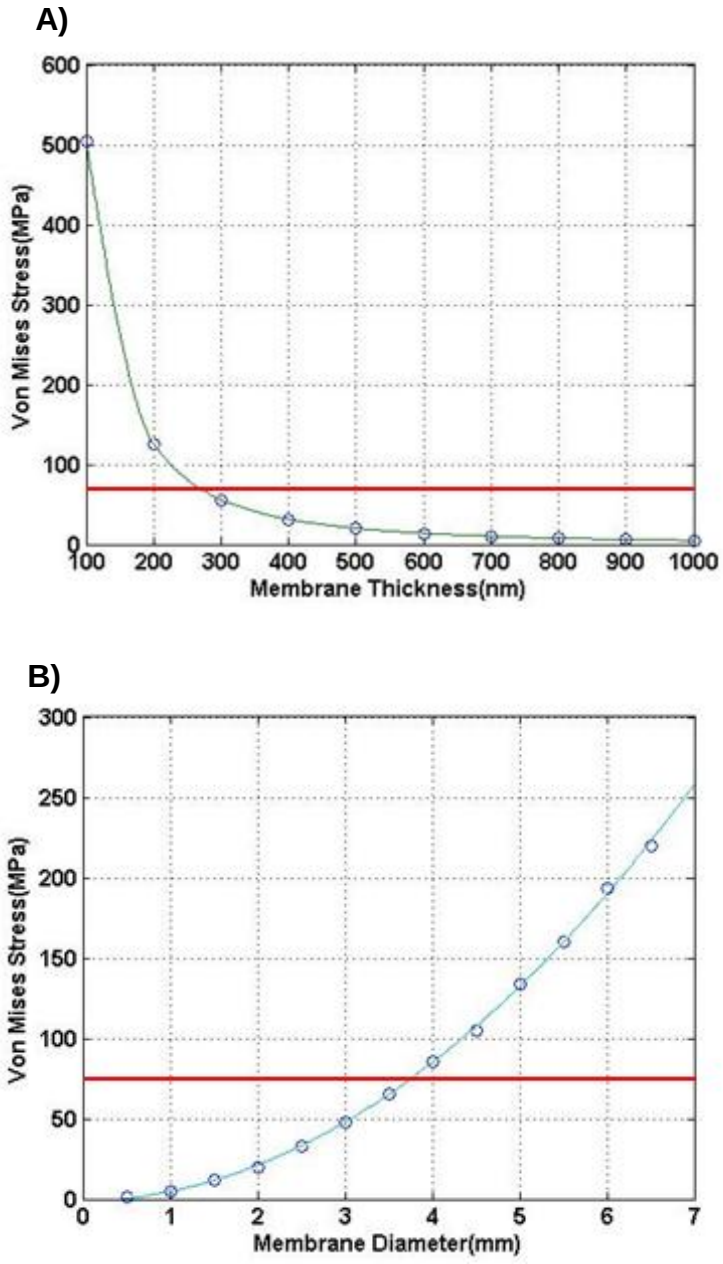

Figure 3.3: Impact of varied geometric parameters on the simulated maximum von Mises stress in a PMMA membrane under the geodetic pressure of 3.68 mm electrolyte. The horizontal lines

represent the materials properties-related limit for the acceptable stress (yield stress of 73 MPa): (A) Variation of the membrane thickness between 100 nm and 1000 nm at a fixed diameter of 1 mm; (B) Variation of the membrane diameter between 0.5 mm and 6.5 mm at a fixed thickness of 1000 nm.

The simulated geodetic pressure is only one of several contributions of stress on the membrane. Others include expected stress peaks during fabrication, such as during the membrane release step. A safety margin is therefore added to the simulated minimum membrane thickness of 265 nm at 1 mm diameter. This is anticipated to increase the fabrication process yield significantly, while compromising on the electrophoretic performance. A membrane thickness of 1 µm was considered to be a good compromise. In later experiments, such a membrane in fact never ruptured during operations, but a few did rupture during fabrication. Figure 3.4 shows the simulated stress distribution for the load case of 36 Pa geodetic pressure which formed the basis of the previous simulations as well. The maximum equivalent stress of about 50 MPa remains well below the yield stress of 73 MPa.

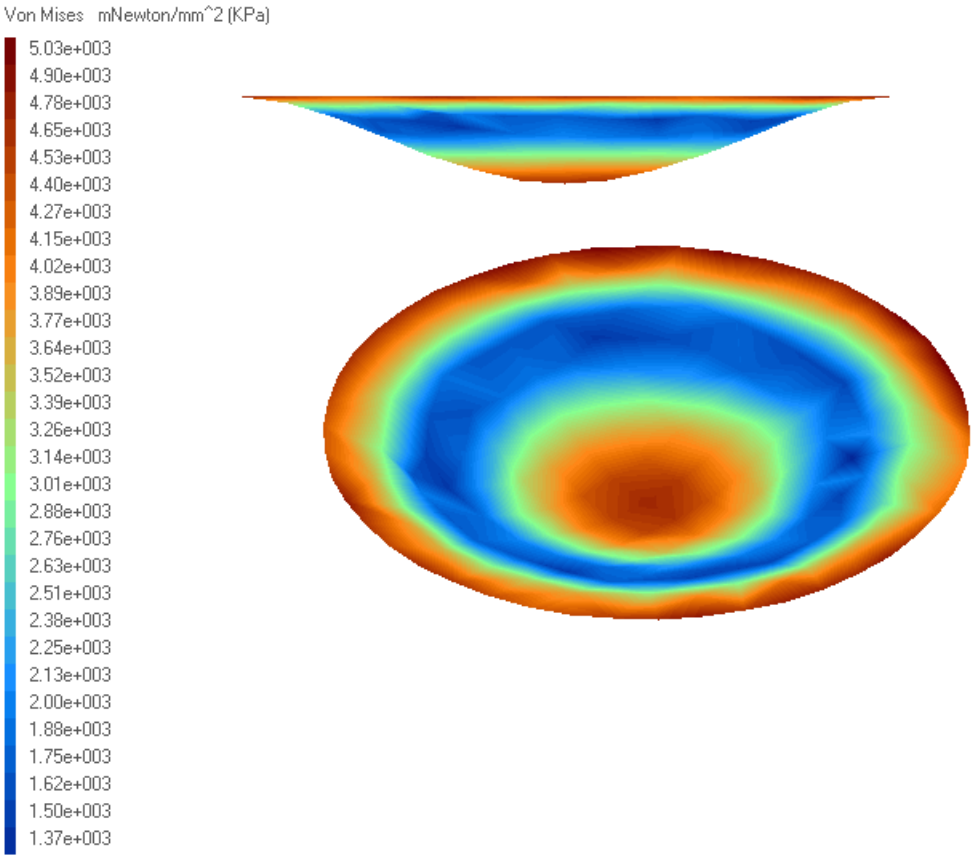

Figure 3.4: Simulated distribution of von Mises stress in an unpatterned PMMA membrane with 1 mm diameter and 1 μm thickness under a pressure of 36 Pa. Side view (top) and isometric view (bottom).

The membrane will slightly deform as a result of the differential pressure. The simulated stress translates into a maximum displacement of the center of the membrane of about 0.1 mm as illustrated in Figure 3.5. The graphical representation of the deformation is not to scale. During

actual operations, the displacement will be reduced as soon as electrolyte is filled into the second reservoir and the pressure gets compensated to a large extent.

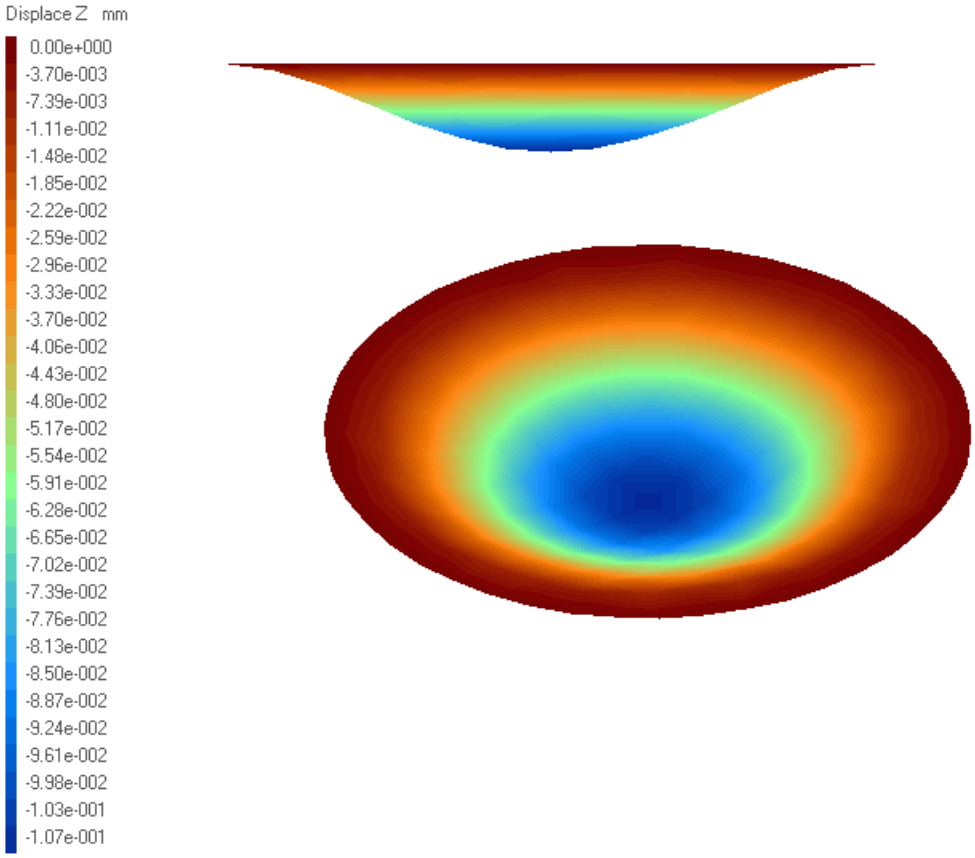

Figure 3.5: Simulated membrane displacement in a PMMA membrane with 1 mm diameter and 1 µm thickness under 36 Pa pressure. Side view (top) and isometric view (bottom), not to scale.

3.2.2. Pore Dimensions and Shape

As discussed in chapter 2, length and diameter of the pore are the important geometrical properties that will affect the detector device performance.

The pore length *L* is given by the membrane thickness *T* and has just been defined to be 1 µm in the previous FEM analysis section. The pore length not only affects the device stability, but

also its performance. According to the equation 2.6, a pore with a shorter length will provide a larger open pore current I_{open} at otherwise constant conditions. Since typical currents are on the picoampere scale, larger currents, corresponding to shorter pores or thinner membranes, are desirable for the measurements.

The pore diameter d can still be freely determined within the boundaries dictated by fabrication capabilities. A larger pore diameter will result in a larger open pore current I_{open}. A larger open pore current will have smaller relative fluctuations at otherwise similar conditions, or a better open pore signal-to-noise ratio. At the same time will particles of a given size create smaller relative temporal current blockades if the pore and open pore current are larger. If the pore diameter is too big compared to the diameter of particles/biomolecules to be detected, the large open pore current will only slightly change upon translocation, which impedes reliable detection. Eventually, some translocations might not get detected at all, which results in an underestimation of the frequency of translocations and therefore the particle concentration in the electrolyte [61]. Since current blockades constitute the key measurement signal, the primary goal is to maximize the signal change upon translocation of a particle to be measured. In other words, the diameter of pores in an electrophoretic biomedical detector should always be slightly larger, but comparable to the size of the biomolecule or pathogen to be detected. This facilitates monitoring and analysis of the obtained changes in I_{open} upon translocations through the pore [9] avoids underestimating the frequency of translocation events [61].

These considerations determine reasonable upper and lower limits of the pore diameter, depending on the size of particles to be analyzed. Particles, biomolecules, and pathogens of interest cover a wide range of sizes from a few nanometers up to several hundred nanometers. The largest pores to be fabricated are thus designed to have 1 μm in diameter. The smallest size

desirable would be a few nanometers and for our initial tests in reality is determined by the smallest feature that still has a reasonable process yield in 1 μm thick PMMA. We decided to plan for minimum feature size of 200 nm in a first detector layout. Pore post processing might be applied to further shrink that size.

The third important geometrical property of the pore, besides its dimensions given by length and diameter, is its detailed shape. Aspects of the pore shape cover its lateral shape in the plane of the membrane, and the shape across the membrane, along the pore. Analyzed particles of interest do span a wide range of diameter-to-length ratios, but are considered to be more or less rotation symmetrical. We therefore design our pores to be circular openings in the lateral plane of the membrane as well. The exact cross section across the membrane requires some more consideration. The pore width can be constant along the pore, which would correspond to a cylindrical pore. If the cross section gets narrowed or wider along the pore, i.e. across the membrane, the pore is conical. Naturally occurring protein pores sometimes feature even more complicated geometries as illustrated in Figure 1.6. This cross-sectional shape of the pore can affect the overall performance of the detector: Conical pores with an increased diameter at the front, or inlet, of the pore, for instance, may help to guide and orient molecules in the vicinity into the narrower constriction of the pore [14]. Therefore, conical apertures with such an orientation are anticipated to increase the frequency of translocation events of molecules through the pores, which could be advantages for samples with very low particles concentration in the electrolyte. Furthermore, conical pores are attributed to possess a reduced *effective length* compared to cylindrical pores. However, conically-shaped pores are extremely difficult to fabricate in a controlled and reproducible manner. We will, therefore, focus on microfabrication of cylindrical pores in 1 μm thick PMMA membranes.

3.2.3. Auxiliary Components of the Detector Device

To act as an electrophoretic detector, the patterned membrane needs to be supported and integrated into two chemically and mechanically stable reservoirs for the electrolyte solution, access paths for electrodes have to be provided, and a save stand must be added. A layout with a vertical orientation of the membrane will allow to minimize the differential pressure on the membrane. If the entire system is planned symmetrically, no additional considerations, e.g. with respect to the exact positions of the electrodes, are necessary. All components will be made of PMMA to follow the single-material approach discussed earlier.

Following these design considerations, the following auxiliary device components are laid out:

- two electrolyte reservoirs with openings at the top to fill in the electrolyte and to add the electrodes
- two rings to support the patterned membrane from either side
- two stands for the detector system

Figure 3.6 shows an explosion graph of these auxiliary components. The patterned membrane would be added right in the center. The alignment grooves in the support rings will be explained in detail further down and in the fabrication section in chapter 4.

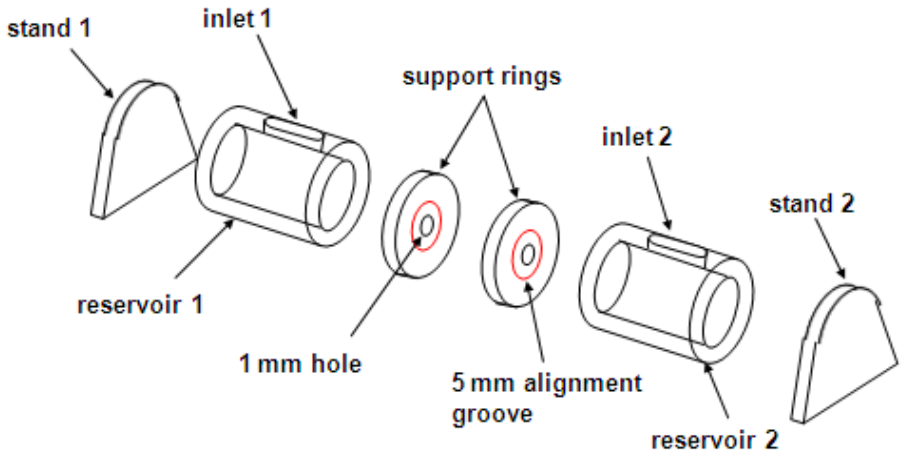

Figure 3.6: Explosion graph of the auxiliary detector components.

Details, including all dimensions, can be taken from Figure 3.7. Numbers are dimensions in millimeters. Section A-A, for instance, defines the overall system length to be 33.6 mm.

The electrolyte reservoirs are filled using the injection and drain inlets at the top. These inlets also allow to position two electrodes in the vicinity of either side of the membrane for the electrophoretic measurements. The reservoir dimensions are designed so that the head pressure cannot exceed the 3.68 mm limit defined in the FEM analyses. View B in Figure 3.7 illustrates how the geodetic pressure increases from top to bottom of the reservoir, assuming complete and one-sided filling. The maximum pressure 3.68 mm from the top, 36 Pa, was used as a constant pressure in the simulations previously discussed to cover a worst-case scenario. Since pressure is a scalar quantity, it is independent of direction, and the membrane orientation therefore has no impact under this worst-case assumption.

View A: PMMA disc in Figure 3.7 represents a support ring which will be mounted to the membrane to prevent the membrane from rolling up. The ring has a diameter of 13 mm and a

thickness of 300 μm. The thickness is sufficiently big so that the ring can offer the necessary support to the membrane. It is thin enough though to avoid trapping of bubbles during electrolyte filling. Much thicker rings could create air pockets and possible bubble creation during electrolyte filling, which would jeopardize proper pore wetting. This was observed in a previous layout where support rings of 1 mm thickness were used. The ring has a 5 mm alignment groove scratched centrically on one side using a precision tool with less than 50 μm tolerance. The center forms a 1 mm opening drilled through the PMMA which will define the area of the freely suspended membrane.

View A: PMMA membrane in Figure 3.7 represents the micropatterned PMMA membrane. The centre submicron pore is fabricated using Electron Beam Lithography (EBL). This pore is not visible with the naked eye or optical microscopy. Additional larger alignment structures are therefore added to the membrane during the EBL patterning process: Four 0.1mm wide alignment holes are evenly dispersed on a 5 mm diameter around the pore. These will be matched up with the 5 mm diameter alignment groove in the support ring while assembling under a stereomicroscope in order to center the pore in the 1 mm opening of the support ring (see *view A: membrane assembly*).

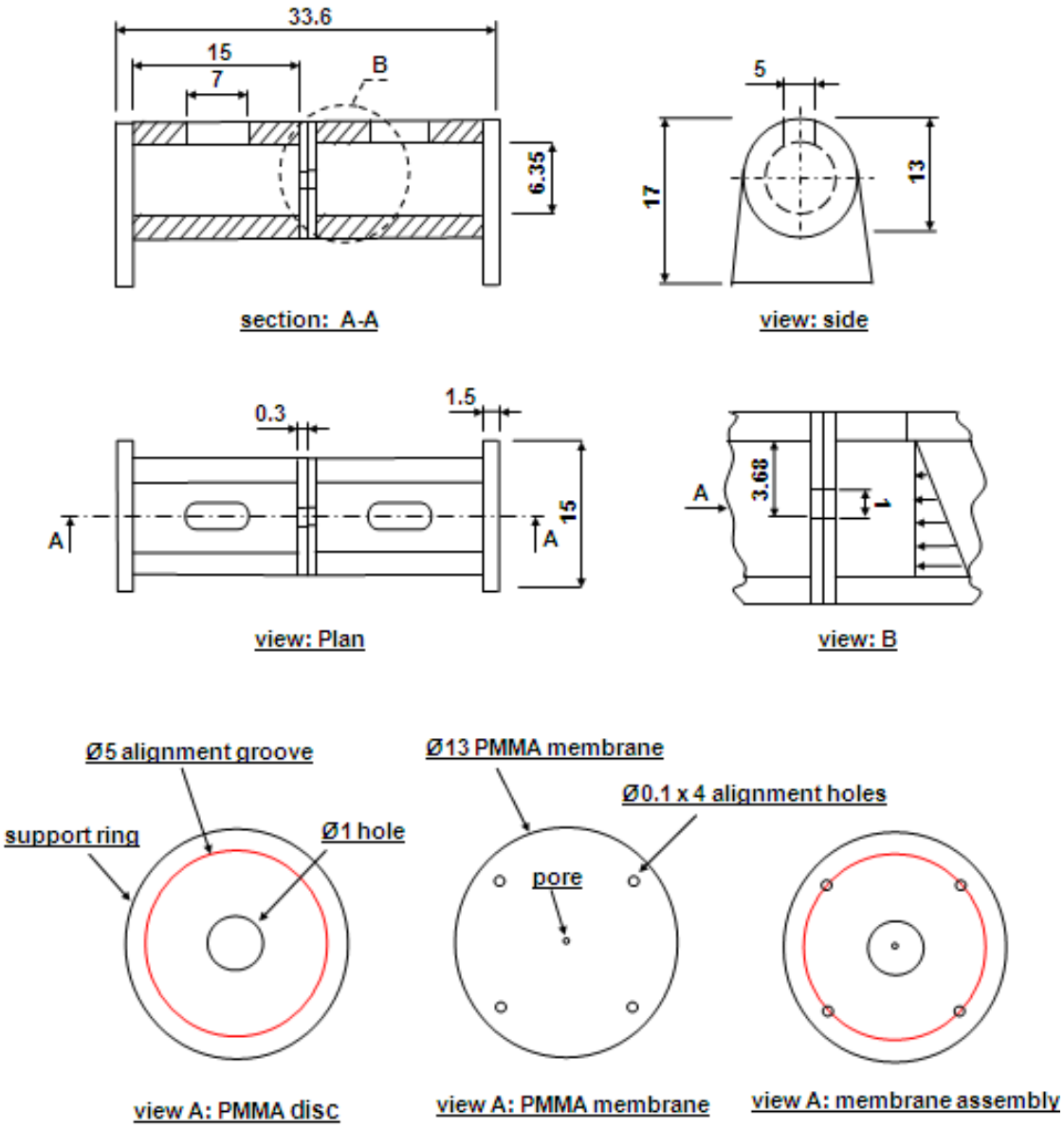

Figure 3.7: Overview and dimensions of the all-PMMA detector system components.

After appropriate materials were identified and all functional and auxiliary shapes and dimensions determined in this design chapter, the fabrication sequence will be discussed in the upcoming chapter.

4. Fabrication Procedure and Detector Integration

Based on the design considerations detailed in the preceding chapter, chapter 4 now focuses on developing and improving the fabrication processes for all individual components of detector devices. These include the fabrication and submicrometer patterning of the membrane using electron beam lithography (EBL), optional post processing of the pore to further reduce the diameter, mechanical microfabrication of the auxiliary PMMA components, and finally membrane release, alignment, and hermetic sealing of the components in a systems integration sequence.

4.1. Pore Fabrication by Electron Beam Lithography

The membrane is fabricated on a silicon wafer as a sacrificial substrate. The first step in the fabrication sequence comprises cleaning of the substrate with acetone to remove potential debris from the wafer surface. PMMA is then spin-coated to form a 1 μm thick film. Parameters are 2500 rpm for 45 seconds using PMMA 950 A8 by MicroCHEM. It is a PMMA grade with a molecular weight of M_W = 950,000 g/mol with a solid content of 8%, dissolved in anisole. Subsequent baking in a convection oven is done at 170°C for 30 minutes.

The third step is micro- or nanopatterning the film. This step is the key to the future device performance as it determines, to a large extent, the structure quality and accuracy of the pore. As discussed in chapter 1.5, electron beam lithography (EBL) is applied in this research. PMMA is particularly well suited for patterning by EBL as it is one of the highest contrast, standard resists. Feature sizes down to a few nanometers can get fabricated using optimized process conditions. The fabrication challenge is to produce small pores in comparatively very thick resist. The aspect ratio, defined as the ratio of resist thickness to minimum lateral feature size, does not usually

exceed 2 or 3. Pores with diameters smaller than 500 nm in the 1 µm thick PMMA film will therefore need significant process optimization. Furthermore, scattering effects of incident electrons widen the electron beam in the resist resulting in non-vertical walls and poor structure quality. Cylindrical pore can only be fabricated at high initial electron energies, i.e. high acceleration voltages, and on a substrate with minimum back-scattering.

The penetration depth of electrons has been empirically determined by Schonland [62] as

$$D_p = K''.10^{-12}\frac{V^2}{\rho} \tag{4.1}$$

where D_p is the penetration depth, K'' is an empirical coefficient equal to 2.1, ρ is the density of the exposed material, and V is the accelerating voltage. Figure 4.1 plots this formula of the electron penetration depth in PMMA as a function of the accelerating voltage. To even allow electrons to propagate 1 µm into the PMMA, an acceleration voltage of at least 8 kV is needed. Higher voltages will improve the structure quality achievable. The highest acceleration voltage available in reasonable distance to our laboratory is a Raith 150 EBL electron beam writer with up to 30 kV acceleration voltage, located at the University of Alberta NanoFab in Edmonton. It is represented by the vertical line on the left in Figure 4.1 Higher acceleration voltage writers are fabricated, for instance, by Elionix, Tokyo, Japan, who have demonstrated 15 nm wide lines in 1.5 µm thick resist with a 120 kV machine (represented by the vertical line on the right in Figure 4.1).

In this study, we use 30 kV with an exposure dose finally set to 315 µC/cm^2 to transfer the pattern. Future tests should be made using dedicated beam writers with increased acceleration

voltage. A 50 kV writer (Jeol JBX-6000) would be available in eastern Canada at the National Research Council Institute for Microstructural Sciences, for instance.

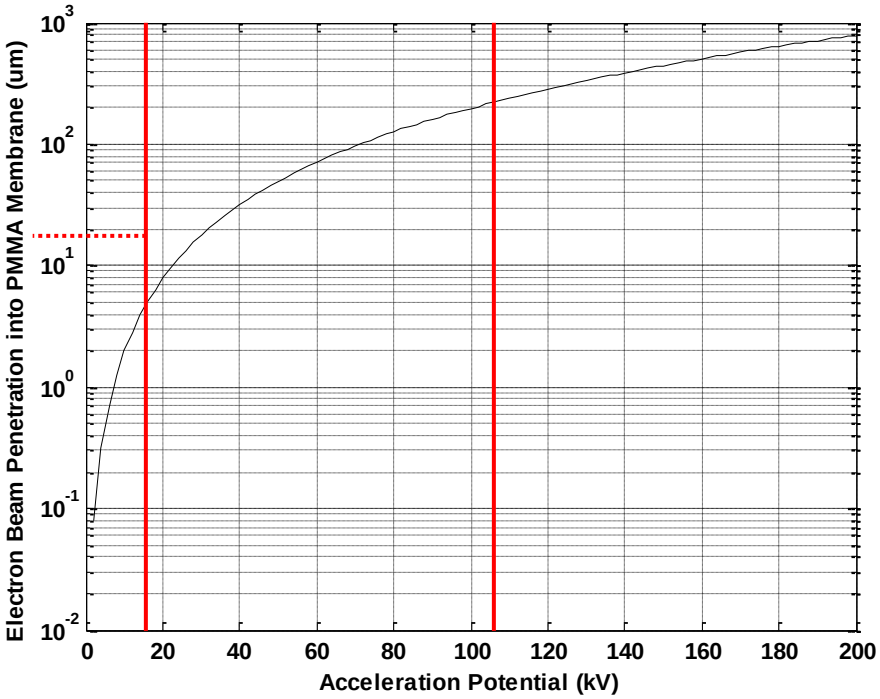

Figure 4.1: Electron penetration depth in PMMA as a function of the accelerating voltage. Acceleration voltages of 30 kV used in this study (Raith) and 120 kV as an example of a high voltage writer (Elionix) are highlighted by vertical lines.

Exposed PMMA areas undergo a reduction in molecular weight due to chain scission and become soluble in a 1:1 mixture of methyl isobutyl ketone and alcohol (MIBK-IPA)[63]. This dip development is performed for 60 seconds at room temperature. Figure 4.2 sketches these basic lithographic steps.

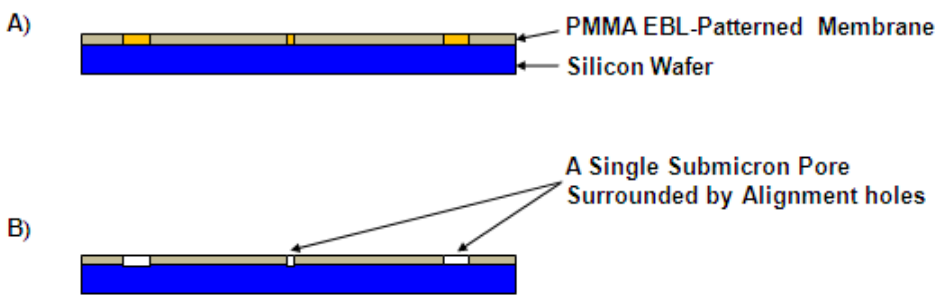

Figure 4.2: Schematic representation of basic steps involved in the lithographic patterning of submicron pores in a PMMA film: (A) electron beam exposure; (B) development of a submicron pore surrounded by alignment holes.

The initial test layout consists of a redundant array of circular pores, ranging between 200 nm and 1 µm in diameter. Each pore is surrounded by four auxiliary microscopic alignment holes of 100 µm diameter on a 5 mm diameter for optical alignment of the pores relative to the support ring (see Figure 3.7).

To evaluate the results of the EBL patterning and the development processes, Atomic Force Microscopy (AFM) and Scanning Electron Microscopy (SEM) measurements were used. Figure 4.3 depicts AFM measurements of a pore with 300 nm nominal size. The data was obtained using a Digital Instruments/Veeco Dimension 3100 AFM in tapping mode, applying a standard Tapping Mode silicon probe. The measurement was taken with the pore still on the Si wafer, i.e. the PMMA membrane was not yet released. The measured pore geometry is a convolution of the actual pore size with the tip geometry. This convolution is the reason why the hole appears to be trapezoid rather than round, showing different sizes in x-direction (≈ 400 nm) and y-direction (≈ 300 nm). Assuming the smallest measured values to be most accurate in this

context, the nominal size of 300 nm seems to be close to the actual size at resist top. Actual measurements are hard to perform, though, since roundings at the AFM tip and PMMA surface roundings do not clearly indicate where the pore starts. AFM measurements also a-priori preclude statements on the sidewall verticality.

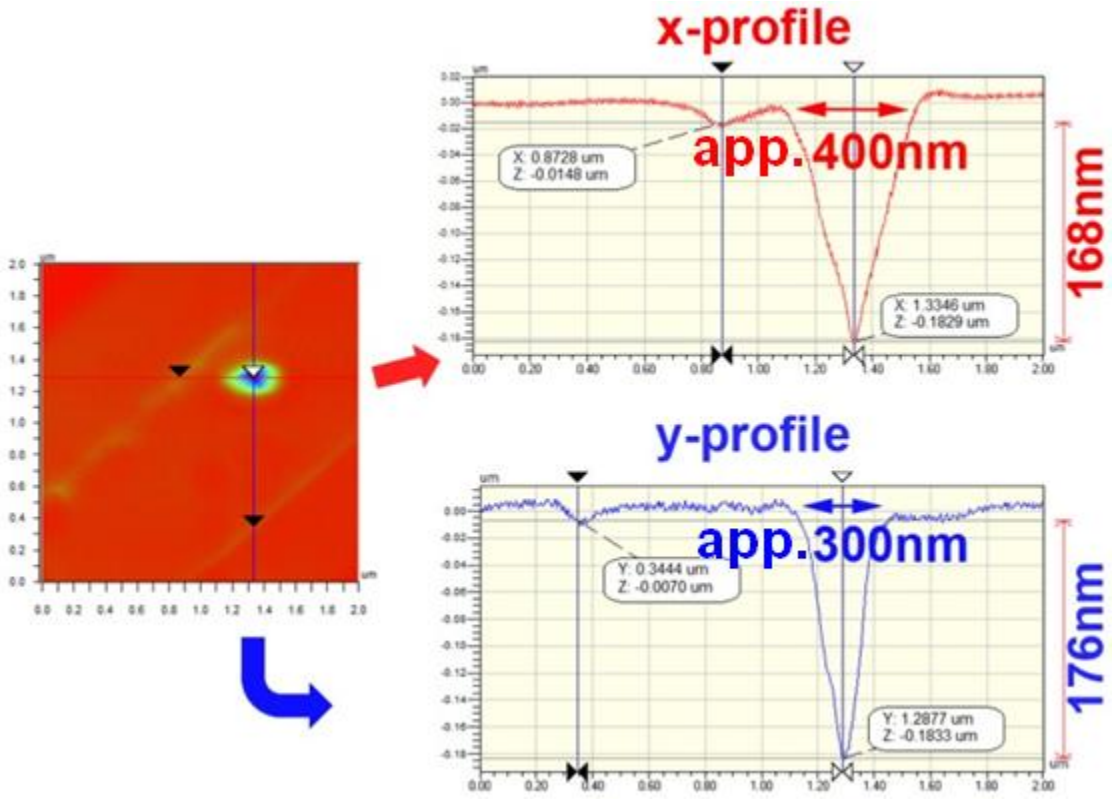

Figure 4.3: AFM measurement of a 300 nm pore before release from the silicon wafer, courtesy Varshni Singh, CAMD, Louisiana State University.

Additional data was obtained from the same pore, using a field emission scanning electron microscope (SEM) at the Louisiana State University (LSU) in Baton Rouge, USA, Center for Advanced Micro Structures and Devices (CAMD). Figure 4.4 was imaged without conductive coating. While SEM imaging is not technically considered a calibrated measurement, a good

approximation of actual sizes can still be obtained. The image reveals that the pore does not have a perfectly round shape, and is slightly oval. It is wider than high in this graphical representation, but not as deformed as alluded by the convoluted data obtained using an AFM tip. The surface size is approximated to be within 30 nm of the nominal diameter, with a width of 320 nm ±5 nm and a height of 292 nm ±5 nm. Further imaging with modified contrast and brightness settings did not reveal any obstructions within the pore further down in the resist, but did not allow for measurements down in the resist.

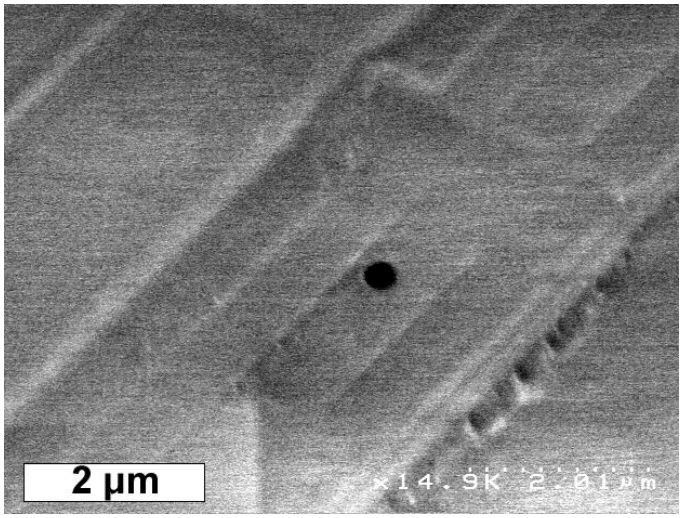

Figure 4.4: SEM image of the same 300 nm pore in a 1 µm thick PMMA membrane before release from the silicon wafer, courtesy Varshni Singh, CAMD, Louisiana State University.

4.1.1. Fine tuning the Diameter of Single Pores

Under the given geometrical and lithographic conditions, minimum pore diameters using the EBL technique available for this research are about 200-300 nm. This would suggest an application for the detection of particles in the 100 nm to 150 nm range. Those biomolecules

with much smaller diameters would however require smaller pores. Many biomolecules feature a diameter of about 10 nm. These would best be measured with pores of approximately 20-25 nm in diameter. EBL will not readily allow to pattern a 20 nm pore in 1000 nm thick membrane. This would equate to an aspect ratio of 50:1 and is far beyond typical limits. Optimized writers, substrates, and processing would be required. However, the use of polymer membranes offers an elegant opportunity to postprocess the EBL-patterened pores. To create a smaller pore, an optional post-processing technique is, therefore, developed in this study for fine-tuning the diameter of the pores. If applied, this processing step will follow later on in the fabrication sequence after the membrane has been released from the wafer and integrated into the support ring. To give a consistent overview of the nanopatterning of the pore, however, the postprocessing option is further described here.

Such a reflow process can be performed without compromising the structural integrity of the membrane. In the case of round pores, this reshaping can significantly reduce the pore diameter. We introduced the surface energy model in chapter 2.2 which theoretically describes this fine tuning process. The published procedure is modified for implementation using UV exposure rather than electron beams. In chapter 2.2, boundary conditions were developed which have to be satisfied in order to reduce the pore diameter upon exposure. These conditions are met for the EBL patterned pores in this research. As an example, a 450 nm pore was shrunk by about an order of magnitude to a diameter of approximately 22 nm: Under the impact of an intense, broadband UV point source using a mercury vapour lamp without additional filters (OmniCure 1000, EXFO Life Sciences, Mississauga, Canada), exposure with an intensity of 3600 mW/cm^2 for a few second results in repeatable pore size reduction. Process parameters

were developed in iterative attempts until the above mentioned dose resulted in the size quoted. Further details will be given in chapter 5.1.

4.2. Fabrication of Auxiliary Device Components

According to the detector system designed in chapter 3, each detector consists of the patterned membrane as well as six auxiliary components. These additional components are two electrolyte reservoirs, two support rings to support and protect the membrane from either side, and two stands to support the entire detector system. Figure 3.6 in chapter 3 gave an overview, and Figure 3.7 specified details and dimensions. These components are milled using conventional machine shop tools. The components are thoroughly cleaned in an ultrasound-supported bath with de-ionized water to remove all debris created during fabrication.

4.3. Detector System Integration

The patterning of the membrane was carried out on a sacrificial silicon wafer to ensure reliable and repeatable process conditions, including flat surface topography and definite positioning in the EBL writer. In operation, this silicon wafer will have to be removed as it blocks the submicron pore. While releasing the membrane from the wafer, high mechanical and thermal stresses are likely to appear, depending on the release process selected. Either might compromise or even rupture the membrane. Additionally, the membrane might simply roll up upon release from the wafer due to a non-uniform stress distribution. Once rolled-up, a 1 μm thick membrane will not be usable anymore. Therefore, prior to the release process, the membrane must get supported properly. This is achieved by attaching a PMMA support ring onto the membrane. Considerations for the support were already commented on in chapter 3.2.4 and include:

- The PMMA support ring must be rigid enough to support the membrane and thin enough to avoid trapping of bubbles during filling with electrolyte. With a central hole of 1 mm, a thickness of 300 μm was selected as a compromise.

- The central hole in the support ring has a diameter of 1 mm. This dimension determines the size of the freely suspended membrane. The submicron pore is supposed to be in the center of the 1 mm hole. This allows for a tolerance of ring misalignment on the membrane as well as excess glue emersion of up to 500 μm.

- Attaching the support ring entails alignment to the patterned membrane, mounting, and hermetically sealing. The overall error budget is 500 μm.

The alignment of the support ring to the nanopore is a challenge among others because the nanopores are beyond the diffraction limit and therefore cannot be detected optically. Alignment holes of 100 μm diameter as designed in chapter 3, Figure 3.7, and repeated in Figure 4.5 (left), are used. The alignment groove illustrated in the same Figures is placed onto all 4 alignment holes simultaneously, using a stereo microscope for inspection. The desired result is sketched in Figure 4.5 (right).

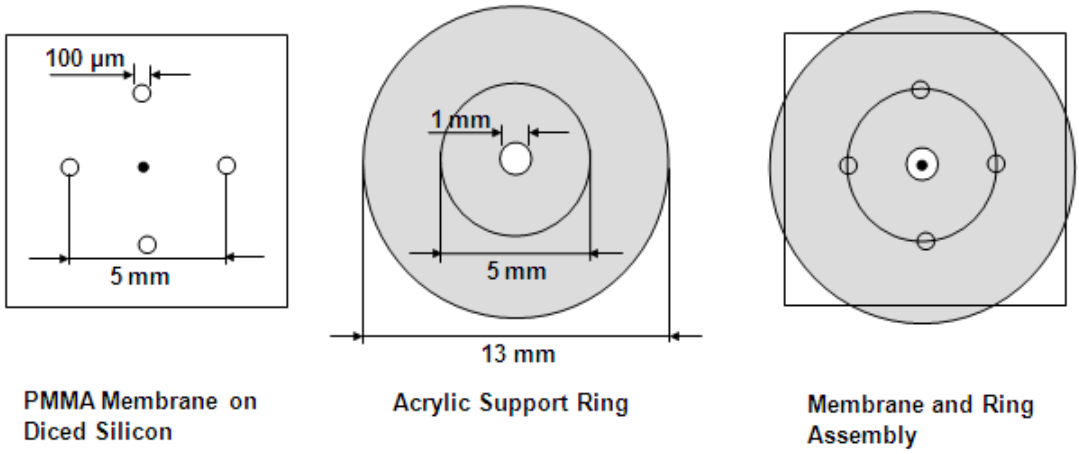

Figure 4.5: Schematic illustration of a single pore and four 100 µm alignment holes in the membrane (left) and of an alignment circle on the support ring (center). Aligned assembly (right). Sketches are not to scale.

For the 75 samples assembled, the observed misalignment usually was less than 100 µm and never exceeded 300 µm. This leaves an error budget of 200 µm to 400 µm for excess glue later on in the integration process:

An additional challenge was to attach the aligned support ring to the membrane while the membrane is still mounted onto the silicon wafer. In many MEMS systems, it would be sufficient to just attach the ring so that it adheres. In the case of an electrophoretic application, however, it must be guaranteed that not even a single nm-sized particle can pass between membrane and ring, or else any detector signal would become obsolete. In other words, a hermetic seal is needed between membrane and ring. This seal must also be process-compatible, i.e. withstand subsequent processing steps. It must be transparent not to impede the optical alignment process. And it must be proven to be biocompatible so the assembled device may still

be used for biomedical applications. Thermally connecting the two PMMA surfaces would compromise the nanostructure in the membrane. Therefore, gluing the components together is the approach of choice. Preliminary studies were carried out to find a process- and biocompatible, transparent, hermetically sealing glue that does not drag into the pore. Two components glues were not successful due to the high typical viscosity and long curing times. The first impedes a hermetical seal and the second prevents stopping the drag flow of the glue once it gets critically close to the pore. Therefore, another class of glues that features a very low viscosity and solidifies immediately when needed was tested. These are UV initiated glues that harden upon UV exposure. This glue first quickly flows, under the impact of capillary pull, to all areas of interest and hence creates a complete film and hermetic seal. Once all areas of interest are filled, further progress can be stopped by exposing the glue for a few seconds. This immediately increases the viscosity and eventually leads to solidification. This approach protects the pore from getting clogged with glue. Unwanted emersion of glue is also limited by the inner edge of the support ring. While capillary forces will drag the glue through the thin gap between membrane and ring, at the inner edge, this capillary pull ends.

In this research, we used the meth-acrylate-based photo-initiated glue Dymax 191-M. It has biocompatibility approval, USP class VI. The UV point source previously described, Omnicure 1000, was equipped with a band-pass filter for wavelengths from 320 to 500 nm and positioned 5 cm from the target area. Full solidification was achieved after 10 seconds. Such exposure heats up the membrane, potentially deforming it. Exposure conditions must therefore take into account the solidification as well as the thermal process. If longer exposure times were required, multi-step exposures could have been applied to ovoid thermal effects.

The situation after aligning and attaching the support ring to the patterned membrane is graphically represented in Figure 4.6 A.

The next processing step is to release the sandwich of membrane and support ring from the sacrificial silicon wafer. Three potential options are:

- *Back-side etching of the sacrificial silicon substrate:* Selectively dissolving the silicon substrate can be achieved using a 30 % potassium hydroxide (KOH) solution at T = 80°C in about 7-10 hours. This option is not suitable in our system since it appeared that minor impacts to the PMMA pore were observed. These were impacts on the nanometer scale, potentially related to thermal effects or swelling, and those would not likely be an issue in most other applications.

- *Etching of a sacrificial intermediate layer between film and silicon substrate:* This approach requires the deposition of an additional interface layer before the deposition of the polymer at the beginning of the process sequence. For example, titanium (Ti) can be used as such a layer and selectively get etched with hydrofluoric acid (HF). Dissolving the intermediate sacrificial titanium layer using a 5% solution of HF 50% at T = 20°C suffers from the extremely slow etch progress along the thin Ti layer. Up to weeks of processing time were required in initial tests, depending on the layout.

- *Capillary force release:* Releasing the sandwich from the silicon substrate using capillary force rather than etching any layer is the third option. Once a tiny area starts to separate from the substrate, further delamination is supported by capillary forces since the sample is submersed in de-ionized water. Gentle cycling between two moderate temperatures (20°C and 80°C) adds slight thermal stress and helps with the delamination. This option seems to

offer a very gentle release and therefore is considered the best approach for our fabrication process.

Therefore, release of the membrane-support ring sandwich is performed by capillary forces. The process was supported reducing the surface tension with the bio-degradable, non-ionic surfactant *Triton X-100*. It contains Iso-octyl Phenoxy Polyethoxy - ethanol and Ethyleneoxide. Typically after a few hours of gentle thermal cycling in 10 min intervals, the membrane detached from the silicon wafer. The upper temperature of 80°C is below the glass transition temperature of bulk PMMA (T_g > 100°C) and therefore save to apply without permanent deformations to be anticipated. However, since UV treatment of the PMMA membrane is applied prior to release, and since such treatment is known to reduce the glass transition temperature, this upper temperature might actually be a little high and contribute to pore reshaping observed after release as discussed in chapter 5.2 Future experiments will be carried out with reduced temperatures [64].

The release procedure nevertheless delivers freely-suspended, patterned PMMA membranes protected by an acrylic support ring on one side, as illustrated in Figure 4.6 B.

In a subsequent step, an acrylic support ring, similar to the one already attached to the top surface of the membrane, is glued to the other side of the membrane in order to prevent the freely-suspended PMMA membranes from mechanical scratching during the next fabrication steps (Figure 4.6 C).

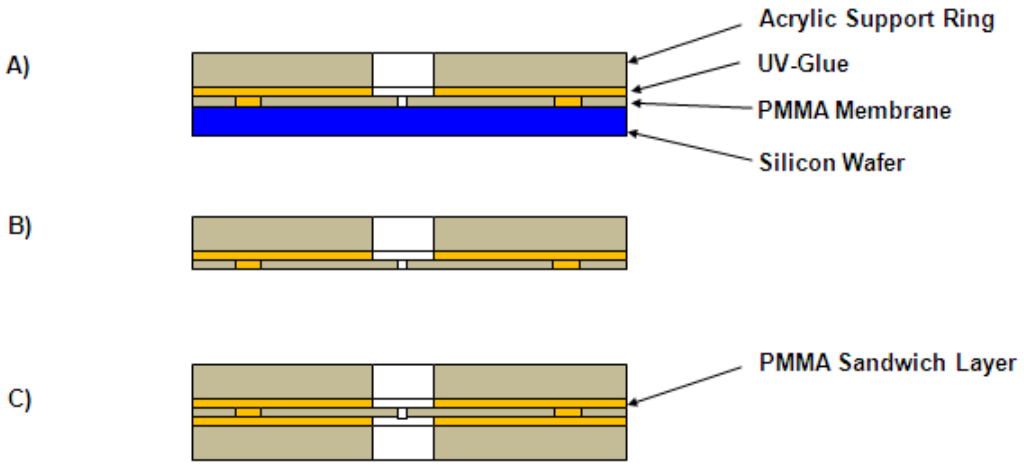

Figure 4.6: Schematic representation of the steps involved in the release of the patterned PMMA membrane from the sacrificial silicon wafer: (A) A PMMA support ring is actively aligned and UV glued to the membrane; (B) The sandwich of support ring and membrane is released from the silicon wafer by capillary forces and thermal cycling; (C) A second PMMA support ring is UV glued to the back side of the released sandwich.

In the last integration step, the support ring-membrane-support ring sandwich is assembled with two reservoirs and two stands to form a complete electrophoretic flow detector system. The reservoirs and their stands were introduced and specified in chapter 3.2.3. The assembly of the final detector components is achieved using the same UV glue introduced above. Figure 4.7 shows a picture of such an assembled electrophoretic flow detector device with an overall length of 33.6 mm. Each reservoir has a filling capacity of about 0.45 ml and contains an upper inlet. These inlets will allow to introduce electrolyte and electrodes in preparation of experiments. The horizontal orientation of cylindrical reservoirs and vertical orientation of the membrane reduces the pressure on the membrane during filling of the electrolyte, facilitates electrolyte filling

without formation of bubbles, and also allows for identical positioning of the electrodes with respect to the pore. Electrodes are placed approximately 5 mm apart from the PMMA membrane through the upper inlets. The freely-suspended PMMA membrane in the center contains a nanometer-scaled pore which forms the only permeable component of the whole detector device.

Figure 4.7: Micrograph of a complete, all-PMMA electrophoretic flow detector device.

4.4. Self-Assembly of α-hemolysin Protein Pores

In the previous chapters it was discussed how pore diameters down to a few hundred nanometer are fabricated by EBL using a top-down fabrication approach. If smaller pores are needed, the pores are post processed exploiting surface tension to decrease the pore size by one order of magnitude. Pore diameters of 20-25 nm can then get reliably fabricated. Our current micro and nano fabrication sequence does not allow to fabricate pores that are yet 1 order of magnitude smaller. However, in order to detect single stranded nucleic acid (ssDNA), pore diameters of about 1.5 nm would be needed.

While working on further improvements of top-down nanofabrication sequences in PMMA, a bottom-up approach was developed to generate 1.5 nm pores in the PMMA detector system. This

alternative exploits naturally occurring protein pores. It therefore somewhat diverts the all-PMMA concept and also reduces the size expectancy of the diameter. But it allows testing the system as a whole and predicts future performance when the protein pores will be replaced by artificial ones. In this rapid prototyping approach, α-hemolysin protein pores were selected, and a fabrication sequence was developed to allow integration of such pores into a PMMA system.

α-hemolysin protein pores have been extensively employed over the last decade for probing the structure and dynamics of biomolecules such as single-stranded nucleic acids (ssDNA) under a range of experimental conditions [10, 65, 66]. Such protein pores have been previously integrated into silicon-based systems [67], while we now develop a technique to allow for their implementation into a polymer micro-device.

In a first step, a lipid bilayer membrane is suspended across a hole in a PMMA layer. Subsequently, a protein nanopore is introduced directly into the suspended lipid bilayer membrane. Since the forces involved in the process of attaching the lipid bilayer membrane to the PMMA are comparatively high, the PMMA layer needs to be more robust than the 1 µm membrane applied so far. Instead of using a spincoated membrane, we now directly apply the micro machined PMMA ring of 300 µm thickness as a support structure. The inner hole, which previously was 1 mm, needs to be reduced to 100 µm to alleviate stress on the lipid bilayer to be mounted later on. Since mechanical microfabrication results in burs and other artifacts that could compromise the vulnerable lipid bilayer, an acrylic ring is first prepared with an inner diameter of 200 µm. This hole is then exposed to a post processing sequence similar to the one used to reshape EBL patterned nanopores: The PMMA hole is exposed to an intensity of 3600 mW/cm^2 for a few ten second in a broad band UV spectrum from 250 nm to 650 nm. As explained in chapters 2.2 and 4.1.1, surface tension will smoothen the rim of the pore and shrink its diameter

to about 100 µm. The post processed ring is then integrated in to the detector system as described in chapter 4.3. Finally, the lipid bilayer and the α-hemolysin pores are added: A lipid bilayer membrane is formed across the prepared micropore by dipping a paintbrush into a lipid solution and painting across the micropore as described by Stefureac et al. [14]. This comparatively forceful process is the reason why a PMMA ring is used instead of a thin membrane. The lipid solution is purchased from Avanti Polar Lipids Inc. (Alabaster, AL), vacuum-dried for 4 hours, and re-dissolved in decane to a final concentration of 30 mg/ml of lipid. Formation of a stable lipid bilayer membrane across the micropore is identified by a complete blockage of the open pore current I_{open} through the micropore in the acrylic layer, when tested in a patch clamp setup. In the final step, the pre-formed lipid bilayer membrane provides support for the protein nanopores of α-hemolysin. α-hemolysin pores, purchased from Sigma-Aldrich (St. Louis, MO), are prepared to a solution with the final concentration of 1.25 µg/ml. Using a pipette, these α-hemolysin pores in solution are now self-assembled into the prepared lipid bilayer membrane by injecting a total of 5 µl of above protein nanopore solution adjacent to the micropore in the PMMA layer. Performed during patch clamp testing, protein pore insertions and their self-assembly are immediately detected by a characteristic jump in the I_{open} value. According to Stefureac et al. [14], each inserted protein pore results in an I_{open} value of approximately 100 pA, when an external potential of + 100 mV is applied across the membrane.

In chapter 4, a complete fabrication process for an all-PMMA electrophoretic flow detector for biological applications was proposed. Cylindrical pores were microfabricated in PMMA membrane using electron beam lithography. Auxiliary components of the detector were fabricated using conventional machining techniques. An optional post processing procedure was introduced to fine-tune the pores, reducing the diameter by one order of magnitude as required

by selected biological applications. The entire detector system was aligned and assembled using UV-initiated glue. An alternative fabrication sequence is based on self-assembly of biological protein pores.

5. Detector Test Results and Discussion

After explaining the design and the fabrication of detector devices in the previous chapters, the detectors now need to be tested. In this chapter, the functionality of the detector devices is evaluated using both, test nanoparticles and two different biomolecules. The initial steps in testing such detector devices are determining the actual pore size, verifying the nanofluidic integrity of the entire system by analysing the open-pore current, and calibrating the detectors by evaluating the current blockade induced by nanoparticles of known sizes. At the end, the two biomolecules are detected and their translocation dynamics are compared with each other.

5.1. Patch Clamp Test Setup

The electrochemical chambers discussed in the previous chapters were fabricated and assembled using different pore sizes between 1.5 nm and 450 nm. To be used as an electrophoretic detector, an electrolyte needs to be added along with two electrodes. A power supply delivers precise, constant, and adjustable voltage levels. Picoammeters with response times better than milliseconds are needed in an environment that is preferably electromagnetically shielded. In our lab, we used a setup as illustrated in Figure 5.1. It consists of an amplifier (Axopatch 200B, Axon Instruments) which provides electric potential range from -1 to +1V and also amplifies the ionic resistive pulse, a digitizer (Digidata 1440A) that acts as analog to digital signal convertor, and a Faraday cage comprising a peltier cooled headstage (CV 203BU) to minimize the thermal noise, the microfabricated detector device, and two Ag/AgCl electrodes.

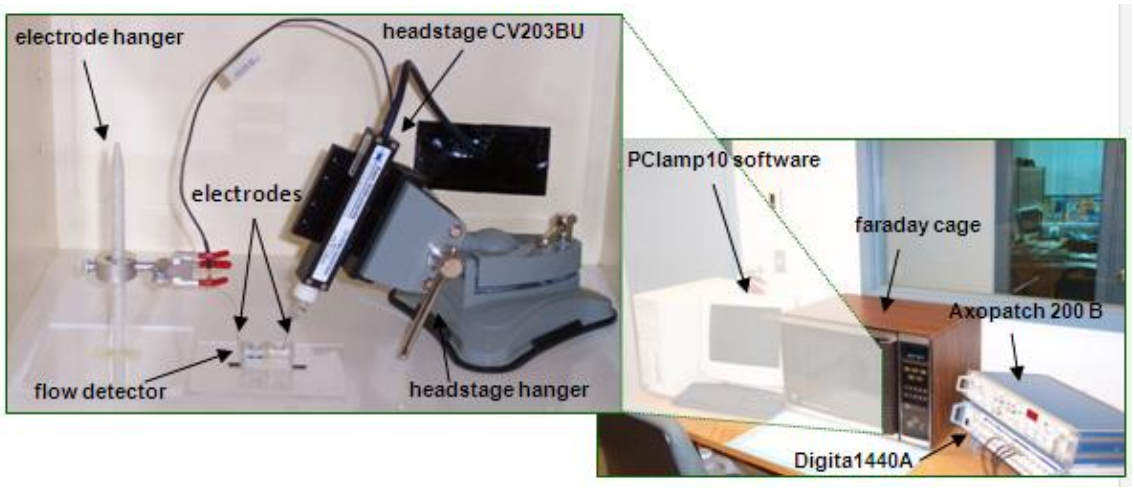

Figure 5.1: Patch clamp setup: Overview (right) and close-up of the Faraday cage with the microfabricated detector (left).

Figure 5.2 gives a simple block diagram of the setup. All cables are coaxial. BNC connectors are used between amplifier and digitizer. The open pore current I_{open} and its variations I_{block} upon translocation of particles and biomolecules of interest through the pore are measured and amplified by the Axopatch 200B and sent to the digitizer Digidata 1440A. Further signal analysis can be performed using the dedicated software *PClamp 10*. The Faraday cage shields the electrochemical experiment from external electromagnetic noise.

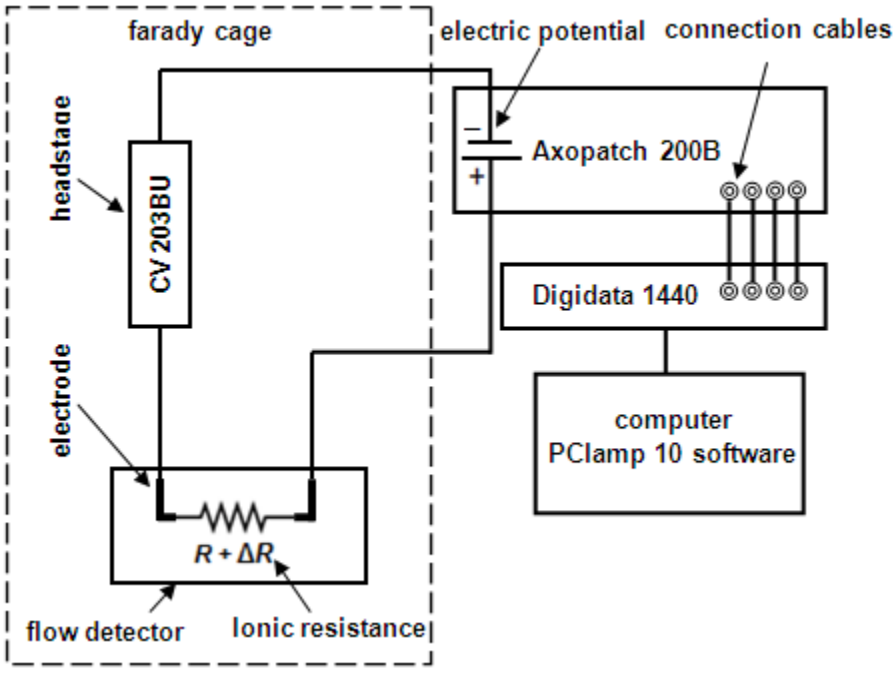

Figure 5.2: Patch clamp setup block diagram

5.2. Characterization of the Pore Geometry

A standard tool in measuring microscopic feature sizes is optical microscopy. Diffraction limits the resolution of optical microscopes to a few hundred nanometers. Many of the pores fabricated can therefore not even be imaged, and none measured with sufficient resolution. Diffraction effects can be neglected in Electron microscopy, and details down to nm or even sub-nm scale can be imaged. Given the relatively thick membrane, transmission electron microscopy cannot be applied for such a small feature size. However, as it was discussed in chapter 4, SEM as non-calibrated and AFM as calibrated methods can be used within limits to measure the pore size before releasing from silicon wafer. However, SEM measurements always led to thermal damage of the membrane surface, and AFM results suffered from convolution effects.

Since the release of the membrane from sacrificial substrate will also have an impact on the exact pore size, it should be remeasured after release. At this stage, even worse thermal effects are expected from SEM inspection since the sacrificial wafer no longer serves as a heat sink, and the AFM tip would likely mechanically compromise the membrane as it is no longer supported from the back side. An alternative to using such standard metrology tools is to evaluate the nano-fluidic performance of the pore. This approach allows to assess the effective pore diameter regardless of whether this is located at the top of the membrane, at its bottom, or in between. This constitutes a further advantage over standard tools which are often limited to measuring surface topographies. The pore diameter was derived in chapter 2, under the assumption of a cylindrical pore, as

$$D = \sqrt{\frac{4LI}{\pi KU}} \tag{5.1}$$

where D is the pore diameter, L denotes the length of the pore, corresponding to the membrane thickness, U is the voltage applied across the membrane, I is the current through the pore, and K is the specific conductivity of the KCL solution. This equation allows to do electrochemical measurements with the pore to approximate its size and to reliably compare pore sizes with a constant measurement setup.

Based on equation 5.1, the 300 nm pores previously inspected by SEM and AFM delivered a diameter of 450 nm. The observed mismatch might indicate a change of the diameter between the previous measurements performed on a sacrificial substrate and the current measurement performed after release. In particular, the UV exposure and thermal cycling could have

contributed to such a change. Furthermore, the electrochemical measurements might slightly overestimate the diameter based on the applicability of the underlying model assumption of a cylindrical pore shape.

5.3. Analysis of the Open Pore Current

After determining the exact pore size, the nanofluidic detector functionality is now verified by analyzing the open pore current I_{open}. These tests will be used to evaluate whether the detector system is hermetically sealed and the only connection between the electrolyte reservoirs actually is the nanopore. This would be a requirement for any application as a pore-based detector. Tests also include an electrochemical characterization of the detector, analyzing the followings:

- Noise levels of unpatterned membranes;
- Long-term stability and noise levels of the open pore current I_{open};
- Current-voltage (I-V) characteristics;
- Impact of electrolyte concentration on I_{open} and the cross-pore conductance;
- Impact of electrolyte concentration on resistance of the pores.

In all experiments, both electrolyte reservoirs are filled with KCl electrolyte solution of 0.1 M concentration, unless otherwise stated. An unbuffered KCl solution with a slightly acidic pH value of 6.0 ± 0.2 is used in all experiments to avoid introduction of variations, which might otherwise potentially lead to additional ionic effects in the system.

5.3.1. Noise Level of unpatterned Membranes

Selected tests were carried out with a complete flow detector system, however using an unpatterned membrane, i.e. a membrane without a pore. This test was made for few times over a

period of a day. A reliable detector would therefore deliver an "open pore current" of zero, independent of properties such as the electrolyte concentration or the acceleration voltage. These tests, if successful, will validate the hermetic assembly concept, the dielectric properties of the membrane, and the system noise level in the absence of fluidic effects.

The measured open pore current actually was zero for all devices and under all conditions tested. This proves a hermetic seal of the devices. Typical noise levels are between 4 pA and 5 pA at 2 kHz bandwidth. This noise does not include contributions from fluidic effects and is referred to as system noise. It arises from the electrodes, the electronic instrumentation (e.g., voltage clamp amplifier), external sources (e.g., power lines, fluorescent lights, monitors, and even noise associated with mechanical vibrations), and the digitizer. The faraday cage mentioned in chapter 5.1 shields the electrophoretic setup. The Axopatch system is equipped with an 8-pole Bessel low pass filter with a -3 dB selectable bandwidth of 1 kHz to 100 kHz, and built-in amplifiers are optimized for low noise in the DC to 10 kHz bandwidth. According to the manufacturers' users guide [7], the lowest noise level that can be achieved is less than 1 pA. This is about 20% of the noise we determined for the entire system in the laboratory environment.

5.3.2. Long-Term Stability, Noise Level and Repeatability of the Open Pore Current

In subsequent tests, 450 nm pores are characterized electrochemically. Figure 5.3 exemplifies sample recordings of the open pore current I_{open} in 20 mV increments of the applied voltage (20 mV to 100 mV) over a time period of 10 minutes. The ionic transport at 20 mV applied external voltage is magnified in the left inset to better demonstrate the presence of a steady-state I_{open} of 4 nA and the corresponding noise of 25-30 pA. at 100 mV, I_{open} increases to 20 nA with a 10 kHz noise of 35-40 pA (see right on the right).

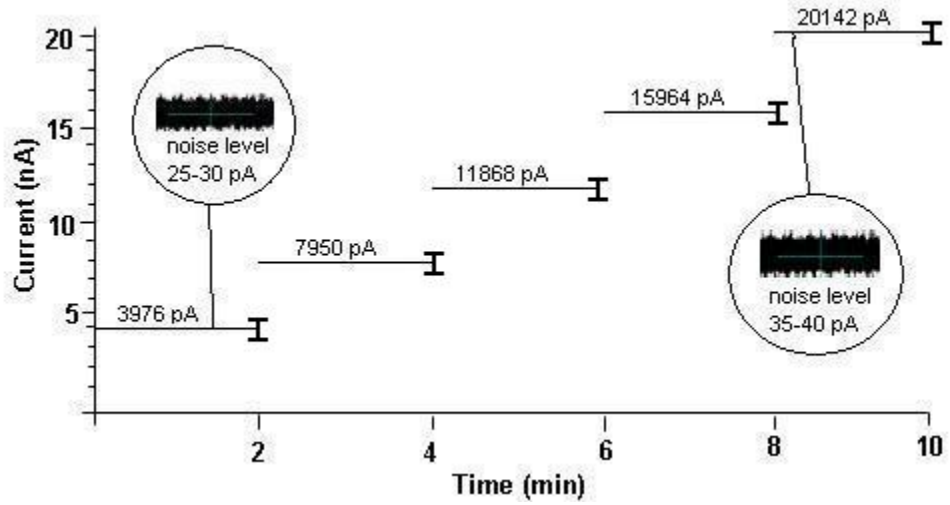

Figure 5.3: Patch clamp measurements of the open-pore current (I_{open}, nA) through single cylindrical submicron pores (300 nm diameter) in PMMA membrane as a function of time (min), in the presence of 0.1 M KCl electrolyte solution and applied external voltages of 20 mV to 100 mV, in 20 mV increments. The magnified insets demonstrate a steady-state I_{open} over time at 20 mV applied voltage having a low level of noise (approx. 1% of I_{open}). The measured signal is reproducible within ±10-15% shown with error bar.

The observed noise is less than 1% of I_{open} for all voltage levels analyzed. However, it is still significantly more than the system noise of 4-5 pA introduced in the previous chapter. Additional sources of noise related to fluidics depend on parameters affecting the fluidics and surface charge properties. Such parameters include the electrolyte concentration, the pH value, the electroosmotic flow, and the driving voltage. The detected noise also depends on the filters applied in the measurements. A filter with appropriate band width reduces noise to a level deemed acceptable so that the desired signal can be detected. A wider filter band width can be chosen if the signal is large enough compared to the background noise, so that more rapid events

can pass through the filter. In our experiments, we used a filter band width of 10 kHz, which is commonly used in patch clamp experiments.

The measured signal is reproducible within ±10-15%, when the pores gets evacuated, washed with de-ionized water, and re-examined following the same procedure after a finite period of time. This value therefore not only comprises the variations between several measurements, but also includes ‘reusing’ a pore that was cleaned in between uses. These variations are identified as the error bars in Figure 5.3.

The ionic current measured appears to be independent of the exact distance between each electrode and the membrane, as long as both electrodes are approximately placed in the same distance from the membrane, which is guaranteed by the system layout. Measurements are started 0.5 to 1 hour after filling the electrolyte solution to allow for the pore to reach its steady-state I_{open} level. This setting time is usually attributed to the dynamics associated with wetting of the pore and also removal of contaminant layers; contaminants from previous measurements, as well as contaminants in the electrolyte solution, would certainly add to the overall noise level. Both should therefore be minimized, and the setting time addresses at least the first point. In the present research, the setting time is significantly reduced by immersion of the pores into de-ionized water for storage immediately after each experiment. This is shown to avoid drying of the pores as well as accumulation of solidifying contaminants in the vicinity of the pores.

The detector devices are tested over a period of three months (some even up to a year) to show their long-term and multi-experiment stability.

The low level of noise would, of course, likely increase with a significant decrease in the pore size because of an increase in the relative tolerance and roughness and an increase in the effect of contaminants and their relative importance. Furthermore, Siwy et al. [40] demonstrated that the

ion transport properties of artificial micro/nanopores are strongly influenced by the chemical structure of the membranes as well as microfabrication steps involved, including beam exposure and other accompanying pore development procedures. For instance, the typical behaviour of the ion current versus time recorded at a constant voltage in the case of PET membrane exhibited pronounced fluctuations with a high level of noise. Likewise, the nanopores in PC foils present similar transport characteristics. In contrast, there were no fluctuations observed for pores microfabricated in PI by the same procedure of ion track etching [40, 68]. The authors explained this difference with different material structures/properties related to imperfectly terminated polymer chains. Upon ion exposure-induced scission of polymer chains and subsequent chemical etching, carboxylate end groups are formed in PET. In PET, the so called "dangling ends" are created due to the presence of ethylene components, which perform random movements and thus fluctuations, when immersed in a solution. The chemical structure of PI, on the other hand, is based on a planar sequence of aromatic groups, rendering a strong rigidity to the material and limiting the movement of PI polymer chains and thus fluctuations when immersed. Smoothness and rigidity of the PI surface thus seem to be the factors responsible for the observed stable ionic current.

In agreement to above, we propose that the observed low level of noise with our PMMA membrane-based detector devices can be mainly attributed to the experimental conditions that are employed by our group in comparison to other research groups. This is because of the fact that electron beams are also previously shown to create carboxylate end groups (dangling ends) with a net negative charge on the surface of PMMA membrane [69]. However, we, in our experiments, could control their formation and, thus the resulting negative membrane surface charge, keeping them in their minimal amount using KCl electrolyte solution of a slightly acidic

pH value; at neutral and basic pH values, the generated dangling carboxylate end groups by the microfabrication/micro-patterning procedure are deprotonated, yielding in an excess negative charge attached to the relatively flexible polymeric chains on the membrane surface. Under these circumstances, when a micro/nanopore is immersed in an electrolyte solution, increasing the voltage and, thus enhancing the electric field, will cause the negatively charged flexible dangling end carboxylate groups to move vigorously in the field direction resulting in an increased level of noise. In comparison, at a slightly acidic pH value of the electrolyte solution (6.0 ± 0.2) used in our experiments, however, the carboxylate end groups are mostly kept in their protonated state, giving rise to a minimal net negative surface charge on the membrane and, thus minimal random movements/fluctuations under an applied external voltage. Our explanation is in accordance to those of other researchers; Siwy et al. [40] suggested that reducing the electrolyte pH value below 3 would neutralize carboxyl groups present on PMMA membrane surface lowering the negative surface charge density of the membrane. However, this could destabilize our analyte molecules to be detected in our next experiments and is hence not a feasible option.

In any case, the preceding arguments all stress the importance of fine-tuning the surface chemistry of membranes in the operation of micro/nanopore systems and their associated noise level. Other than the described reversible changes (reduction of net negative surface charge) in membrane surface chemistry caused by manipulation of the pH of electrolyte solution, in which the pore-containing membranes are immersed, another approach could be through chemical surface modification procedures, which can be implemented relatively easy on polymer membranes: a huge advantage for our selected membrane material of PMMA. Whilst there are a number of existing physical and chemical methods, in the area of surface modification of polymeric synthetic membranes most emphasis has been given to plasma treatment, grafting of

polymers on the surface, and modifying the surfaces by adding surface modifying molecules [38, 70].

Summing up the measured results of this chapter, the pores exhibit a stable, time-independent open pore current with a low level of noise over a wide range of applied voltages from 0 mV (control scenario) to 100 mV. This proves that the PMMA membrane neither deteriorates by excessive swelling nor starts to leak over time.

5.3.3. Current-Voltage Characteristics

As anticipated from above results, evaluation of the open-pore current-voltage (I-V) characteristics demonstrates a strong linear relationship at five different KCl electrolyte solution concentrations of 0.02, 0.05, 0.1, 0.5, and 0.75 M (Figure 5.4). No saturation is observed for higher driving voltages, such that a wide range of voltages from 0 mV to + 100 mV typically used in such electrophoretic experiments can be applied. Even further increasing the transmembrane potential to voltages beyond + 100 mV does not damage the PMMA membrane, and further increases the current through the submicron pore to higher values. This is in contrast to protein nanopores, such as α-hemolysin, where a transmembrane potential of + 100 mV produces a current value of approximately 100 pA, but a higher potential will result in damage to the lipid bilayer membrane [18].

The observed I-V characteristics in Figure 5.4 are linear and do not show any current at an applied driving voltage of zero. This relates to the transport mechanisms effective in our devices (no diffusive contribution), and determines that it is possible for our devices to operate under reverse polarity. Three different transport mechanisms can contribute to the measured total steady-state ionic transport through a specific pore: convection i.e., electro-osmotic flow (EOF), driven by the pre-formed electric double-layer on the pore surface and walls (explained in

section 5.3.4), and partly by the electric field applied across a pore] (Ho et al., 2005), electrophoretic ion migration (driven by the electric field applied), and diffusion (driven by the electrolyte concentration gradient). Diffusion is the only contribution independent of the applied voltage. The devices exhibit zero current at zero voltage, indicating negligible diffusive transport contributions. Therefore, as expected, the electrolyte solution does not exhibit a concentration gradient across the pore for either of the tested molarities.

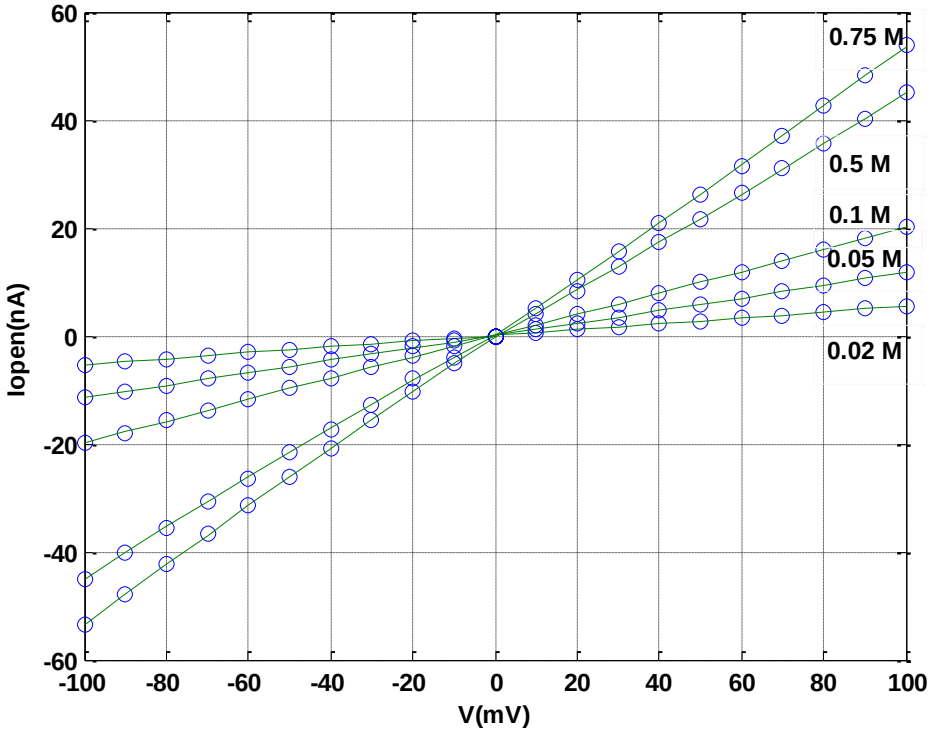

Figure 5.4: Patch clamp measurements of I_{open} (I_o, nA) as a function of the applied voltage (mV) for five different KCl electrolyte concentrations of 0.02, 0.05, 0.1, 0.5, and 0.75 M.

As shown in Figure 5.4, the same linear I-V relationship is maintained when negative transmembrane potentials of 0 mV to -100 mV are applied. More accurately, the amount of

current measured through the pore at a certain negative transmembrane potential is approximately the same as that measured at a corresponding positive potential. These pores, therefore, do not exhibit rectification of the current flowing through them. Similar I-V relationships have been reported by other groups working with cylindrical nanopores [71, 72, 34]. This observation has two implications: First, the device can be operated in either direction (or polarity), which is referred to as dual "on"-state (see below for explanation). Second, this is a further confirmation of the symmetrical shape of our pores: asymmetric (e.g. conical) pores such as basically all protein pores and conically-shaped artificial synthetic pores typically exhibit current rectification. This can be explained by a model focusing on electrostatic interactions between ions passing through a specific pore and the surface charge distribution on the pore surface and walls [50]. Almost all microfabrication processes and their accompanying pore development steps leave artificial nanopores in either polymer membranes or silicon-based substrates with a net negative charge on their surface and walls [40]. The surface charge creates an asymmetric internal electrostatic potential inside the pore with a profile dependent on the pore shape. Conical pores accumulate a much higher negative charge, and thus formation of a stronger electrostatic trap, on the pore base compared to the pore tip. This stronger electronic trap, with the applied transmembrane potential induced by the electrodes, creates a preferred transport direction for positively charged ions towards the base [73, 74, 75, 76, 38]. As asymmetric nanopores tend to reduce the ionic flow in one direction, but promote it in the other, they are said to be either in the “on” state with much higher currents flowing through the pores, or in the “off” state with much less currents flowing through the pores. Artificial conical nanopores could, therefore, act like “voltage-gated” channels, resembling some of their biological counterparts. The gated channels open (on state) and close (off state) in response to a specific chemical,

mechanical, or electrical signal. This phenomenon, however, does not occur in symmetric submicron pores with a homogenous surface charge distribution inside the pores, just like for the pores presented in this study. It is often considered an advantage for such pores to be always in their "on" state of function regardless of the polarity of the applied transmembrane potential.

5.3.4. Impact of the Electrolyte Concentration on the Open Pore Current and the Cross-Pore Conductance

The electrical characterization of our detector devices is expanded to the I_{open} as a function of the electrolyte concentration. It is shown in Figure 5.4 that the current monotonously increases with increasing KCl electrolyte concentration (0.02 M to 0.75 M) in an almost linear relationship. Applied voltages range from + 10 mV to + 100 mV.

Standard electrolyte concentrations for biological experiments range from approximately 0.75 down to 0.1 M. Higher electrolyte concentrations are avoided in their experiments because of biological pore are being saturated. They are usually shown to saturate, reaching a conductance plateau, when the concentration is raised above a certain physiological level. This has been attributed to a limited binding-unbinding capacity for protein nanopores. In comparison, artificial synthetic micro/nanopores in solid-state membranes do not exhibit such a saturated conductance pattern, allowing their application in a broader concentration range. We also identified that the dependence of the ionic current through single artificial submicron pores on the electrolyte concentration deviates to a curve with a steeper slope, at all the voltages applied, as the electrolyte concentration is lowered to values below 0.1 M. We therefore extended the electrolyte concentration range in our tests beyond 0.1 M and included 0.02 and 0.05 to study the flow behavior in this critical region as well. The results obtained are in agreement with Schiedt et al. [50] (Figure 5.5). The observed phenomenon has been attributed to two effects: an incomplete

dissociation of the electrolyte at higher concentrations, and formation of an "electric double-layer". An electric double-layer is formed as the negative surface charge on the PMMA membrane, due to the formation of carboxylate end groups, attracts K^+ ions in the electrolyte solution to the pore surface and walls [50, 41]. The electric double layer, then increase the effective potential for the electrochemical transport mechanism through the pores. The thickness of the formed double-layer depends on the salt concentration of the electrolyte solution in the vicinity of the membrane; at lower salt concentrations, the relative concentration of K^+ ions on the pore surface and walls is much greater compared to that in the bulk electrolyte solution, determining a thicker double-layer, and therefore an elevated conductivity gradient or higher conductance.

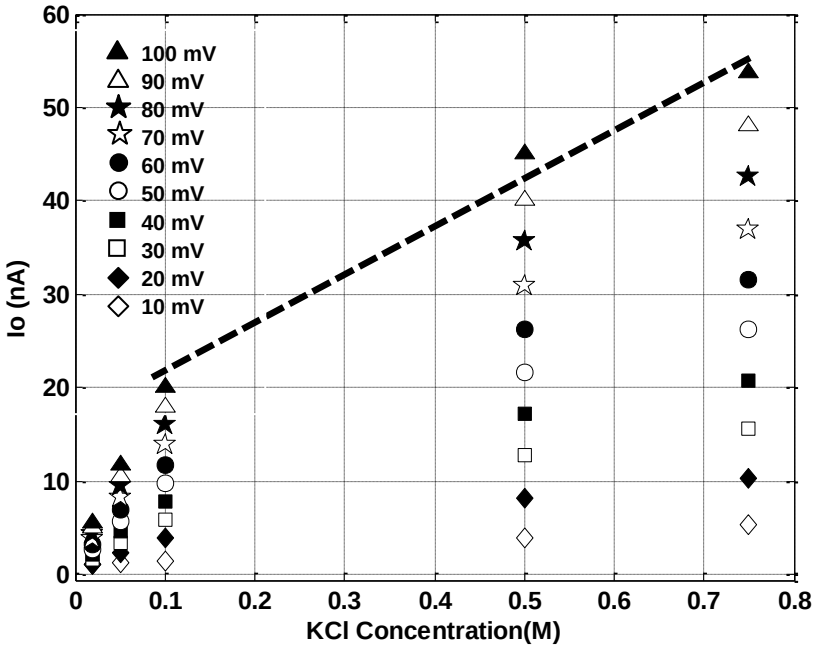

Figure 5.5: Patch clamp measurements of I_{open} as a function of the KCl electrolyte concentration for the applied voltages ranging from 10 mV to 100 mV.

The same effect is illustrated in Figure 5.6 by showing the conductance [reciprocal of the steady-state pore resistance ($1/R_p$), ns, demonstrated below] measured as a function of the electrolyte concentration. In accordance to the data presented above, the pore conductance also over-proportionally increases with increasing electrolyte concentration at low concentrations. Our results are in close agreement with those reported by other researchers fabricating cylindrical and conical nanopores in membranes with unique surface charges [34, 50].

As a remedy to this effect, the negative surface charge on the membrane can be minimized or even neutralized by temporary protonation of the membrane surface, which offers additional positive charge carriers, or by modification of the surface properties themselves permanently or for intermediate terms. Temporary protonation can be achieved by adjusting the pH value of the electrolyte solution to an acidic regime [40]. We, ourselves, observed a pH value of approximately three to almost neutralize the aforementioned effects. However, whether such an approach is compatible with future biological experiments might need further clarification. Modification of the surface properties of the membrane can be achieved for longer times by either inducing chemical reactions based on oxygen plasma treatment or by photochemical modifications involving UV surface exposure [38, 77].

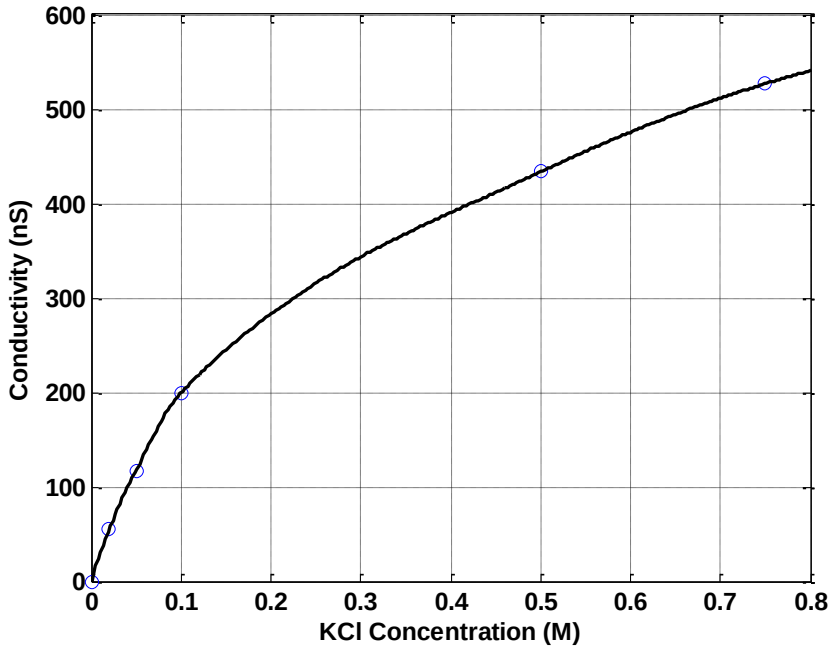

Figure 5.6: Patch clamp measurements of the conductance (ns) through single cylindrical submicron pores as a function of KCl concentrations of 0.02, 0.05, 0.1, 0.5, and 0.75 M.

5.3.5. Impact of the Electrolyte Concentration on the Pore Resistance

The resistance of single synthetic cylindrical submicron pores in PMMA membrane as a function of increasing KCl electrolyte concentration is elucidated in Figure 5.7. The measured resistances are inversely correlated to the slope of the described I-V curve (Figure 5.4). According to Figures 5.4 and 5.7, as KCl concentration decreases, the magnitude of the slope of the I-V curve increases, resulting in a larger pore resistance. In agreement to the above mentioned, larger pore resistance would be exactly expected as lower salt concentrations result in a thicker double-layer on the pore wall and surface. Very close similarity exists between our

present data and the ones reported by other researchers fabricating cylindrical nanopores in silicon-based membranes [33].

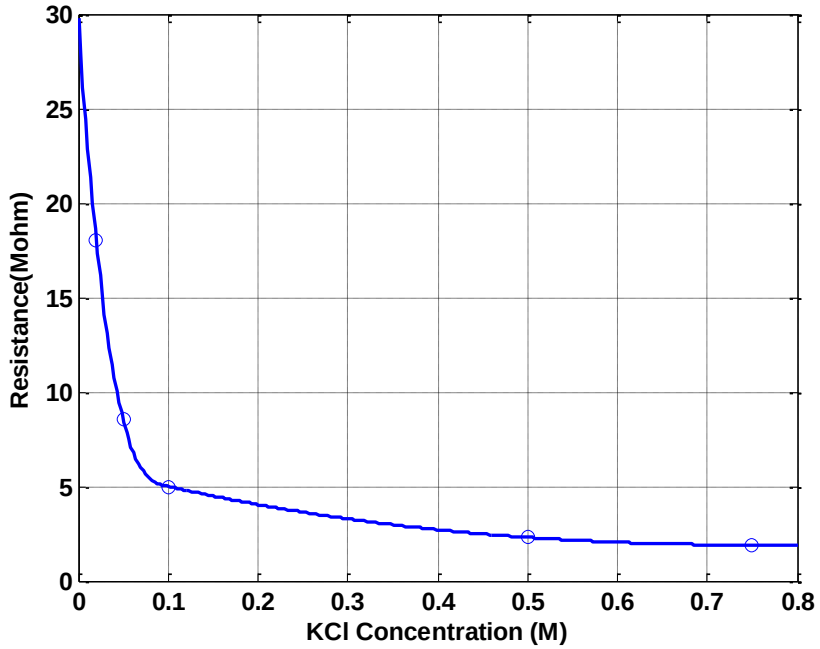

Figure 5.7: Resistance of single submicron pores (R_p, MΩ) as a function of increasing KCl concentrations of 0.1, 0.5, and 0.75 M.

5.4. Functional Analysis of Submicron Pores via Translocation of Differently-Sized Silica Nanoparticles

In section 5.2, the geometrical pore properties were identified. In section 5.3, the nanofluidic detector functionality was verified by analysing the open pore current. A third aspect of pre-testing the flow detector now is calibrating it by measuring the current blockage caused by nano particles of known size. Test objects are silica nanospheres of 100 nm and 150 nm nominal

diameters purchased from Polysciences, Inc. These are tested in pores with a nominal diameter of 300 nm and an actual diameter of about of about 450 nm.

In preparation of the test are the electrolyte reservoirs of filled with electrolyte solution of 0.1 M concentration, using unbuffered KCl with a slightly acidic pH value of 6.0 ± 0.2. The test nanoparticles are then added to the reservoir on the negative side of the membrane (*cis* compartment). The final concentration is 3.10^9 spheres/ml. An external potential between 10 mV and 30 mV is applied across the membrane to induce a transmembrane ionic current.

5.4.1. Mathematical Model for the Current Blockade

Prior to actual measurements, translocations of silica nanoparticles through a 450 nm pore are mathematically modeled to obtain reference values for later experimental verification. The temporary current blockade I_{block} associated with such an event is calculated based on an increase in resistance, ΔR, due to the presence of nanoparticle/s inside the pore. Different models have been proposed in literature to estimate the resistance variance developed by a single particle translocating through a pore [34, 52]. All of these models have been proven valid only for certain and very specific pore shapes and dimensions. Deblois and Bean [52] were the first to develop a theory for translocating spheres in a uniform electric field that is valid over a broad range of pore shapes and dimensions. Deblois model was described in detail in chapter 2. Simplifying the model for a cylindrical pore of diameter D, a translocating sphere diameter of $d \ll D$, ΔR can be written as

$$\Delta R = \frac{4\rho' d^3}{\pi D_m^4}\left(1 + 1.26\frac{d^3}{D_m^3} + 1.1\frac{d^6}{D_m^6}\right) \tag{5.2}$$

where ρ is the electrolyte resistivity and L is the length of the pore over which the potential difference is applied. This expression includes the Maxwellian value as its limit. The increased resistance obtained is independent of the pore length L if L is much bigger than D_m [52]. This applies to the geometry under discussion with $L = 1000\ nm$ and $D_m = 450\ nm$. This means that the obtained ΔR values in this situation can be quite the local values across the pore and is only affected by the existing of nanoparticle inside the pore.

Deblois's group evaluated their proposed model by calculating ΔR values for three different pore sizes of 400 nm, 454 nm, and 500 nm diameter, and translocating sphere particles of up to 400 nm in diameter. They considered an electrolyte resistivity of $\rho = 0.75\ \Omega m$. Among all of their analysis, it is demonstrated that the ΔR values calculated for a 454 nm-diameter pore were in very close agreement with the experimentally obtained values for translocating sphere particles of less than 200 nm in diameter. From above model, it is concluded, in a simplified form, when the sphere particles get closer in diameter to that of the pore, the experimental results of ΔR fall below the theoretical values. This ΔR value, is then used to determine the magnitudes of the I_{block} (which represents as ΔI) spikes according to

$$\Delta I = I_{open} \frac{\Delta R}{R_{open} + \Delta R} \tag{5.3}$$

The particle size obviously has the strongest impact on the current blockade. Increasing particle diameters will increase the expected blockade in a cubic fashion. Assuming a constant driving voltage of 20 mV, 100 nm silica nanoparticles translocation through 450 nm pore result in current blockade of $I_{block} = 32\ pA$, which is only twice the noise level, whereas larger particles of 150 nm diameter cause a much increased blockade of $I_{block} = 112\ pA$.

5.4.2. Measured Current Blockade of 100 nm Silica Nanoparticles

Measurements of the ionic current through a single 450 nm wide pore are performed both in the absence and presence of 100 nm silica nanospheres. When only pure electrolyte solution without adding nanoparticles is present, an applied constant voltage of 20 mV induces an open pore current I_{open} of approximately 3970 pA. The signal has a very low noise level of approximately 25 pA, and does not fluctuate over time. A typical measurement is reproduced in Figure 5.8 A.

In the next step, 100 nm-silica nanoparticles are added to the electrolyte. Triton X-100 surfactant (0.1% w/v) is also added supporting the translocation of nanoparticles in two ways: It reduces the surface tension in the electrolyte which promotes the wetting properties of the pore and results in an improved flow through the pore. Secondly, the probability of adsorption of nanoparticles to each other, onto the PMMA membrane surface and surfaces of the electrophoretic flow detector is reduced. During extensive measurements, tens of thousands of translocation events are recorded. Figure 5.8 B shows a typical current trace recorded in the presence of 100 nm silica nanospheres. In contrast to Figure 5.8 A, temporary current blockades well beyond the noise level are now observed. These are not present in the absence of nanospeheres and can therefore be associated with individual translocation events of nanospheres. The blockade amplitudes allow to not only detect individual translocation events, but to also discriminate between two distinct blockade regimes: A smaller group of events exhibit I_{block} values of approximately 30 to 35 pA, while a larger group of events demonstrates current deductions of about 50 to 55 pA.

The first group with I_{block} values of 30 to 35 pA is consistent with the prediction of the mathematical model and is therefore associated with a current signature indicative of a complete

translocation of 100 nm silica nanoparticle (labelled as 'type I' in Figure 5.8 C). On average, a complete translocation event takes a blockade time of about 0.5 ms. Type II current signatures in Figure 5.8 C with blockade values of 55 to 65 pA can likely be attributed to the passage of multiple (most probably two) nanoparticles at the same time. This is likely not an independent movement of two individual particles, but due to aggregation of multiple nanoparticles. Some agglomeration can still occur despite the treatment with a surfactant as described above. Type II current signatures in Figure 5.8 C demonstrate a multi-blockade fine structure labelled with subscripts a, b, and c. This labelling refers to earlier studies by Prabhu et al. [78]. Consistent with literature, IIa and IIc events could represent the presence of nanoparticles at the entrance of single pores near their top surface and at the exit of single pores near their bottom surface, respectively. These blockades therefore do not represent successful translocations but are as unavoidable part of high interaction effects in between multiple particles and pore. IIb events represent the presence of nanoparticles actually passing through the centre of a pore, blocking a major portion of the baseline open pore current of I_{open}. On average, a complete translocation event through single pores for multiple (probably two) nanoparticles takes a blockade time of about 1.5 ms. Under the same applied voltage of 20 mV, the difference in blockade times of 1.5 ms versus 0.5 ms observed with current signatures of translocation events II and I could be explained by a higher degree of electrostatic interactions that may occur between translocating nanoparticles and the fixed surface charges on the membrane, when multiple nanoparticles are passing together, at the same time, through single pores.

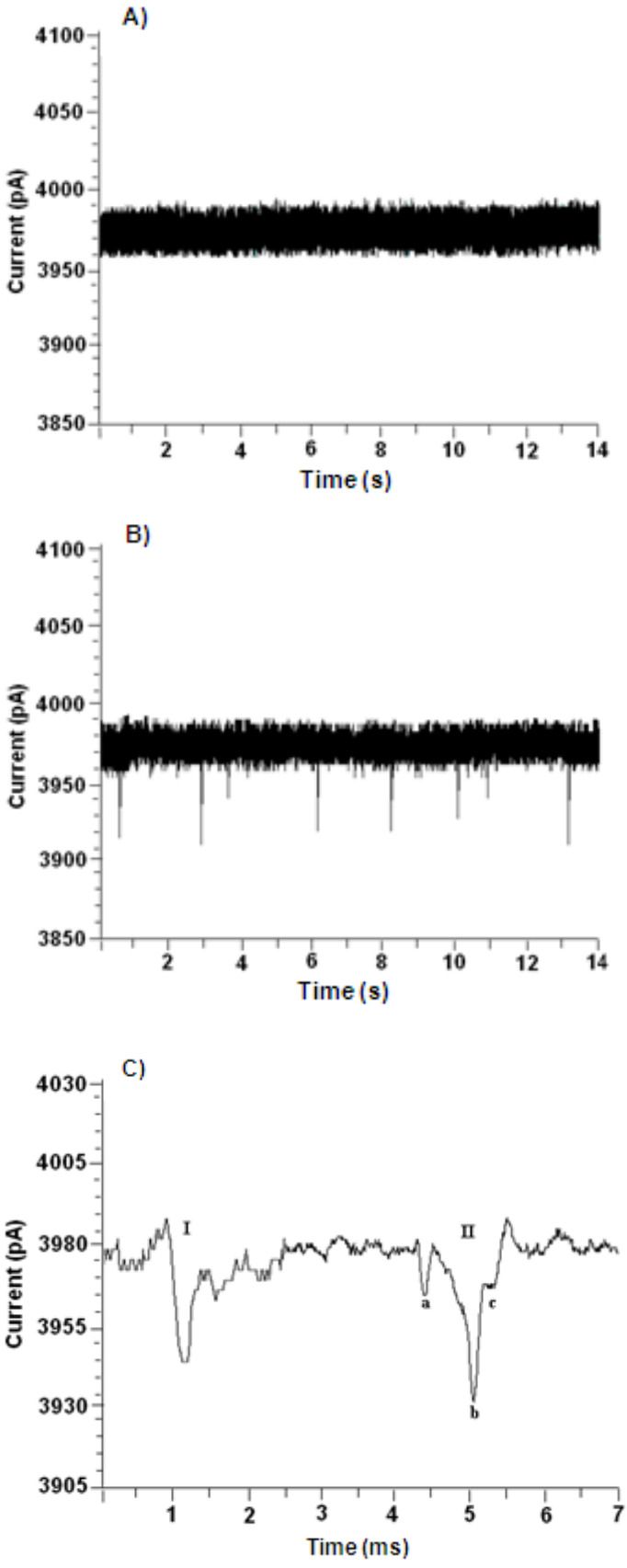
A)
4100
4050
4000
3950
3900
3850
Current (pA)
2
4
6
8
10
12
14
Time (s)
B)
4100
4050
4000
3950
3900
3850
Current (pA)
2
4
6
8
10
12
14
Time (s)
C)
4030
4005
3980
3955
3930
3905
Current (pA)
I
II
a
b
c
1
2
3
4
5
6
7
Time (ms)

Figure 5.8: Open pore current I_{open} through a 450 nm wide nanopore in a 1 µm thick PMMA membrane and current blockades I_{block} caused by translocation events of 100 nm silica nanospheres. Measurements obtained at room temperature, 20 mV driving voltage, and 0.1 M electrolyte concentration: (A) Basal ionic current I_{open} versus time in the absence of silica nanoparticles as a reference; (B) Ionic current with temporary current blockades of 30 to 55 pA in the presence of nanoparticles; (C) Close-up of a segment of B with 2,000-fold time resolution, showing only two individual blockade events representing two types of translocation events - type I with current blockades of about 30 to 35 pA, type II with current blockades of about 50 to 55 pA.

Translocations are measured for various driving voltages, beyond the 20 mV described above. Figure 5.9 represents excerpts from line traces taken from the each individual experiment at 10 mV, 20 mV, and 30 mV (left to right). Two effects can be identified regarding frequency and amplitude: Translocation events occur more frequently upon increased voltage at otherwise constant conditions. At 10 mV, on average, a translocation occurs every 1.5 seconds, at 20 mV every 1 second, and at 30 mV every 0.5 seconds. Besides, the amplitude of the current blockade increases, from typically 15±5 pA at 10 mV to 30±5 pA at 20 mV to finally 40±5 pA at 30 mV.

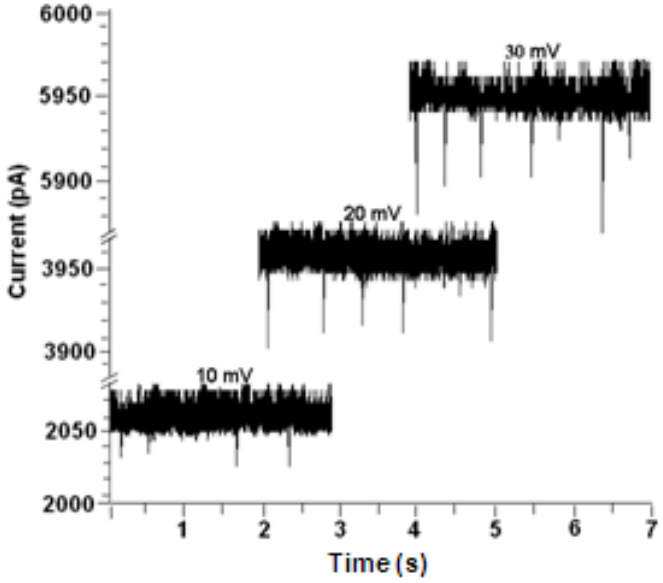

Figure 5.9: Measured current signal with open pore current and current blockade events during the translocation of 100 nm silica nanospheres through a 450 nm pore in PMMA for various driving voltages (10 mV, 20 mV, and 30 mV).

This increase in frequency and amplitude can be explained based on a force equilibrium acting on the nanoparticles: The driving force for a nanoparticle to translocate through a micro/nanopore is determined by balancing the electrostatic force and the viscous drag force. The electrostatic force arises from the electrophoretic pull on the charged nanoparticle in an electric field, while the viscous drag force arises from fluid flow due to the nanoparticle motion as well as the electro-osmotic flow (EOF) present around the charged nanoparticle and the membrane surface. All of these forces are ultimately dependent on the net- or surface charge of the nanoparticle observed and the porous membrane. Prabhu et al. [78] derived drag forces created by the EOF under various circumstances. For negatively-charged nanoparticles and a relatively negatively-charged membrane, the EOF around nanoparticles and the membrane

surface creates a drag force that opposes the electrophoretic pull experienced by nanoparticles. Nanoparticle translocation in this case requires the electrophoretic force to overcome the drag force created by the EOF. With increasing driving voltage, the electrophoretic force outgrows the EOF-related drag force and speeds up the translocation of nanoparticles through the pore, and ultimately results in a higher frequency of translocations. Increasing the voltage also increases the open pore current I_{open} as previously explained in the context of the I-V characteristics in section 5.3.3. This effect is evident in Figure 5.9 as well, where I_{open} rises from about 2065 pA at 10 mV to 3960 pA at 20 mV and 5950 pA at 30 mV. An increased I_{open} through single pores with increasing voltage creates higher interaction in between forces involved in translocation and also larger number of particles (single or multiple) passing through the pore. It produces a higher resistance against and more volume occupied by the passing particles through the pore per unit of time. This then results in increased amplitudes of I_{block} spikes observed in our experimental results.

We did not increase the voltage beyond 30 mV in our experiments with nanoparticles due to creation of a higher level of noise, than the one reported in section 5.3.2, as the voltage is increased. A higher level of noise could hide some of the translocation events happening through the single pores with small I_{block} values.

Under a fixed pH value of electrolyte solution (6.0 ± 0.2) being used in our experiments, there would be a minimum possibility for formation of further negatively-charged dangling carboxylate end groups on the surface of our PMMA membranes, that are able to move and fluctuate around upon increasing the voltage, creating a higher noise level. We, therefore, could interpret the higher level of noise seen in our nanoparticle experiments with increasing the voltage, to the bombardment of the membrane surface by a higher number of nanoparticles

intending to translocate through single pores. With increasing driving voltage, resulting in a higher open pore current, the frequency of translocations does increase as well, as explained above. Besides, the probability and therefore the frequency of unsuccessful translocations, referred to as *bumping* or *collision*, also increases. Examples of these are type IIa events highlighted in Figure 5.8 C. Mara et al. [68] described that any time a nanoparticle is pulled toward a specific pore, but the interaction is not within a certain distance of the membrane surface, it will only strike the membrane surface but not translocate through the pore, creating such *bumping/collision* events. A high number of bumping/collision events bombarding single pore's membrane surfaces would also give rise to an increased level of noise and inhibit translocation events to happen.

5.4.3. Measured Current Blockade of 150 nm Silica Nanoparticles

After reproducible measurements of 100 nm silica nanospheres and the analysis of the current traces, the next step is to validate that the flow detector is fundamentally capable of discriminating between different nanoparticles based on their size and/or conformation. This is done in the next test by introducing slightly larger silica nanospheres with 150 nm diameter instead of the 100 nm studied before. We flushed the detector system and reused it for the next set of tests under otherwise same conditions. At 20 mV driving voltage, a stable open pore current is observed. While the recorded open pore current is the same as encountered in previous experiments with 100 nm nanospheres, the amplitude of the current blockade now is much higher. Figure 5.10 represents a sample current trace, which shows, as before, two well-defined types of translocation events. Some current blockades exhibit approximately 105 to 110 pA reduction of the open pore current. This measurement is in excellent agreement with the mathematical model which predicted a current blockade of $I_{block} = 112\ pA$. This set of events

therefore likely corresponds to the successful and complete translocations of nanospheres. Other translocation events, however, exhibit higher amounts of current blockades with I_{block} values of around 200 pA. These events are, again, associated with agglomerated multiple nanospheres translocating through the pore at the same time.

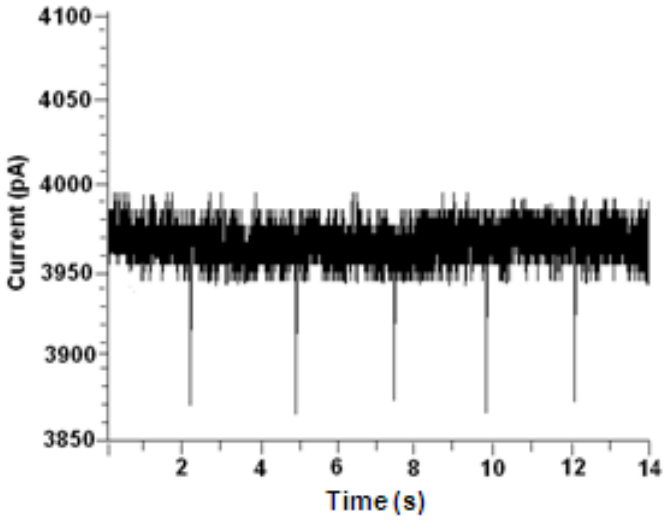

Figure 5.10: Measured current signal with open pore current and current blockade events during the translocation of 150 nm silica nanospheres through a 450 nm pore in PMMA at a driving voltage of 20 mV.

5.4.4. Comparison of modeled and measured Current Blockade

The functional analysis of the detector using translocating test nanoparticles is concluded by evaluating all the modeled and measured data in comparison. 100 nm and 150 nm spheres are considered at driving voltages between 10 mV and 30 mV. The functional value analysed is the current blockade I_{block} obtained under the various conditions. The mathematical model for 100 nm nanospheres predicts current blockades of, e.g., 16 pA, 32 pA, and 48 pA at an applied voltage of 10 mV, 20 mV, and 30 mV, respectively. For 150 nm nanospheres, these values

increase to 56 pA, 112 pA, and 168 pA. The mathematical model predicts the linear increase with voltage in either case. Figure 5.11 graphically represents these modeled values as the two solid lines.

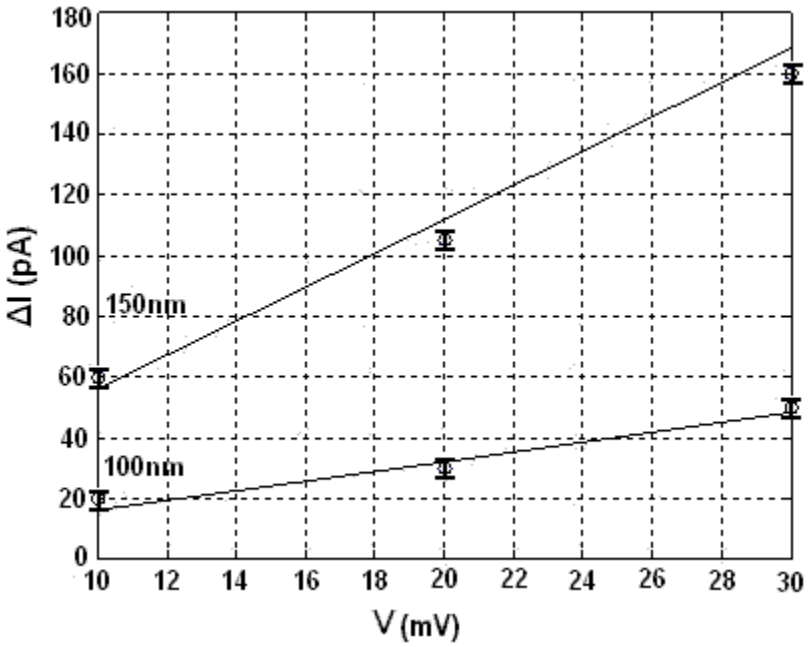

Figure 5.11: Current blockade I_{block} in a 450 nm wide submicron pore as a function of the driving potential V for 100 nm (bottom) and 150 nm (top) silica nanospheres. Mathematical model (straight lines) and measurements at 10 mV, 20 mV, and 30 mV driving voltage (open circles). Average amount of experimental results obtain a tolerances of ± 2.5 pA shown with error bar.

The circled data points in Figure 5.11 represent measured values obtained for experimental verification. The data points presented refer to complete translocation of individual nanospheres only, i.e. unsuccessful translocation (bumping/collision) as well as translocation of multi-particle-agglomerates have been disregarded in this analysis. The measured values are in very

good agreement with the modeled values. Maximum deviations are 5-7 pA with voltage sweeps from 10 mV to 30 mV, in 10 mV increments, for single 100 nm- and 150 nm-nanoparticles are performed as depicted in Figure 5.11. The experimentally-measured I_{block} values are in good agreement with the obtained mathematically-calculated ones. As expected, translocation events and, thus reductions in the amount of basal I_{open} through single pores, are not observed for experiments at 0 mV driving voltage. As explained earlier in section 5.3.3, for well-behaved linear systems, this is due to the fact that under the conditions, where no potential difference is applied across single pores, there would not be any electrophoretic force available to electrophoretically drive single molecules through the pores that exhibit a negligible amount of diffusive transport in the absence of a concentration gradient across them.

5.5. Functional Analysis of Self-Assembled Protein Pores via Translocation of Linear ssDNA Molecules

The nanopores that were patterned by electron beam lithography have diameters down to a few hundred nanometers or down to a few ten nanometers after thermal treatment. Pores yet one order of magnitude smaller were rapidly prototyped in a bottom-up approach using self-assembly of biological nanpores: 1.5 nm wide α-hemolysin protein nanopores were inserted directly into lipid bilayer membranes previously attached across micropores in a PMMA membrane. The fabrication sequence developed was explained in detail in chapter 4.4. The detector systems based on these self-assembled pores are now functionally tested for applications in biomedical sensing. The α-hemolysin protein features a nanopore with a fixed diameter of 1.5 nm. This is only slightly bigger than single stranded (ss) DNA molecules which are important biomolecules storing all genotypic and phenotypic characteristics of living things. Detection of ssDNA would

therefore be a valuable proof of the detector functionality. We prepared samples of ssDNA from DNA purchased from Invitrogen^{TM}/Life Technologies.

Functional testing included determination of the open pore current in the absence of ssDNA, and the current blockade in the presence of ssDNA. At 100 mV driving voltage, the open pore current amounts to approximately 800 pA. This is indicative of 8 nanopores present in the membrane, as each nanopore can handle 100 pA at this voltage. Figure 5.12 A represents such an I_{open} current trace up to an hour. When no biomolecules are added to the electrolyte solution, I_{open} remains constant during the tests. Upon addition of linear plasmid ssDNA molecules to the electrolyte solution in the negatively-biased reservoir, numerous short-lived current blockades occur illustrated in Figure 5.12 B. The observed events are identified as translocation of ssDNA molecules through the protein nanopores, as they entirely disappear after the molecules are flushed out of the detector system in about an hour. A single translocation event exhibits a current blockade of about 95 pA, or 11% of the total open pore current through 8 nanopores. If only one biological pore had been introduced into the membrane, each translocating ssDNA would lead to a current blockade of about 90% of the open pore current. This demonstrates a very high sensitivity of the nanopore-based detector, and proves its functionality. Further studies will concentrate on the impact of molecule conformation, as the relative orientation of molecular building blocks is referred to the biological context, on the detected signal. Signal variations with conformation would be very beneficial further biological information retrieved from the detector.

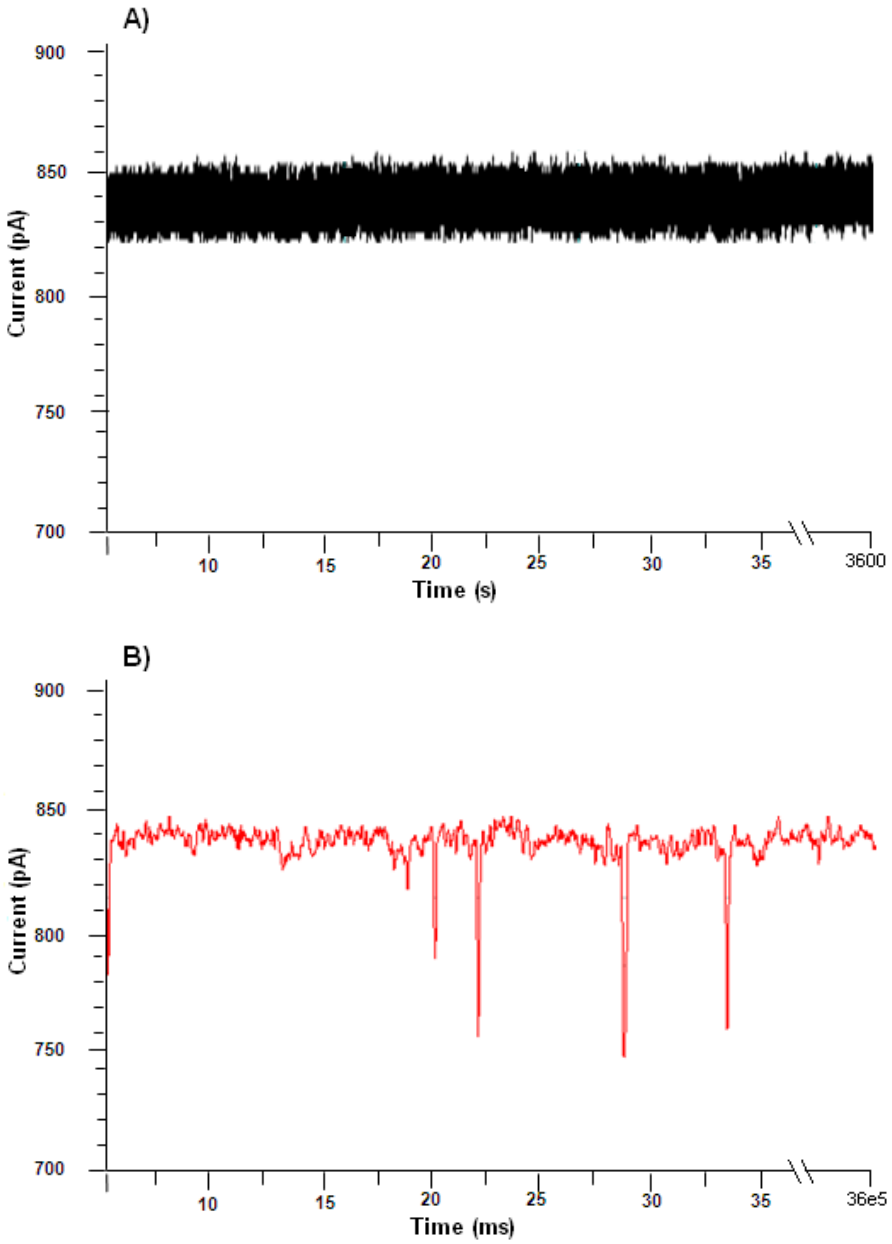

Figure 5.12: Patch clamp measurements with 8 biological nanpores (α-hemolysin) inserted into a lipid bilayer on a PMMA membrane applying 100 mV driving voltage in to 0.1 M KCl electrolyte at room temperature: (A) open pore current up to an hour; (B) temporary current blockades due to resistive pulses caused by translocation of single-stranded linear plasmid DNA (ssDNA) molecules recorded for about an hour.

5.6. Detection and Identification of Biomolecules

After verifying the functionality and characterizing the performance of different variations of the flow detector in the preceding chapters, first experiments with actual biomolecules will be presented in the subsequent chapters. Biomolecules of several nanometers diameter will be studied. Therefore, nanopores of the 'intermediate' size will be used for these experiments, i.e. electron beam patterned and thermally post processed pores with about 22 nm diameter as described in chapter 4.3. Two classes of biomolecules with outstanding importance to the biomedical field will be used as nanoparticles under test for the translocation experiments: Double-stranded deoxyribonucleic acid (dsDNA) and the protein bovine serum albumin (BSA).

Nucleic acids are molecules that carry the genetic information used in the development and function of all living organisms. Detailed information about dsDNA therefore is indispensable in modern life sciences. Nanopore-based analysis of DNA investigates variations in the nanostructure of the DNA, such as length, diameter, or sequence of the relative orientation (conformation) of DNA building blocks. Detection and analysis of such variations, such as the detection of genetic variabilities (i.e. detection of subtle variations in local DNA structure) or the detection of phenotypic variabilities (i.e. detection of variations in local protein structure) can support the study of the relationship between genetic and phenotypic variations (i.e. how variations in the structure of DNA affects the structure/function of proteins and therefore the basis of different diseases), and the study of DNA-protein interactions (i.e. structural interactions between proteins such as transcription factors and DNA) and therefore the effects of DNA-binding proteins on the expression of certain genes, study of DNA sequencing.

The double helical structure of dsDNA has a fixed diameter of about 2 nm, but the length can vary significantly. We applied dsDNA molecules with a length of about 5,400 'steps' in the

double helix, referred to as5.4 kilobase-pairs (kbp). These molecules were obtained by cleavage of longer pcDNA3.1^{+} plasmid. This plasmid had been purchased from Invitrogen^{TM}/Life Technologies. Cleavage was performed by our group using the commonly applied Hind III restriction enzyme.

Albumin is the second biomolecule selected for these initial studies. Albumin is a major blood protein and occurs in humans (human albumin) as well as in animals. Albumin is normally filtered back by the kidneys by the glomerular filtration. It should not be found in urine. The maximum normal concentration is considered to be on the order of 30 µg/ml. If found in the urine in larger quantities, it is usually a clear indication of kidney or liver dysfunction. Albumin has a diameter of typically 4 nm to 10 nm. It is considered the largest of several thousands of potential urine ingredients, its detection with a nanopore seems like an excellent biomedical application. The bovine form of albumin is readily available commercially. We obtained it from Sigma-Aldrich.

The translocation experiments with dsDNA and BSA biomolecules are conducted with a slightly acidic, buffered KCl electrolyte. This on one hand limits further negative surface charging of biomolecules and pores which would occur in a basic environment, and on the other hand is compatible with biological conditions required by the biomolecules analysed. The solution has a pH-value of 6.0 ± 0.2 and a concentration of 0.1 M.

Two AgCl electrodes create a transmembrane potential, inducing an open pore current through the nanopore. Individual populations of either dsDNA or BSA biomolecules, each at a final concentration of 10 nM, or a mixed population containing both biomolecules together, are introduced into the electrolyte in the reservoir on the negative side of the membrane (*cis*). The

current traces are measured, and the open pore current as well as blockade events are recorded and analysed.

5.6.1. Factors impacting the Translocation of dsDNA Molecules

In the absence of biomolecules, a constant open pore current of approximately 430 pA is induced at a driving voltage of 600 mV. The open pore current does not change upon addition of dsDNA molecules to the electrolyte, but numerous distinct stochastic current blockade events representative of translocation of dsDNA molecules through nanopores from *cis* to the *trans* side of the membrane occur. These translocation events disappear upon flushing out the dsDNA molecules from the *cis* chamber. Figure 5.13 displays a typical current recording. After about 4 s, DNA molecules are added to the electrolyte, and blockade events with amplitude of approximately 20 pA are observed roughly every second. A more detailed trace of a blockade event is represented in the inset. While the y-axis (current) remained unchanged, the x-axis (time scale) is now significantly expanded. The overall time for the blockade is about 0.22 ms.

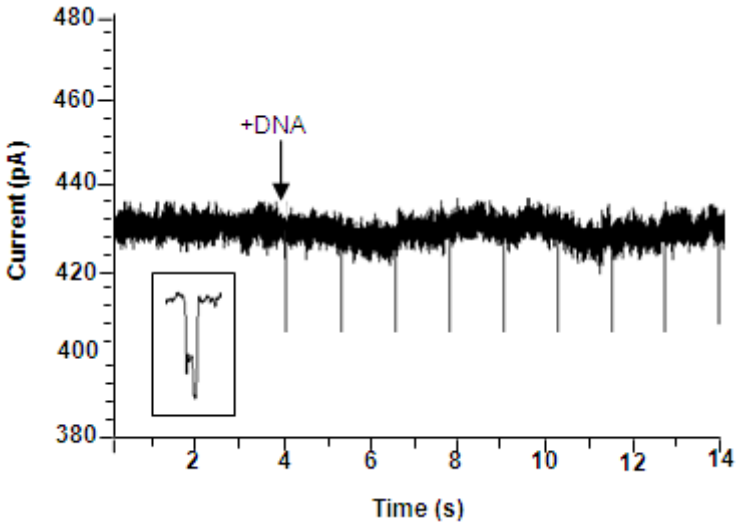

Figure 5.13: Patch clamp measurement of the ionic current through a 22 nm wide nanopore at 600 mV driving voltage. The open pore current is unaffected by the addition of dsDNA molecules after 4 seconds. Translocations of the molecules are identified by blockade events roughly every second. The inset displays an expanded time line of such a blockade to ms scale.

A biomolecule constitutes a topologically much more complex object than the nanospheres studied so far. Biomolecule surface charging and electric double layers depending on the experimental conditions further complicate the electrostatic boundary conditions. Translocations of the biomolecules therefore depend on a variety of parameters. Details of the recorded traces can, likewise, reveal much information about the translocating particles. The exact interactions during translocation of biomolecules will therefore be discussed in the subsequent sections.

So far, we always considered resistive pulses, or current blockades, during translocation events. DNA molecules translocating nanopores can actually cause both, downward current spikes of current deductions and upward spikes of current enhancements [79, 72, 26, 80]. The salt concentration of the electrolyte has been identified to play a key role in determining the sign

of the change in current as molecules pass through nanopores. Smeets et al. [72] showed that current deductions produced upon translocation of DNA molecules are gradually converted to current enhancement spikes as the salt concentration of the KCl electrolyte decreases from 1 M to less than 0.3 M. Contrary to this observation are the translocation events in our experiments almost exclusively current deduction spikes even though an electrolyte of 0.1 M concentration is used. This indicates that the salt concentration of the electrolyte cannot be the only factor determining the sign of current changes, or changes in nanopore conductance, upon translocation of dsDNA molecules through nanopores.

A closer analysis reveals that there are two competing effects for the nanopore conductance in the presence of a DNA molecule inside a nanopore: First, the physical volume of the DNA leads to a reduction in total electrolyte ion population in the nanopore, thereby reducing the nanopore conductance. Secondly, DNA molecules are negatively charged, adding counter-ions to the pore area, which results in a larger number of free charge carriers and therefore a conductance enhancement. The net effect of a translocating DNA molecule on the nanopore conductance can be influenced by several factors. One of these is the aforementioned ionic strength, or salt concentration of the electrolyte. Others include the *conformational state of the DNA* and, thus the length and surface charge of the molecule exposed to the electrolyte. Finally, the *surface charge of the nanopore* and the electrolyte ions form an electric double-layer. Under the impact of an external field induced by the electrodes, the Coulomb force on the net charge in this double layer creates a movement in the electrolyte, referred to as the electro-osmotic flow (EOF) through the pore. The EOF is independent of the pore size under most conditions, but is a function of the voltage applied across the nanopore [72, 26, 80, 81].

Among the potential contributions, the conformational state of the DNA has the largest impact on the sign of the current changes. The observed large number of current deduction spikes is indicative of the DNA molecules translocating through the nanopore in their *partially-folded* conformation: under the use of a constant amount of the applied voltage of 600 mV, the ionic strength of 0.1 M, and the fixed negative pore surface charge, fully or partially folded DNA molecules occupy a larger fraction of the available pore size and therefore displace a larger fraction of the electrolyte potassium (K^+) and chloride (Cl^-) ions flowing through the pore than it would be the case for unfolded DNA. These displaced, or temporarily lost, electrolyte ions decrease the number of free charge carriers and therefore decrease the pore conductance. This reduction cannot be completely compensated by the electrostatic attraction of K+ ions to the pore due to the surface charge of translocating DNA molecules. The net effect is therefore a reduction in conductance and current. Current enhancement spikes are only observed if DNA molecules are unfolded. Such longer/stretched DNA molecules occupy a smaller fraction of the pore cross section and, therefore, displace fewer electrolyte ions flowing through the nanopore. Furthermore, a larger fraction of the DNA molecule surface is exposed to the electrolyte, such that the constant surface charge can now attract more electrolyte counter-ions to the longer DNA molecules flowing through the nanopore.

Another potential reason for observing current deduction rather than current enhancement spikes at any DNA conformation has been reported in literature, but is statistically very unlikely to occur: Occasionally, a second DNA molecule in any conformation can be captured in the pore before the first captured DNA molecule leaves the nanopore. Steinbock et al. [82] reported the average time between two subsequent translocation events for dsDNA molecules to be around 0.14 s at a driving voltage of 500 mV, a pore size of 19 nm and a KCl electrolyte concentration

of 0.5 M. The translocation time is about three orders of magnitude shorter. Under conditions comparable to these of Steinbock et al, e.g. at a driving voltage of 600 mV, we determine the average translocation time t_D to be 0.22 ms. This is further explained in the subsequent chapter. Based on these numbers, the probability of two DNA molecules passing through a nanopore at the same time is very low.

The conformation state of individual dsDNA molecules remains the most important factor in predicting current changes upon translocation. As explained above, the data in the present study suggests the presence of at least partially folded molecules. This is in good agreement with results reported in literature. Using pores of comparable size, a substantial fraction of translocation events is attributed to fully-folded or partially-folded DNA molecules entering the pore [21, 22]. Further analysis is based on the fine structure of the translocation signal. The measurements in the present study reveal a typical series of blockade events with two amplitude levels as a single DNA molecule translocates through the nanopore. Such a bi-level signature is reproduced in the inset of Figure 5.13. Such bi-level events were previously reported by others [21, 22, 83, 72, 80 and 84]. They are attributed to partially-folded DNA molecules translocating through a nanopore. Following the nomenclature used by Storm et al. [22], the bi-level event in Figure 5.13 is a 12 events, where a DNA molecule is in its partially-folded conformation, entering the nanopore in its unfolded state (described by the first digit as number 1) and exiting the nanopore in its folded conformation (described by the second digit as number 2). The hypothesis of partially-folded molecules is not only supported by other nanopore research groups, but also by general biochemical considerations: These considerations compare the pH value of the electrolyte solution to the pK_a value of the DNA molecule. pK_a here stands for the negative decadic logarithm of the acidic dissociation constant K_a: $pK_a = -log_{10} K_a$. Large pK_a

values represent smaller amounts of dissociation, or a weaker acid, at a given pH value. DNA molecules are naturally highly negatively-charged, folded biopolymers with a pK_a value of around 3.8 to 4.5 [85]. Bhattacharya et al. [85] determined a regime for pK_a values below the pH value and a regime for pK_a values above the pH value, and associated these regimes with conformational states. If the pH value is lower than the pK_a value, atom N1 of nucleotide A and atom N3 of nucleotide C are likely to accept a proton from the electrolyte solution, neutralizing the net charge of the entire nucleotide. This protonation of the nucleotides disrupts the delicate balance of the forces holding together the double helix, and the helix denatures. In the other regime with pH values above the pK_a value, DNA molecules are stabilized in their native highly negatively-charged and fully-folded or partially-folded conformation. This regime applies in the experiments we conducted, using a slightly acidic unbuffered electrolyte with a pH value of 6.0 ± 0.2. Therefore, a large number of dsDNA molecules are expected to be in their partially-folded conformation. The closer the pH of the electrolyte solution gets to pH 8.0, the more DNA molecules are stabilized in their natural native folded conformation. Further theoretical and mathematical studies along with computer simulations could be applied to study conformational states in much more detail. However, this is beyond the scope of the present study.

An important characteristic of translocation is the minimum driving voltage required for complete translocation events. Starting at this threshold voltage the barriers to permeation are overcome and DNA molecules are impelled through a specific nanopore under specific operational conditions. The threshold voltage depends on factors such as translocating molecule and pore dimensions, total charge on the pore surface and inner walls, the total charge on the translocating molecules, as well as electrolyte concentration, temperatures, etc. For a given molecule, decreasing the pore diameter increases the threshold voltage, possibly due to the

presence of more extensive interactions between the translocating DNA molecules and pore surface and inner walls [86]. Our experiments established a threshold voltage of about 400 mV for dsDNA molecules and the experimental conditions previously stated. This is a larger threshold voltage than in many comparable studies using even smaller pore diameters [87, 72, 88]. We associate this comparatively high threshold voltage with the unusual membrane thickness or length of the nanopores of 1 µm. This is in agreement with Harrell et al. [89] who suggest that the length of nanopores plays an important role in determination of the threshold voltage Harrell found a threshold voltage as high as 600 mV for 10 µm long conical nanopores. Liu et al. [84] made a valuable contribution to estimate the impact of pore length on the threshold voltage by investigating the electric potential and field distribution in conical nanopores with different thicknesses, ranging from 50 nm to 250 nm. The applied driving voltage was 300 mV. They have shown that the electric field strength at the pore entrance decreases with an increasing pore length. Therefore, the electric force (F_E) driving DNA molecules toward the pore is smaller in thicker membranes or longer nanopores. This causes a high threshold voltage to capture the molecules.

The driving voltage does not only determine whether translocation events are possible, but also when further increasing the potential, several characteristics of the observed translocations change. At otherwise constant conditions, the rate of translocations, for instance, increases with the applied voltage. Figure 5.14 A shows measurements at three voltage levels of 400 mV (top), 500 mV (center), and 600 mV (bottom). Each current trace represents 14 seconds. The number of dsDNA translocation events through the 22 nm wide nanopore in the considered time interval almost doubles. Our results correlate well with several studies measuring an increased rate of DNA translocations through artificial nanopores over voltages ranging from 100 mV to 1000 mV

[90, 89, 26]. According to Wanunu et al. [80], a strong decrease in translocation time of DNA molecules with increasing voltage could result in an increased rate of translocation events through nanopores. The specifics of the rate increase with voltage, however, seem to be highly dependent on the extent of DNA/pore interaction, and a general statement whether the increase observed follows a linear or non-linear relationship cannot be made. Higher DNA/nanopore interactions due to their negative charges, for instance, tend to reduce the linearity.

Another translocation characteristic changing with increased voltage, besides increased number of blockade events per unit of time, is an increasing amplitude of individual blockade events. The current deductions increase from top to bottom graph in Figure 5.14 A. These I_{block} values are plotted as a function of the driving voltage in Figure 5.14 B. The excellent fit of the data points measured with a linear regression indicates a linear dependence of the current blockade amplitude on the driving voltage. Under the experimental conditions used, the blockade increase amounts to 5 pA per 100 mV. Liu et al. [84] also reported a linear increase in the DNA blockade amplitude with voltage. In their case, the increase amounted to ~ 85 pA per 100 mV. As it was explained in nanoparticles translocation, the larger I_{block} values as a function of voltage can be resulted either by more interaction in between forces involved in translocation for each individual DNA or by passing multiple DNA at the same time through the pore.

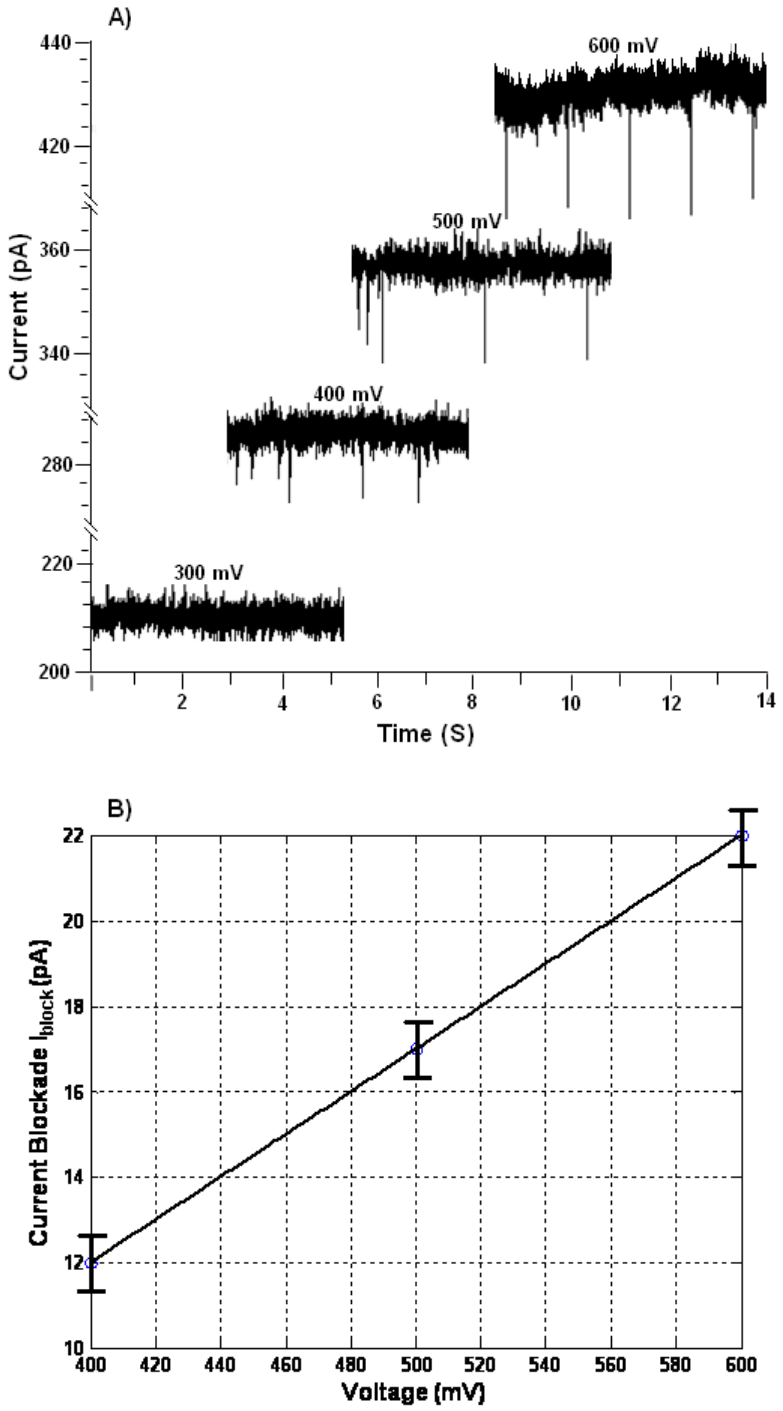

Figure 5.14: Translocation event recordings and current blockade- I_{block} (pA) values as a function of the applied voltage (mV) for 5.4 kbp dsDNA molecules (10 nM concentration) translocating through single 22-nm diameter nanopores at 0.1 M KCl electrolyte solution: (A)

Current-time traces indicate an increasing number of I_{block} events during a 14 second-long time (event rate) for molecules translocating through nanopores, as the voltage increases from 300 to 600 mV; (B) The plot demonstrates the means of I_{block} values for downward translocation events obtained as the voltage increases across the nanopores from 400 to 600 mV. Average amount of experimental results obtain a tolerances of ± 0.69 pA shown with error bar.

5.6.2. Translocation Dynamics of dsDNA Molecules

Interaction with complex biomolecules is much more complicated than with comparatively simple nanospheres. Statistically occurring events have a larger impact on, e.g., translocations through nanopores. In-depth studies therefore require a large number of quantitative analyses of the current blockade I_{block} and the translocation time t_D. Figure 5.15 for instance summarizes 1000 dsDNA translocation events at an acceleration voltage of 600 mV. Taken into account within these 1000 events are all those which exhibit a current blockade value exceeding the open pore current noise level of about 8 pA. Therefore, the events recorded may or may not represent successful transitions through the pore. Figure 5.15 A represents a semi-logarithmic scatter plot of the current blockade I_{block} versus the translocation time t_D. I_{block} values given are the contributions beyond the open pore current noise level. The scatter plot shows a large cloud of 1000 events varying in I_{block} from approximately 2 pA to 43 pA and in t_D from 0.02 ms to 5 ms. A closer analysis however reveals two distinct populations as indicated by the dotted perimeter lines in the graph. One group has a low mean blockade of 8.17 pA, the other has a much larger average blockade of 22.4 pA. These two groups show very distinct time duration. Low blockade amplitudes correlate with short time duration between 0.02 ms and 0.25 ms. In contrast, the events with larger current blockades take longer transition times and a larger spread of these t_D

values ranging from 0.1 ms to 5 ms. There is hardly any overlap in the time duration between the two populations: *A*lmost all low-t_D-events are associated with the low blockade amplitude group.

Statistical evidence of the intuitive grouping based on the scatter plot is graphically represented in Figures 5.15 B-D. The translocation events are characterized in terms of the most probable current blockade I_{block} and time duration t_D values. The number of events is counted as a function of the current blockade or the time duration respectively. The bin width for the current blockade is 1 pA, the bin width for the translocation time is 0.05 ms. The raw values obtained are shown in Figure 5.15 A along with Gaussian fits (Figure B) and exponential distributions of the I_{block} and t_D histograms (Figures C, D). Corresponding to the intuitive grouping above, both, the current blockade and the time duration have a bi-modal distribution. Figure B identifies the relative current blockade average for the population with smaller values to be $I_{block} = 8.17 \pm 0.2\ pA$. Figure C correlates this to an average time duration of $t_D = 0.033 \pm 0.003\ ms$. The population with larger values has a current blockade amplitude of $I_{block} = 22.4 \pm 0.69\ pA$ (Figure B) and a translocation time $t_D = 0.202 \pm 0.009\ ms$ (Figure D).

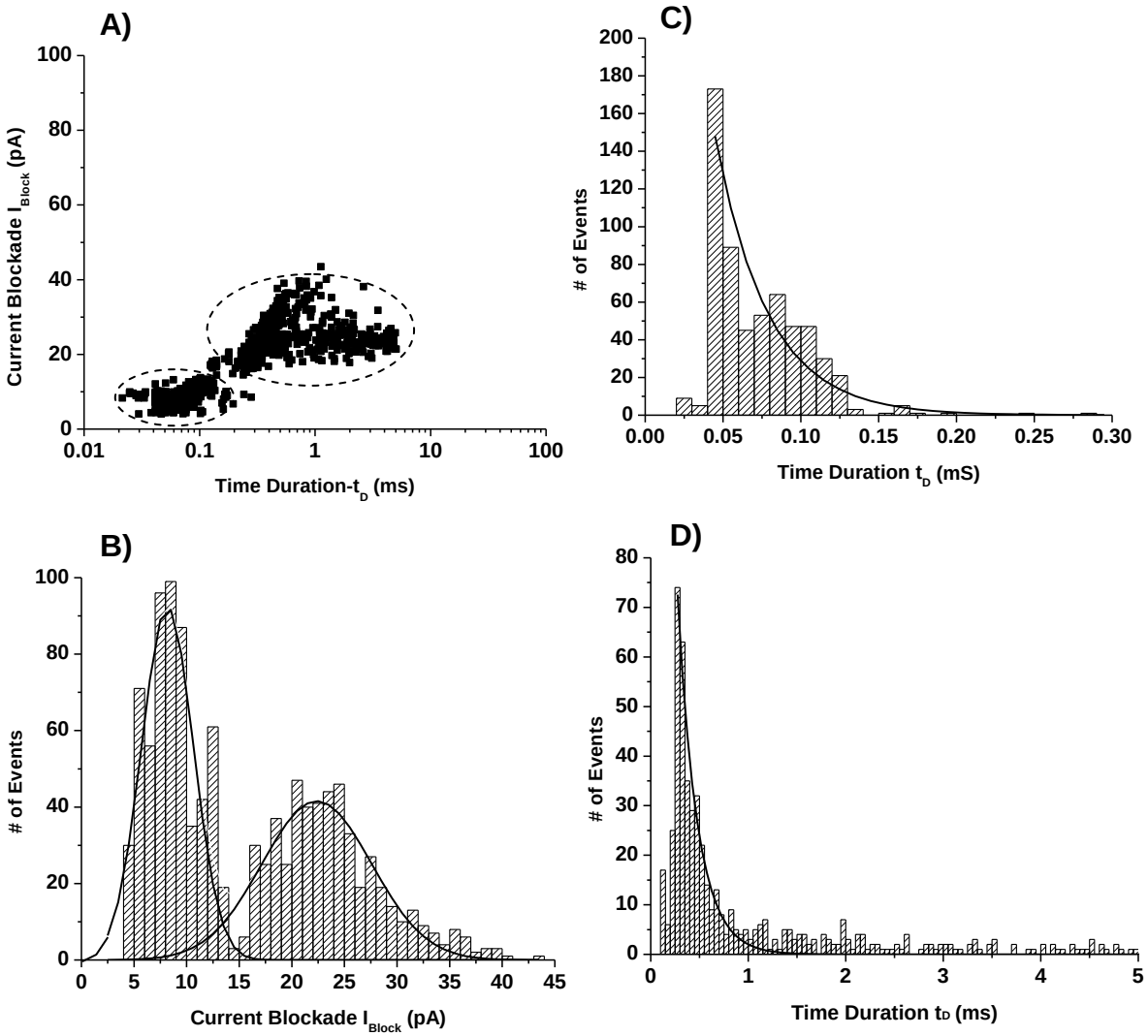

Figure 5.15: Statistical evaluation of patch clamp measurements of the current blockade created by 5.4-kbp dsDNA molecules in 0.1 M KCl electrolyte translocating through a 22 nm wide nanopore at 600 mV driving voltage: (A) semi-logarithmic scatter plot of the current blockade I_{open} versus time duration t_D for 1000 events. The dotted perimeters indicate two distinct populations of events having both a low current blockade and short time duration (I_{block} *= 8.17 ± 0.2 pA*; t_D *= 0.033 ± 0.003 ms*) or a high current blockade and large time duration (I_{block} *= 22.4 ± 0.69 pA*; t_D *= 0.202 ± 0.009 ms*); (B) Histogram for the 1000 current blockade

events, revealing a bi-modal distribution; (C) Histogram for the time duration of the low blockade/ short time population; (D) Histogram for the time duration of the large blockade / long time population.

Such a bi-modal distribution has previously been reported in literature as a typical feature of nanopore experiments for all examined DNA lengths [80, 72]. These studies revealed different behaviour of the populations with smaller I_{block} and t_D values compared to those with larger number values: Small-number-value events are associated with incomplete translocations, also referred to as *collisions* or *bumps* on the surface or in the entrance area of the nanopores. These molecules do not reach the other end of the pore. Molecules do not need to eventually change their conformation as might be needed for translocation. Consequently, the duration of these surface-related effects is independent of the length of the molecule. Complete or successful translocations through the pores are associated with the larger-number-value population. Their translocation time depends on the length of the migrating molecule [72]. The spread in translocation times determined for this larger-number-value population consequently is much larger, based on the variety of DNA molecule lengths in the examined sample. We therefore correlate the events with small I_{block} values to unsuccessful bumpings/collisions to the nanopores surface, and the events with high I_{block} values to full translocations through single nanopores. We observe a three-fold variation in the characteristic time-scale associated with the events of large I_{block} *(± 0.009 ms*) as successful translocations strongly depend on the length of the specific DNA molecule. The time-scale associated with the events of small I_{block} exhibits very weak, if any, length dependence, and therefore varies much less *(± 0.003 ms*).

The observed behaviour was not only previously reported for artificial nanopores, but for self-assembled biopores as well. Several other studies investigating DNA translocation through α-hemolysin protein nanopores identified the short and shallow current change events as random bumping/collisions with the pore entrance, whereas longer and deeper events were identified as successful translocations through the pores [10, 65, 91, 92].

The spread in current blockade amplitude and translocation time observed mandates a more detailed review of the underlying physical effects to validate and assess the measured signal. Figure 5.15 documents a broader distribution in both, current blockade amplitude and translocation time, for complete translocation events when compared to bumping/collisions. An explanation is offered by analyzing the equilibrium of relevant forces:

Three main forces act on DNA molecules as they translocate through a nanopore in the presence of an outer electric field: The electrostatic force F_E, the viscous drag force F_D, and the random thermal force F_R [85, 88, 93]. Bhattacharya et al. [85] applied a general equation of motion

$$m\, dv/dt = F_E + F_D + F_R \tag{5.4}$$

with an inertial term related to the change of momentum over time based on the mass of the molecule m on the left hand side of the equation.

- The electrostatic force F_E on the translocating molecules has two components: The potential difference applied across the pore by the external electrodes imprints a force experienced by all mobile charge carriers in the electrolyte. Additionally, the total net charge on the DNA molecule surface and the total charge on the pore surface and inner walls result in Columb interactions between the charged DNA molecules and pore surface.

- The viscous drag force F_D results from the mass of moving particles, such as DNA molecules or electrolyte ingredients, and the viscosity in the fluid. The Navier-Stokes equation mathematically relates these to the flow profile for incompressible fluids.
- The fluctuating random thermal force F_R is strongly related to the viscous force. Its origin, like that of the F_D, lies in the random bumping/collisions of the solute molecules of electrolyte solution with the moving DNA molecules. F_R however, is not a function of the flow pattern established, but rather a stochastic contribution. It is a major source of thermal noise in the open pore current.

All three forces increase with the length and depend on the conformation of DNA molecules translocating a nanopore. The required translocation time t_D, in turn, is a strong function of the length and conformation of the DNA molecule [80, 72, 84]. Wanunu et al. [80] described increased t_D values for an increased length of DNA molecules from 0.15 kbp to 20 kbp because of an increased interaction between nanopore and the passing DNA molecules. This increase in t_D is particularly well described for increased length of unfolded DNA molecules [72, 84].

A sample of DNA with non-uniform length distribution, as always present in reality, will therefore necessarily feature a variety of translocation times, or a comparatively large spread, as long as all contributions of the above mentioned equation of motion are relevant, i.e. for all complete translocations. A few approaches can be contemplated to reduce the spread in translocation time. Surface charging contributions to the electrostatic force F_E are not needed for the translocation itself, unlike the electrostatic aspect of the driving voltage. Surface charges on the pore walls can be minimized by adapted pore post processing or by chemical coatings. A slightly reduced spread of the translocation time of similar DNA molecules could support the identification and study of translocation events. Regardless of the impact of F_E will the random

thermal force F_R always be present. F_R acts statistically even on DNA molecules with exactly the same lengths and conformation. This will always cause some variations and spread in the values of t_D.

In summary, the study of translocation dynamics of a biomolecule migrating through a nanopore is subject to many parameters and complex to predict. Comparisons to other studies therefore are complicated and current blockade amplitude and translocation time values vary substantially even for the same biomolecule. The mean dsDNA translocation time in the present study of $t_D = 0.202\ ms$, for instance, is notably shorter than the 1 ms to 2 ms values reported by some other studies [22, 72, 84]. These studies investigate DNA molecules as well, but many other parameters vary slightly. Four of these will subsequently be discussed:

1. The diameter of the nanopores presented here is 22 nm, which is slightly larger than those reported in the other studies, between 10 nm and 20 nm. A faster translocation through larger pores is to be expected as explained in chapter 3.2.2.
2. The driving voltage used here is between 400 mV and 600 mV. This is similar to those in the other studies mentioned, where a typical driving voltage is around 500 mV. Increased voltages have been shown to strongly decrease the translocation time [84].
3. The dsDNA molecules used here are mostly in their partially-folded conformation, which is known to decrease the translocation time needed compared to unfolded counterparts [72].
4. In the present study, some of the negative charges present on the PMMA membrane surface and nanopore inner walls are neutralized. This neutralization occurs during the processing sequence described, when UV exposure is applied to fine-tune the pore dimension. The use of a slightly acidic electrolyte with a pH value of 6.0 ± 0.2 further

supports this neutralization. A reduced amount of surface charge on membrane and pore walls reduces the electro-osmotic flow (EOF) induced by the electric double layer formed between pore surface and free charge carriers in the electrolyte. As previously mentioned, the EOF moves in the opposite direction to the electrophoretic flow and, therefore, is inhibitory to the transport of DNA molecules through nanopores [90, 94, 84]. The reduced amount of EOF therefore contributes to a reduced translocation time in the present study in comparison with previous investigations.

The literature review suggests there are sufficient reasons that might explain a faster translocation observed here compared to the other studies mentioned and justifies further systematic studies.

5.6.3. Translocation and Translocation Dynamics of BSA Protein Molecules

After analyzing dsDNA molecules in the previous chapter, the flow detector system now gets evaluated analyzing another species of biomolecules, BSA proteins. A previously used detector system can be reused if the DNA molecules are flushed from the cell compartments/reservoirs by replacing the electrolyte containing DNA molecules with fresh electrolyte solution.

The open pore current reaches its standard value of 430 pA at 600 mV, as previously established in chapters 5.1 to 5.6. The noise amounts to about 15 pA. BSA protein molecules are then added to the *cis* compartment of the electrophoretic detector system, which induces numerous short-lived current blockade events with varying amplitude and duration. Figure 5.16 shows a typical current trace. In accordance with experiments using dsDNA molecules in the preceding section, compare Figure 5.13, and in agreement with the recent studies by Talaga and Li [25], Oukhaled et al. [95], and Cressiot et al. [96], the protein-induced current blockade are

voltage-dependent. Translocation frequency and blockade amplitude increase with increasing applied transmembrane voltage. Details are given in Figure 5.17.

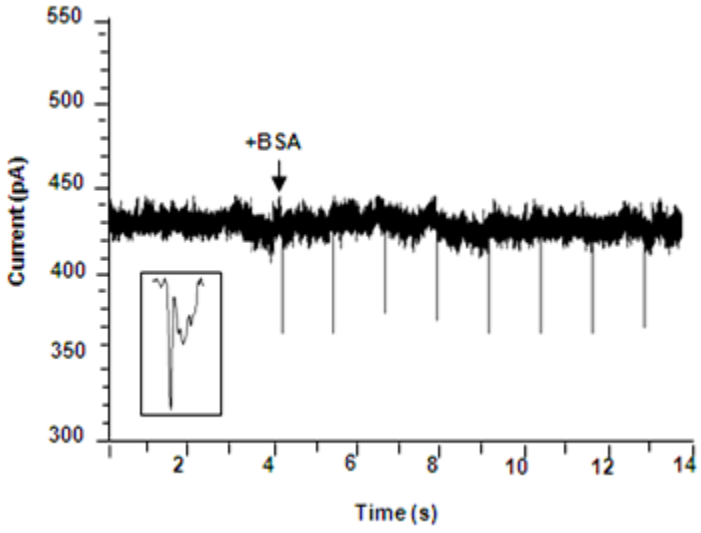

Figure 5.16: Patch clamp measurement of the ionic current through a 22 nm wide nanopore at 600 mV driving voltage. The open pore current is unaffected by the addition of BSA protein molecules after 14 seconds. Translocations of the molecules are identified by blockade events roughly every second. The inset displays an expanded time line of such a blockade to ms scale.

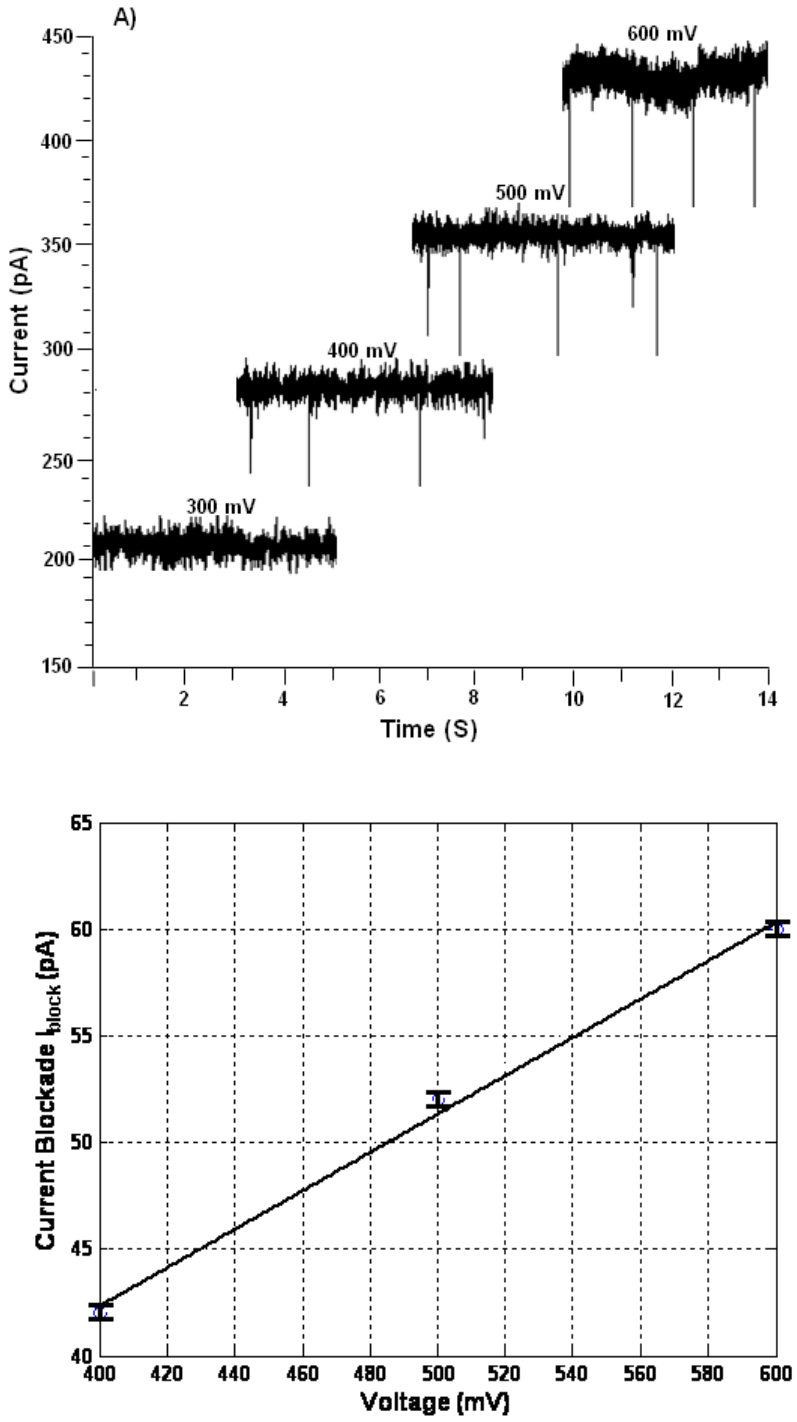

Figure 5.17: Patch clamp measurement of the ionic current through a 22 nm wide nanopore with translocation events of BSA protein molecules of 10 nM concentration in 0.1 M KCl electrolyte: (A) 14 s long current traces indicating an increasing translocation rate with increasing voltage

(400 mV top graph, 500 mV center graph, 600 mV bottom graph); (B) Increasing current blockade amplitude as a linear function of the driving voltage (measurement and linear fit). Average amount of experimental results obtain a tolerances of ± 0.19 pA shown with error bar.

Figure 5.18 further details the translocation dynamics, focussing on the current blockade amplitude I_{block} and the translocation time t_D. Like in chapter 5.5 for dsDNA, a scatter plot of about 1000 BSA protein translocation events reveals two distinct populations Figure 5.18 A). At 600 mV driving voltage, the population with low blockade amplitudes ranging between 19 pA and 52 pA correlates with short time duration of 0.01 ms to 0.75 ms. The population with high blockade amplitudes ranging between 48 pA and 80 pA correlates with long translocation times of 0.3 ms to 3.5 ms. The histogram of the current blockade in Figure 5.17 B statistically proves the bi-modal distribution. The characteristic mean blockade amplitude for low amplitude and fast events is $I_{block} = 26.27 \pm 0.12\ pA$, while it is $I_{block} = 60.14 \pm 0.19\ pA$ for large amplitude and slow events. Figure 5.18 C identifies the characteristic mean time duration for the low amplitude and fast events population to be $t_D = 0.066 \pm 0.001\ ms$, while it is $t_D = 0.59 \pm 0.08\ ms$ or an order of magnitude slower for the other population, as seen in Figure 5.18 D. Such a bi-modal characteristic of BSA protein translocations through a silicon nitride nanopore has previously been detected using chemiluminescese analysis [24]. Similar to the results presented here, two clusters of blockade events were observed. Cluster 1 features low blockade amplitude of about 20 pA, while the most probable high amplitude blockade of cluster 2 amounts to 50 pA.

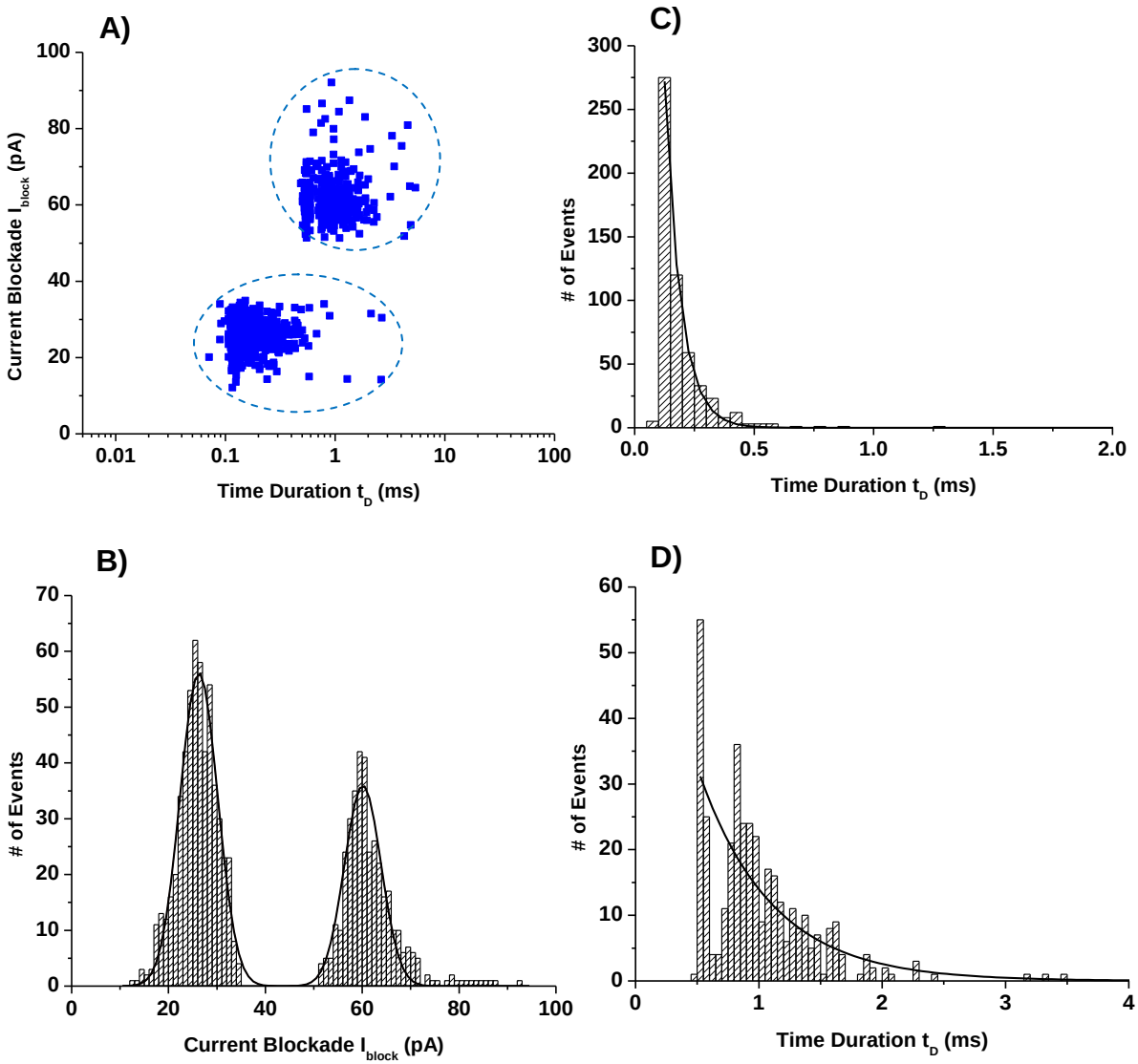

Figure 5.18: Statistical evaluation of patch clamp measurements of the current blockade created by BSA protein molecules in 0.1 M KCl electrolyte translocating through a 22 nm wide nanopore at 600 mV driving voltage: (A) semi-logarithmic scatter plot of the current blockade I_{block} versus time duration t_D for about 1000 events. The dotted perimeters indicate two distinct populations of events having either a low current blockade and short translocation time (I_{block} = *26.27 ± 0.12 pA*; t_D = *0.066 ± 0.001 ms*) or a high current blockade and large time duration (I_{block} = 60.14 ± 0.19 pA; t_D = *0.59 ± 0.08 ms*); (B) Histogram for all current blockade

events, revealing a bi-modal distribution; (C) Histogram for the time duration of the low blockade/short time population; (D) Histogram for the translocation time of the large blockade/long time population.

The measured results are in good agreement with literature studies of similar biomolecules: Translocation characteristics depend, among others, on the conformation and the surface charge of the migrating molecules. For example, changes in size and structure of protein molecules, such as BSA, were previously reported upon variations of the electrolyte pH value [24]. Such changes in the geometrical structure have different impact on the migration dynamics, depending on the kind of events: Unsuccessful translocation, referred to as *bumping* or *collision*, do not usually change much in response to the changes in the structure of the passing protein molecules. In contrast, dynamics of successful, complete translocation events were shown to be highly specific to the structure of protein molecules migrating through the pores: Fologea et al. [24] compared two protein molecules with different structure, fibrinogen and BSA. Fibrinogen is larger in size than Albumin. Fibrinogen has a unified atomic mass of 340,000 Da, which is five times the mass of BSA with 66,430 Da. The relative shape differs as well, with the fibrinogen structure being described as an elongated molecule of approximately 47.5 nm in length, in contrast to BSA with a globular shape with 4-10 nm diameter and a length of about 14 nm [89, 97]. These proteins are good candidates to analyse the isolated effect of structural differences because the surface charge is almost identical. In a neutral electrolyte with a pH value of 7.0, fibrinogen has a negative net charge of 16 elemental charges, very similar to BSA with 18 e^-. The structural differences lead to larger current blockade amplitudes and longer translocation times for fibrinogen molecules compared to those of BSA [24].

Other studies focus on both, the impact of structure and charge, on translocation dynamics. Using a silicon nitride nanopore with fixed driving voltage and electrolyte concentration, Talaga and Li [25] discussed in detail the effects of the *primary- amino acid* (*aa*) sequence on translocation properties. They analyzed the charge of every individual *aa* and therefore the net charge of the entire protein sequence, as well as the effects of loops likely formed along different segments of a protein sequence, on the translocation dynamics of *β-lactoglobulin* (βLGa) and *histidine-containing- phosphocarrier* (HPr) proteins. Three different conformational states, linear unfolded, partially-folded, and fully-folded, were enforced using three concentrations of urea as a denaturing agent. Translocation of linear βLGa protein, compared to that of linear HPr protein, induced higher current blockade amplitude due to the presence of bigger, bulkier *aas* in the βLGa sequence. Furthermore, formation of loops involving various *aa* residues on different segments of βLGa sequence was shown to result in a broad distribution of current blockade and translocation time values. Similar to the above studies, Oukhaled et al. [95] and Cressiot et al. [96] further analyzed and compared the effects of different structural conformations, electrical charge distributions, hydrodynamic interactions, and drag forces on the mean I_{block} and t_D values of native and unfolded *maltose-binding protein* (MBP).

Based on the impact of size and structure of protein molecules on the translocation dynamics as described above, we complemented previous patch clamp measurements of BSA translocation through nanopores in slightly acidic regime with a pH value of 6.0 ± 0.2 by measurements in a strongly acidic regime with a pH value of 4.2. The additional protons available in an acidic regime will cause a net positive charge on the BSA molecules. According to Fologea et al. [24], BSA molecules with a net positive surface charge will become structurally denatured and change their shape. Analysis of the dynamics reveal that incomplete *bumping*/*collision* events as well as

complete translocation events still occur: Two populations of translocation events are recorded: One population has mean current blockade and transition time values very close to those reported for the fast, low magnitude blockade events at a pH value of 6.0. The other population has higher transition time, but lower current blockade values compared to the equivalent slow, high magnitude blockade population measured at a pH value of 6.0. Conclusions drawn from these results are as follows: The fast, low magnitude blockade events are comparable for both pH values and therefore almost independent of the structure of the migrating BSA molecules. These events therefore cannot represent complete translocations but are rather *bumpings* or *collisions* at the membrane surface in the entrance area of the pore. The slow, high amplitude blockade population however strongly reacts to the modified conditions of the experiment as expected for complete translocation of differently shaped proteins through the pores. This population therefore represents complete translocations at either pH value.

The fine structure of translocation events, as shown in the inset of Figure 5.16, typically features multiple current blockade levels. One potential explanation is the quasi-simultaneous transition of multiple, possibly agglomerated BSA molecules through the pore. Since almost all events show the same time structure, this is an unlikely assumption and would require an identical agglomeration of three molecules at all times. Furthermore, the translocation time is just a fraction of a percent of the time between translocations. The probability of simultaneous, but independent translocation of several BSA molecules therefore is extremely low. Finally, the observed fine structure seems to be independent of the BSA concentration and therefore unrelated to multi-particle statistics. A better explanation for the observed fine structure therefore is as follows: A single, partially-folded molecule could show multiple current blockade levels due to the presence of multiple stable loops formed on its surface. The fine structure would, in

this way, ‘image’ the structure of a complex molecule as it passes through the pore. According to the nomenclature proposed by Storm et al. [22], the blockade profile observed represents a *211 event*, where the first digit *number 2* represents the protein entering the nanopore in its *folded* state, and second and third digit *number 1* represents the protein being unfolded in two positions as it translocates through the nanopore.

The nanopore diameter of 22 nm is much larger than the diameter of BSA molecules, ranging from 4 nm to 10 nm. The pore size therefore cannot contribute to the unfolding of the BSA molecule upon translocation. A reason for the partial unfolding could be, however, associated with the pH value of the electrolyte: BSA molecules are negatively-charged under ambient conditions, naturally folded, globular molecules. Their isoelectric point, the IP value, ranges from 5.1 to 5.5. This is the pH regime in which the amount of positively and negatively charged amino acid molecules is the same, such that no amino acids migrate under the impact of an outside electric field. Keeping the molecules in an environment where the pH value exceeds the pI value has shown to better preserve the native folded structure of the molecules [24]. This is the case in the experiments described here with a pH value of 6.0. The BSA molecules only partially unfold, but still preserve their net negative surface charge. An indication of this maintained negative BSA surface charge at *pH = 6.0* is the fact that translocation blockades are only observed when BSA molecules are added to the *cis* chamber with its electrode being negatively-biased.

Besides the pH value of the electrolyte, a further driving force for partial unfolding of the BSA molecule is the electric field strength applied. Talaga and Li [25] demonstrated that a weak electrified strength provides little driving force to unfold βLGa protein molecules, while the stronger field applied in the present experiments likely contributes to at least partial unfolding.

Analysis of translocation events at an electrolyte pH value of 6.0 as described in the preceding chapters revealed that the majority of both, dsDNA and BSA molecules, are in their partially-folded conformation. Applying identical experimental conditions, such as 600 mV driving voltage and 0.1 M electrolyte concentration, therefore allows to directly compare translocation parameters measured. Current blockade amplitude and translocation time values are almost three-fold larger for BSA molecules than those obtained for dsDNA molecules ($I_{block,\,BSA} = 60.14 \pm 0.19\ pA$ and $t_{D,\,BSA} = 0.59 \pm 0.08\ ms$ versus $I_{block,\,DNA} = 22.4 \pm 0.69\ pA$ and $t_{D,\,DNA} = 0.202 \pm 0.009\ ms$). This can be explained based on the molecular structure. According to Talaga and Li [25], *amino acids* (*aas*) forming the backbone of proteins such as BSA are, in general, very heterogeneous in their partial molecular volumes and are much bulkier and bigger than the nucleotides forming the backbone of DNA molecules. This results in a larger fraction of the available volume of a single nanopore occupied by at least parts of a translocating BSA molecule than by a DNA molecule. Ultimately, it delivers larger mean current blockade amplitude for a segment of the BSA protein inside a nanopore compared to any segment of a dsDNA molecule with the same length as the protein. The sequence of various cross sections of BSA molecules, more than DNA molecules with their quasi-constant helical structure, contributes, besides the conformational state, to the complicated, multi-level fine structure of the translocation signals. This fine structure, as intuitively expected based on above explanations, is more complicated for BSA molecules (compare Figure 5.16) than for dsDNA (compare Figure 5.13). This volumetric consideration also holds for comparing the overall size of the molecules rather than their structural details: A BSA molecule has a diameter of approximately 6 nm, while the diameter of individual dsDNA molecules is about 2.2 nm. The same three-fold

dependence is observed as above. The overall size comparison by itself, however, would not justify the complicated fine structure of the blockade signal.

The above considerations justify the higher current blockade amplitude of BSA compared to DNA molecules. They do not explain, however, why the BSA molecules also require a longer translocation time. Nevertheless, seemingly over-proportionally long translocation times for proteins, such as BSA, have already been reported in literature [24, 25, 98, 99, 100, 74, 95, 96]. This phenomenon is not yet fully understood. However, two most likely explanations have been proposed:

The first one involves the attractive interactions that are present between the nanopore surface and its walls on one side and the proteins on the other. This leads to protein adsorption [25, 101], a quite common phenomenon, particularly on surfaces such as silicon nitride [102]. Evaluation of the translocation of proteins by Talaga and Li [25] predicted that proteins will stall at different positions within the *aa* sequence during their translocation through nanopores. This is due to the heterogeneity of charge along the *aa* sequence, resulting in different levels of interaction with a charged nanopore. Contrary to proteins, polynucleotides such as DNA molecules do not feature such an effect, therefore omit stalling events, and ultimately allow for faster translocation. Besides this charge heterogeneity-based stalling of proteins, they are also structurally more complex than DNA molecules: Loops, for instance, can be formed on the surface of linearized and partially-folded proteins by disulfide cross-linking. These loops affect both, the occupied volume and therefore the flow pattern in a nanopore, and the electrophoretic mobility of the molecule itself. The electrophoretic mobility inside the nanopore is reduced due to interactions with the charged pore, which impacts the translocation dynamics [25]. Besides loops formed locally on the surface, BSA molecules are also more likely to loop up as a whole. The

persistence length is a basic mechanical property quantifying the stiffness of a polymer. This persistence length is much shorter for proteins than it is for DNA molecules, suggesting that proteins are more likely to loop than DNA molecules. In summary, stalling inside the pores at different positions of the BSA *aa* sequence due to charge heterogeneity, as well as the formation of loops at different positions on the surface or in the overall structure of BSA molecules, could both result in a larger degree of protein/pore interaction and, therefore, longer translocation times for BSA compared to DNA molecules.

The second potential explanation for increased translocation times of proteins postulates that the electro-osmotic flow (EOF), which counteracts the electric field-induced translocation, may more strongly slow down proteins with larger molecular volumes compared to DNA. This may extend to a point where the flow even reverses. Firnkes et al. [103] studied this assumption in detail. The impact of the EOF can be controlled by adjusting the pore geometry (if the pore length is comparable to the double layer thickness), the pore net charge, pore surface properties, and the ionic strength and the pH value of the electrolyte [103, 104]. The parameters in our experimental conditions strongly limit the impact of the EOF, as also observed by Oukhaled et al. [95]. Here, the EOF does not seem to have a dominant effect on the translocation dynamics measured: The translocation times decrease inversely proportional with increased trans-membrane potential. Oukhaled et al. [95] demonstrated that the translocation time is expected to be inversely proportional to the applied transmembrane voltage only if energy barriers, such as the EOF inside a nanopore, is zero or at least minimal. In summary, the impact of the electro-osmotic flow on increased translocation times for proteins can be neglected under the experimental conditions studied here.

5.6.4. Discrimination of, and Differentiation between, Translocation of dsDNA and BSA Biomolecules

So far, the concept, fabrication, and functional testing of a novel, PMMA-based flow detector was presented. Detection of known molecules was repeatedly achieved. This raises hope to go beyond simple detection of the presence of test molecules, and to use the system for sensing selected properties associated with the molecules. This would allow for discrimination of different molecules and ultimately even enable biomedical applications where varying conformations of biomolecules, for instance, can reveal information about the conditions of an entire organism. Complete system evaluation requires entire teams of biochemists and goes far beyond the scope of this study. Initial discrimination experiments will, however, be presented to evaluate and illustrate the potential.

Both reservoirs of the electrophoretic flow detector systems are flushed and refilled with fresh electrolyte. A mixed population with equal concentrations of two chain-like biomolecules is introduced into the *cis* compartment of the detector systems. The molecules used are *double stranded linear plasmid DNA* (dsDNA) and the protein *Bovine Serum Albumin* (BSA), which were previously tested separately as described in chapters 5.6.1 to 5.6.3. Discrimination of translocation properties is based on different migration behavior through a nanopore. An essential part of the data analysis therefore is filtering out all those events which constitute incomplete translocations, such as bumping or collisions. Only successful, complete translocations can contain useful information and may be considered. As before, a scatter plot of current blockade amplitudes as a function of translocation time is produced. Based on information from the previous chapters, those events representing collisions or bumping of either dsDNA or BSA are filtered out, such that the remaining events must represent complete

translocations of either dsDNA or BSA molecules. Two separate populations of events remain after filtering. These are represented in Figure 5.19 A for a driving voltage of 600 mV and an electrolyte concentration of 0.1 M with a pH value of 6.0: One population exhibits current blockade amplitudes ranging from 13 pA to 38 pA with a translocation time between 0.16 ms and 4 ms. The other population shows larger current blockade amplitudes ranging from 52 pA to 73 pA with a translocation time between 0.42 ms and 5 ms.

The first population ($13\ pA \leq I_{block} \leq 38$) of the mixed sample corresponds very well with the data for complete translocations events using dsDNA molecules only ($17\ pA \leq I_{block} \leq 43$; compare chapter 5.6.2). Similar agreement is observed for the respective translocation time t_D. The second population ($52\ pA \leq I_{block} \leq 73$) of the mixed sample corresponds very well with the data for complete translocations events using BSA molecules only ($48\ pA \leq I_{open} \leq 90$; compare chapter 5.6.3). Similar agreement is, again, observed for the respective translocation time t_D.

All translocation events detected in the mixed sample can therefore clearly be identified as either a dsDNA or a BSA molecule migrating through the nanopore. The mixed sample constitutes a linear superposition of the individual species. Figure 5.18 B graphically extracts the dsDNA events and Figure 5.18 C represents the BSA events from the mixed scatter cloud. This proves the concept of an artificial nanopore in a PMMA-based electrophoretic detector system to detect and reliably discriminate between different types of biomolecules.

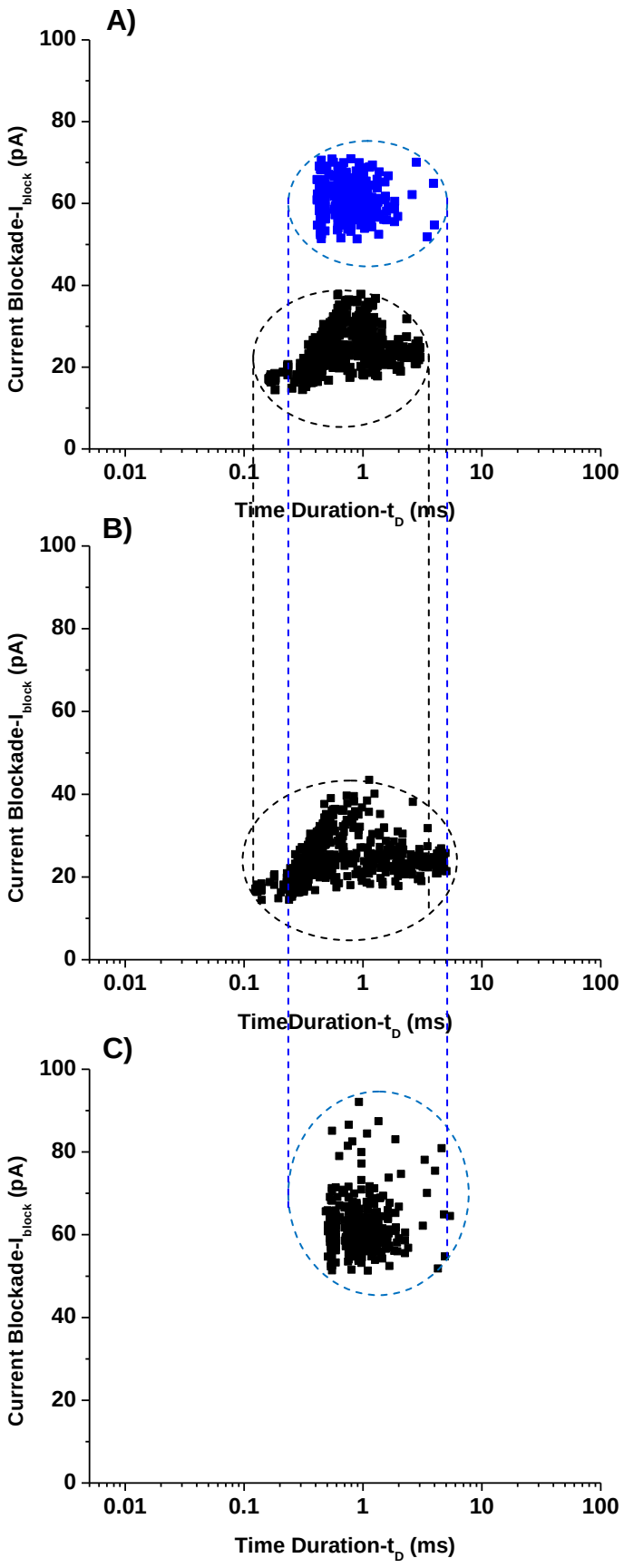
A)
B)
C)
Current Blockade-I$_{block}$ (pA)
Time Duration-t$_D$ (ms)
0
20
40
60
80
100
0.01
0.1
1
10
100

Figure 5.19: Translocation of dsDNA and BSA protein molecules through a 22 nm nanopore at 600 mV driving voltage and 0.1 M KCl electrolyte concentration: (A) Semi-logarithmic scatter plot of current blockade versus translocation time for dsDNA and BSA molecules in a mixed population. Only complete translocations through the pore are considered. The dotted perimeters highlight low current blockade population ($13\ \text{pA} \leq I_{block} \leq 38$) representing dsDNA molecules, and high current blockade population ($52\ pA \leq I_{open} \leq 73$) representing BSA molecules; (B) Scatter plot with a subset of the mixed population: data points identified as dsDNA translocations only; (C) Scatter plot with a subset of the mixed population: data points identified as BSA translocations only.

This chapter proved the functionality and applicability of the fabricated PMMA-based detector devices for biological applications. After characterization of the diameter of the pores and the electrochemical characterization of the entire device, the functionality and applicability of the detectors were demonstrated detecting silica nanoparticles and two different types of biomolecules.

6. Conclusion

6.1. Summary and Conclusions

During the course of this work, a concept for an all-polymer, nanopore-based electrophoretic flow detector was developed. The system is relatively easy to fabricate and allows to adapt the pore sizes for optimized detection of the particles of interest. Top-down as well as bottom-up fabrication approaches were applied to vary pore diameters over three orders of magnitude. A proof-of-concept included the entire sequence of fabrication, testing, and characterization of the detector at the example of pores of approximately 1.5 nm, 22 nm and 450 nm in diameter.

Poly methylmethacrylate (PMMA) was spincoated onto a sacrificial substrate and patterned by electron beam lithography (EBL) for simple adjustment of pore sizes. A generic 30 kV acceleration voltage EBL sequence was used. It allowed for patterning PMMA membranes of 1 µm thickness with pore diameters down to about 300 nm. An optional, subsequent thermal reflow process further shrinks pore diameters upon UV exposure. Sizes of about 22 nm were repeatedly demonstrated. Alternatively, naturally occurring a-hemolysin protein nanopores were self-assembled into a lipid bilayer membrane in the PMMA detector in a bottom-up fabrication approach. Biocompatible as well as process-compatible UV-glue was applied to integrate and hermetically seal the patterned membrane with the auxiliary PMMA components. Release from the sacrificial substrate was based on capillary forces exerted by deionized water, supported by thermal cycling between room temperature and 80 degrees. Aqueous potassium chloride (KCl) electrolyte was pipetted into the detector reservoirs, and external Ag/AgCl electrodes were lowered into the reservoirs for performing the electrophysiological experiments.

Noise levels of the system setup, in the absence of pores, are about 5 pA, which is larger than best reported in literature, but sufficient for the envisioned proof-of-principle.

A theoretical model was applied to approximate the pore diameters exploiting the electrophoretic detector behavior. The model can also be used to precisely compare pore sizes with respect to each other. System verification was performed using silica nanospheres of 100 nm and 150 nm diameter as known test particles. Translocation through a 450 nm pore induced current blockades for about 1 ms with an amplitude of 30 pA to 55 pA for 100 nm particles and in excess of 70 pA for 150 nm particles. This is in close agreement with results obtained by the mathematical model.

The detectors can be used with either polarity, i.e. with reversible flow direction. They are stable over several months and can be re-used even after rinsing and drying. In these cases, open pore currents detected in the absence of nanoparticles vary by ±10-15%.

Biomolecules relevant to many life science applications, double-stranded DNA (dsDNA) and bovine serum albumin (BSA were analyzed to prove the device concept. Post-processed pores of 22 nm diameter were used at 600 mV driving voltage and 0.1 molar electrolyte in a slightly acidic regime of pH = 6. Statistical evaluations delivered typical current blockade amplitudes for complete translocations of dsDNA are I_{block} = 22 pA for a translocation time of t_D = 0.2 ms, and an almost threefold current blockade (I_{block} = 60 pA) and translocation time (t_D = 0.6 ms) for the larger BSA molecules, respectively. The detector can therefore be applied to identify different biomolecules simultaneously present in the electrolyte.

These results demonstrate the feasibility for an all-polymer detector system covering pores from sub-micrometer diameters to single-digit nanometers and fulfill the objectives of the

research as detailed in chapter 1.6. Biomedical detection applications were exemplified by discriminating between different populations of biomolecules.

Selected results obtained in this study have previously been published as refereed journal contributions:

- M. Hashemi, S. Achenbach, D. Klymyshyn, B. Moazed, J. Lee, "Design and Microfabrication of a Polymer Membrane-Based Submicron Scale Electrophoretic Flow Detector for Biomedical Applications," *Microsystems Technologies,* vol. 16(8), pp. 1563-1567, 2010.

- S. Achenbach, M. Hashemi, B. Moazed, D. Klymyshyn, "PMMA Polymer Membrane-Based Single Cylindrical Submicron Pores: Electrical Characterization and Investigation of Their Applicability in Resistive-Pulse Biomolecule Detection," *American Journal of Analytical Chemistry,* vol. 3(8), pp. 534-543, 2012.

- M. Hashemi, B. Moazed, S. Achenbach, D. Klymyshyn," Functional Analysis of Single PMMA-Based Submicron Pore Electrophoretic Flow Detectors via Translocation of Differently-Sized Silica Nanoparticle**s,"** *IET Nanobiotechnology,* vol. 6(4), pp. 149-155, 2012.

- S. Achenbach, M. Hashemi, B. Moazed, D. Klymyshyn, "Fabrication and Electrical Characterisation of an all-PMMA and PMMA/Lipid Bi-Layer Single Submicron Pore Electrophoretic Flow Detector for Biomedical Applications," *Microelectronic Engineering,* vol. 98, pp. 630-633, 2012.

- B. Moazed, M. Hashemi, S. Achenbach, "Novel PMMA Polymer-Based Nanopores Capable of Detection and Discrimination between Structurally-Different Biomolecules", *Accepted for publication in Sensors Journal, IEEE,* 2014.

6.2. Future Work

The following items should be considered to continue the current study and to more thoroughly investigate the subject:

- Based on the devices already fabricated, the fine structure analysis of translocation signals should be further validated to fully understand the events that contribute to, and impede, translocations, and to fully comprehend the effect of polymer membrane materials in electrophysiological investigations of biomolecules.
- Based on the preliminary fabrication sequence used so far, specialized electron beam lithography (EBL) equipment and process parameters should be applied to fully exploit the patterning capabilities of PMMA and directly tailor pore sizes to desired values, without the need for thermal post-processing. Elionix Inc., Tokyo, Japan [105], for example, is a manufacturer of high acceleration voltage electron beam writers. They have demonstrated 15 nm wide lines in 1.5 µm thick resist using a 125 kV writer.
- Applying optimized EBL equipment and parameters, avoiding reshaping the pore cross section in a reflow process, and verifying that thermal cycling for the final membrane release always remains well below the actual glass transition temperature, even if UV exposure is applied, can support improving the structure accuracy of the pores. Specifically, the sidewall profile might get enhanced and the discrepancy between nominal and actual pore diameters might get minimized.
- Once optimized pore dimensions and final system configurations have been determined for specific biomolecules, serial fabrication by EBL might get complemented by parallel nanofabrication approaches such as X-ray lithography and nano imprint lithography to increase the throughput and decrease device costs.

- Device functionality can significantly get improved by functionalizing the surfaces of the pores. Such functionalization can go beyond controlling the hydrophilicity and surface charges and extend to control the transport of biomolecules through nanopores in detail [106]. In [60], self-assembled monolayers (SAMs) are applied to potentially regulate the transport of DNA molecules. Similar approaches potentially allow to use nanopores for DNA sequencing [107].
- Functionalization of the pore surface could also be applied to change the paradigm from a volatile sensor to a permanent detector. Thiol linkages could affix antibodies to the pore. These antibodies are specific to certain biomolecules and could permanently capture them. This allows to be less dependent on the exact pore dimension, while increasing the selectivity for only one kind of biomolecules. In an ideal scenario, such a detector might be able to be sensitive enough to detect a single biomolecule in the electrolyte.
- A further change in the system concept would be to use several pores in parallel, fed from a common reservoir. Different pore sizes or surface functionalization would allow to screen for different molecules in the different branches of the device.

REFERENCES

[1] H. Basu, B. Feuerstein, D. Zarling, R. Shafer, and L. Marton, "Recognition of Z-RNA and Z-DNA determinants by polyamines in solution: experimental and theoretical studies," *Journal of Biomolecular Structure and Dynamics*, vol. 6, no. 2, pp. 299-309, 1988.

[2] A. Ghosh and M. Bansal, "A glossary of DNA structures from A to Z," *Acta Crystallographica D*, vol. 59, no. 4, pp. 620-626, 2003.

[3] D. Han, S. Pal, Y. Yang, S. Jiang, J. Nangreave, Y. Liu, and H. Yan, "DNA gridiron nano-structures based on four-arm junctions," *Science*, vol. 339, no. 6126, pp. 1412-1415, 2013.

[4] B. Alberts, A. Johnson, J. Lewis, M. Raff, K. Roberts, and P. Walter, *Molecular Biology of the Cell*. New York, NY: Garland Science, Forth ed., 2002.

[5] L. Brocchieri and S. Karlin, "Protein length in eukaryotic and prokaryotic proteomes,"*Nucleic Acids Research*, vol. 33, no. 10, pp. 3390-3400, 2005.

[6] W. H. Coulter, "Means for counting particles suspended in a fluid," *U. S. Patent 2,656,508*, 1953.

[7] Axopatch 200B, "Patch Clamp Theory and Operation," Axon Instruments, Inc. U.S.A, Copyright 1997-1999.

[8] D. J. Fologea, J. Uplinger, B. Thomas, D. S. McNabb, and J. Li, "Slowing DNA translocation in solid-state nanopore," *Nano Letters*, vol. 5, pp. 1734-1737, 2005.

[9] M. Rhee and M. A. Burns, "Nano-pore sequencing technology: nano-pore preparations,"*Science Direct*, vol. 25, pp. 174-181, 2007.

[10] J. J. Kasianowicz, E. Brandin, D. Branton, and D. W. Deamer, "Characterization of individual polynucleotide molecules using a membrane channel," *Proceedings of the National Academy of Sciences USA*, vol. 93, pp. 13770-13773, 1996.

[11] D. W. Deamer and M. Akeson, "Nano-pores and nucleic acids: prospects for ultra-rapid sequencing," *Trends in Biotechnology*, vol. 18, pp. 131-180, 2000.

[12] B. M. Venkatesan and R. Bashir, "Nanopore sensors for nucleic acid analysis," *Nature Nanotechnology*, vol. 6, pp. 615-624, 2011.

[13] L. Song, M. R. Hobaugh, C. Shustak, S. Cheley, H. Bayley, and E. Gouaux, "Structure of staphylococcal α-hemolysin, a heptameric transmembrane pore," *Science*, vol. 274, pp. 1859-1866, 1996.

[14] R. Stefureac, Y. T. Long, H. B. Kraatz, P. Howard, and J. S. Lee, "Transport of α-helical peptides through α-hemolysin and aerolysin pores," *Biochemistry*, vol. 45, pp. 9172-9179, 2006.

[15] X. F. Kang, L. Q. Gu, S. Cheley and H. Bayley, "Single protein pores containing molecular adapters at high temperatures," *Angewandte Chemie International Edition England*, vol. 44, no. 10, pp. 1495-1499, 2005.

[16] T. Z. Butler, M. Pavlenok, I. M. Derrington, M. Niederweis, and J. H. Gundlach, "Single-molecule DNA detection with an engineered MspA protein nanopore," *Proceedings of the National Academy of Sciences USA*, vol. 105, no. 52, pp. 20647-20652, 2008.

[17] F. Haque, J. Li, H. C. Wu, X. J. Liang, and P. Guo, "Solid-state and biological nanopore for real-time sensing of single chemical and sequencing of DNA," *Nano Today*, vol. 8, pp. 56-74, 2013.

[18] C. Dekker, "Solid-state nanopores," *Nature Nanotechnology*, vol. 2, pp. 209-215, 2007.

[19] I. M. Derrington, T. Z. Butler, M. D. Collins, E. Manrao, M. Pavlenok, M. Niederweis, and J. H. Gundluch, "Nanopore DNA sequencing with MspA," *National Academy of Sciences USA*, vol. 107, no. 37, pp. 16060-16065, 2010.

[20] J. Li, D. Stein, C. McMullan, D. Branton, M. J. Aziz, and J. A. Golovchenko, "Ion-beam sculpting at nanometer length scales," *Nature*, vol. 412, pp. 166-169, 2001.

[21] J. Li, M. Gershow, D. Stein, E. Brandin, and J. A. Golovchenko, "DNA molecules and configurations in a solid-state nanopore microscope," *Nature Materials*, vol. 2, pp. 611-615, 2003.

[22] A. J. Storm, J. H. Chen, H. W. Zandbergen, and C. Dekker, "Translocation of double-strand DNA through a silicon oxide nanopore," *Physical Review E Statistical Nonlinear and Soft Matter Physics*, vol. 71, pp. 051903-051913, 2005.

[23] U. F. Keyser, B. N. Koeleman, S. Van Dorp, D. Krapf, R. M. M. Smeets, S. G. Lemay, N. H. Dekker, and C. Dekker, "Direct force measurements on DNA in a solid-state nanopore,"*Nature Physics*, vol. 2, pp. 473-477, 2006.

[24] D. Fologea, B. Ledden, D. S. McNabb, and J. L. Li, "Electrical characterization of protein molecules by a solid-state nanopore," *Applied Physics Letters*, vol. 91, no. 5, pp. 053901-053903, 2007.

[25] D. S. Talaga and J. Li, "Single-molecule protein unfolding in solid-state nanopores," *Journal of the American Chemical Society*, vol. 131, pp. 9287-9297, 2009.

[26] R. M. M. Smeets, S. W. Kowalczyk, A. R. Hall, N. H. Dekker and C. Dekker, "Translocation of RecA-coated double-stranded DNA through solid-state nanopores," *Nano Letters*, vol. 9, pp. 3089-3095, 2009.

[27] S. Kowalczyk, M. Tuijtel, S. Donkers and C. Dekker, "Unraveling single-stranded DNA in a solid-state nanopore," *Nano Letters*, vol. 10, pp. 1414-1420, 2010.

[28] S. Garaj, W. Hubbard, A. Reina, J. Kong, D. Branton, and J. A. Golovchenko, "Graphene as a subnanometer trans-electrode membrane," *Nature*, vol. 467, pp. 190-193, 2010.

[29] R. Wei, V. Gatterdam, R. Wieneke, R. Tampe, and U. Rant, "Stochastic sensing of proteins with receptor-modified solid-state nanopores," *Nature Nanotechnology*, vol. 7, no. 4, pp. 257-263, 2012.

[30] N. T. Nguyen and S. T. Wereley, *Fundamentals and Applications of Microfluidics*. Artech House, first ed., 2002.

[31] D. Belder and M. Ludwig, "Surface modification in microchip electrophoresis," *Electrophoresis*, vol. 24, pp. 3595-3606, 2003.

[32] A. J. Storm, J. H. Chen, X. S. Ling, H. W. Zandbergen, and C. Dekker, "Fabrication of solid-state nanopores with single-nanometer precision," *Nature Materials*, vol. 2, pp. 537-540, 2003.

[33] L. Petrossian, S. J. Wilk, P. Joshi, S. Hihath, J. D. Posner, S. M. Goodnick, and T. J. Thornton, "High aspect ratio cylindrical nanopores in silicon-on-insulator substrates,"*Solid-State Electronics*, vol. 51, pp. 1391-1397, 2007.

[34] L. Petrossian, S. J. Wilk, P. Joshi, S. Hihath, S. M. Goodnick, and T. J. Thornton, "Fabrication of cylindrical nanopores and nanopore arrays in silicon-on-insulator substrates," *Journal of Microelectromechanical Systems*, vol. 16, no. 6, pp. 1419- 1428, 2007.

[35] H. Shadpour, M. Musyimi, J. Chen, and S. A. Soper, "Physicochemical properties of various polymer substrates and their effects on microchip electrophoresis performance," *Journal of Chromatography A*, vol. 111, no. 12, pp. 238-251, 2006.

[36] H. Becker and C. Gartner C, "Polymer microfabrication methods for microfluidic analytical Applications," *Electrophoresis*, vol. 21, pp. 12–26, 2000.

[37] H. Bi, S. Meng, Y. Li, K. Gao, Y. Chen, J. Kong, P. Yang, W. Zhong, and B. Liu, "Deposition of PEG onto PMMA microchannel surface to minimize nonspecific absorption," *Lab on a Chip*, vol. 6, pp. 769-775, 2006.

[38] J. M. Goddard and J. H. Hotchkiss, "Polymer surface modification for the attachment of bioactive compounds," *Progress in Polymer Science*, vol. 32, pp. 698-725, 2007.

[39] M. Madou, Fundumentals of microfabrication: The science of miniaturization. Boca Raton, FL: CRC Press, 2002.

[40] Z. Siwy, P. Apel, D. Dobrev, R. Neumann, R. Spohr, C. Trautmann and K. Voss, "Ion transport through asymmetric nanopores prepared by ion track etching," *Nuclear Instruments and Methods in Physics Research,* vol. 208, pp. 143–148, 2003.

[41] Z. Siwy, I. D. Kosinska, A. Fulinski and C. R. Martin, "Asymmetric diffusion through synthetic nanopores," *Physical Review Letters,* vol. 94, no.1-4, pp. 048102-048107, 2005.

[42] S. Achenbach, T. Mappes and J. Mohr, "Structure quality of high aspect ratio sub-micron polymer structures patterned at the electron storage ring," *Journal of Vacuum Science and Technology B,* vol. 22, pp. 1-6, 2004.

[43] T. Mappes, S. Achenbach and J. Mohr, "High resolution X-ray lithography for the production of polymer submicron structures with high aspect ratio," Thesis, *University of Karlsruhe, FZKA 7215*, ISSN 0947-8620, 2006.

[44] H. Schift, Nanoimprint Lithography, *Springer Handbook of Nanothechnology.* pp. 239-278, 2007.

[45] S. Wu, S. R. Park and X. S. Ling, "Lithography-free formation of nanopores in plastic membranes using laser heating," *Nano Letters,* vol. 6, no. 11, pp. 2571-2576, 2006.

[46] R. Von Mises, "Mechanik der festen korper in plastisch deformablen zustand," *Gottin. Nachr. Math. Phys.*, vol. 1, pp. 582-592.

[47] H. Chang, S. M. Iqbal, E. A. Stach, A. H. King, N. J. Zaluzec and R Bashir, "Fabrication and characterization of solid-state nanopores using a field emission scanning electron microscope," *Applied Physics Letters*, vol. 88, pp. 103109, 2006.

[48] E. A. Heins, Z. S. Siwy, L. A. Baker and C. R. Martin CR, "Detecting single porphyrin molecules in a conically shaped synthetic nanopore," *Nano Letters*, vol. 5, pp. 1824–1829, 2005.

[49] M. Hashemi, S. Achenbach, D. Klymyshyn, B. Moazed and J. Lee, "Design and microfabrication of a polymer membrane-based submicron scale electrophoretic flow detector for biomedical applications," *Microsystem Technology*, vol. 16, no. 8-9, pp. 1563-1567, 2010.

[50] B. Schiedt, K. Healy, A. P. Morrison, R. Neumann and Z. Siwy, "Transport of ions and biomolecules through single asymmetric nanopores in polymer films," *Nuclear Instruments and Methods in Physics Research*, vol. 236, pp. 109-116, 2005.

[51] J. C. Maxwell, *A Treatise on Electricity and Magnetism*. Oxford: Clarendon Press, third ed., 1904.

[52] R. W. Deblois and C. P. Bean, "Counting and sizing of submicron particles by the resistive pulse technique," *Review of Scientific Instruments*, vol. 41, pp. 909-915, 1970.

[53] S. Achenbach, M. Hashemi, B. Moazed and D. Klymyshyn, "PMMA polymer membrane-based single cylindrical submicron pores: Electrical characterization and investigation of their applicability in resistive-pulse biomolecule detection," *American Journal of Analytical Chemistry*, vol. 3, pp. *534*-543, 2012.

[54] M. Hashemi, B. Moazed, S. Achenbach and D. Klymyshyn, "Functional analysis of single PMMA-based submicron pore electrophoretic flow detectors via translocation of differently sized silica nanoparticles," *IET Nanobiotechnology*, vol. 6, no. 4, pp. 149-155, 2012.

[55] J. B. Edel and T. Albrecht, *Engineered Nanopores for Bioanalytical Applications*. William Andrew, Incorporated, 23rd ed., 2013.

[56] J. Schmidt, "Stochastic sensors," *Journal of Materials Chemistry*, vol. 15, pp. 831-840, 2005.

[57] H. Bayley and P. S. Cremer, "Stochastic sensors inspired by biology," *Nature*, vol. 413, pp. 226-230, 2001.

[58] N. Lion, T. C. Rohner, L. Dayon, I. L. Arnaud, E. Damoc, N. Youhnovski, Z. Wu, C. Roussel, J. Josserand, H. Jensen, J. S. Rossier, M. Przybylski, and H. H. Girault, "The role of microfluidic systems in proteomics," *Electrophoresis*, vol. 24, pp. 3533-3562, 2003.

[59] M. Galloway, W. Stryjewski, A. Henry, S. M. Ford, S. Liopis, R. L. McCarley, and S. A. Soper, "Contact conductivity detection in poly (methyl methacrylate)-based microfluidic devices for analysis of mono- and polyanionic molecules," *Analytical Chemistry*, vol. 74, pp. 2407-2415, 2002.

[60] D. Wang, S. Harrer, B. Luan, G. Stolovitzky, H. Peng, and A. A. Ardakani, "Regulating the transport of DNA through biofriendly nanochannels in a thin solid membrane," *Nature*, vol. 4, pp. 3985-3991, 2014.

[61] A. J. Rosenbloom, D. M. Sipe, Y. Shishkin, Y. Ke, R. P. Devaty and W. J. Choyke, "Biomems materials and fabrication technology: Nanoporous SiC: A candidate semi-permeable material for biomedical applications," *Biomedical Microdevices*, vol. 6, pp. 261-267, 2004.

[62] T. Burakowaski, T. Wierzchon, Surface Engineering of Metals: Principle, Equipment, Technologies. CRC Press, 1998.

[63] Nano PMMA and Copolymer, MICRO CHEM Company, 1245 Chestnut Street, Newton, MA 02464.

[64] P. Henzi, R. Truckenmuller, D. Hermann, S. Achenbach, U. Wallrabe and J. Mohr, "Bonding of LIGA PMMA Microstructures by UV Irradiation and Low Temperature Welding", *HARMST 5th Conference*, pp. 197-198, 2003.

[65] A. Meller, L. Nivon, E. Brandin, J. Golovchenko and D. Branton, "Rapid nanopore discrimination between single polynucleotide molecules," *Proceedings of the National Academy of Sciences USA*, vol. 97, pp. 1079-1084, 2000.

[66] M. Akeson, D. Branton, J. J. Kasianowicz, E. Brandin, and D. W. Deamer, "Microsecond time-scale discrimination among polycytidylic acid, polyadenylic acid, and polyuridylic acid as homopolymers or as segments within single RNA molecules," *Biophysical Journal*, vol. 77, pp. 3227-3233, 1999.

[67] A. R. Hall, A. Scott, D. Rotem, K. K. Mehta, H. Bayley and C. Dekker, "Hybrid pore Formation by directed insertion of alpha-haemolysin into solid-state nanopores," *Nature Nanotechnology*, vol. 5, pp. 874-877, 2010.

[68] A. Mara, Z. Siwy, C. Trautmann, J. Wan and F. Famme, "An asymmetric polymer nano-pore for single molecule detection," *Nano Letters*, vol. 4, pp. 497-501, 2004.

[69] S. O. Cho and H. Y. Jun, "Surface hardening of poly (methyl methacrylate) by electron Irradiation," *Nuclear Instruments and Methods in Physics Research B*, vol. 237, pp. 525-532, 2005.

[70] K. C. Khulbe, C. Feng and T. Matsuura, "The art of surface modification of synthetic polymeric membranes," *Journal of Applied Polymer Science*, vol. 115, pp. 855-895, 2010.

[71] C. Ho, R. Qiao, J. B. Heng, A. Chatterjee, R. J. Timp, N. R. Aluru, and G. Timp, "Electrolytic transport through a synthetic nanometer-diameter pore," *Proceedings of the National Academy of Sciences U S A*, vol. 102, pp. 10445-10450, 2005.

[72] R. M. M. Smeets, U. F. Keyser, D. Krapf, M. Y. Wu, N. H. Dekker and C. Dekker, "Salt dependence of ion transport and DNA translocation through solid-state nanopores," *Nano. Letters*, vol. 6, no. 1, pp. 89-95, 2006.

[73] Y. Choi, L. A. Baker, H. Hillebrenner and C. R. Martin, "Biosensing with conically shaped nanopores and nanotubes," *Physical Chemistry Chemical Physics*, vol. 8, pp. 4976-4988, 2006.

[74] L. T. Sexton, L. P. Horne, S. A. Sherrill, G. W. Bishop, L. A. Baker and C. R. Martin, "Resistive-pulse studies of proteins and protein/antibody complexes using a conical nanotube sensor," *Journal of the American Chemical Society*, vol. 1[32], pp. 13144-13152, 2007.

[75] Z. Siwy, Y. Gu, H. A. Spohr, D. Baur, A. Wolf-Rober, R. Spohr, P. Apel, and Y. E. Korchev, "Rectification and voltage gating of ion currents in a nanofabricated pore," *Europhysics Letters*, vol. 60, no. 3, pp. 349-355, 2002.

[76] Z. Siwy and A. Fulinski, "Fabrication of synthetic nanopore ion pump," *Physical Review Letters*, vol.89, no.19,pp. 198103-198107, 2002.

[77] J. Liu and M. L. Lee, "Permanent surface modification of polymeric capillary electrophoresis microchips for protein and peptide analysis," *Electrophoresis*, vol. 27, pp. 3533–3546, 2006.

[78] A. S. Prabhu, T. Z. N. Jubery, K. J. Freedman, R. Mulero, P. Dutta and M. J. Kim, "Chemically modified solid state nanopores for high throughput nanoparticle separation," *Journal of Physics: Condensed Matter*, vol. 22, pp. 454107-454116, 2010.

[79] H. Chang, F. Kosari, G. Andreadakis, M. A. Alam, G. Vasmatzis and R. Bashir, "DNA-mediated fluctuations in ionic current through silicon oxide nanopore channels," *Nano Letters*, vol. 4, pp. 1551-1556, 2004.

[80] M. Wanunu, J. Sutin, B. McNally, A. Chow and A. Meller, "DNA translocation governed by interactions with solid-state nanopores," *Biophysical Journal*, vol. 95, pp. 4716-4725, 2008.

[81] H. Peng and X. S. Ling, "Reverse DNA translocation through a solid-state nanopore by magnetic tweezers," *Nanotechnology*, vol. 20, pp. 185101-185109, 2009.

[82] L. J. Steinbock, O. Otto, C. Chirnerel, J. Gornall and U. F. Keyser, "Detecting DNA folding with nanocapillaries," *Nano Letters*, vol. 10, pp. 2493-2497, 2010.

[83] D. Fologea, "Detecting single-stranded DNA with a solid-state nanopore," *Nano Letters*, vol. 10, pp. 1905-1909, 2005.

[84] Q. Liu, H. Wu, L. Wu, X. Xie, J. Kong, X. Ye and L. Liu, "Voltage-driven translocation of DNA through a high throughput conical solid-state nanopore," *Public Library of Science One*, vol. 7, no. 9, pp. e46014-e46023, 2012.

[85] S. Bhattacharya, S. Nair and A. Chatterjee, "An accurate DNA sensing and diagnosis methodology using fabricated silicon nanopores," *IEEE Transactions on Circuits and Systems*, vol. 53, no. 11, pp. 2377-2383, 2006.

[86] J. B. Heng, C. Ho, T. Kim, R. Timp, A. Aksimentiev, Y. V. Grinkova, S. Sligar, K. Schulten and G. Timp, "Sizing DNA using a nanometer-diameter pore," *Biophysical Journal*, vol. 87, pp. 3205-3211, 2004.

[87] D. Stein, C. J. McMullan, J. Li and J. A. Golovchenko, "A feeback-controlled ion beam sculpting apparatus," *Review of Scientific Instruments*, vol. 75, pp. 900-905, 2004.

[88] J. Li and D. S. Talaga, "The distribution of DNA translocation times in solid-state nanopores," *Journal of Physics: Condensed Matter*, vol. 22, pp. 454129-454137, 2010.

[89] C. C. Harrell, Y. Choi, L. P. Horne, L. A. Baker, Z. S. Siwy and C. R. Martin, "Resistive-Pulse DNA detection with a conical nanopore sensor," *Langmuir*, vol. 22, pp. 10837-10843, 2006.

[90] P. Chen, G. Jiajun, E. Brandin, K. Young-Rok, Q. Wang and D. Branton, "Probing single DNA molecule transport using fabricated nanopores," *Nano Letters*, vol. 4, pp. 2323-2328, 2004.

[91] A. Meller, L. Nivon and D. Branton, "Voltage-driven DNA translocations through a nanopore," *Physical Review Letters*, vol. 86, pp. 3435-3438, 2001.

[92] M. Bates, M. Burns and A. Meller, "Dynamics of DNA molecules in a membrane channel probed by active control techniques," *Biophysical Journal*, vol. 84, pp. 2366-2372, 2003.

[93] B. Luan, G. Stoloviyzky and G. Martyna, "Slowing and controlling the translocation of DNA in a solid-state nanopore," *Nanoscale*, vol. 4, pp. 1068-1077, 2012.

[94] H. Y. He, M. Tsutsui, C. Fan, M. Taniguchi and T. Kawai, "Gate manipulation of DNA capture into nanopores," *American Chemical Society Nano*, vol. 5, pp. 8391–8397, 2011.

[95] A. Oukhaled, B. Cressiot, L. Bacri, M. Pastoriza-Gallego, J. M. Betton, E. Bourhis, R. Jede, J. Gierak, L. Auvray and J. Pelta, "Dynamics of completely unfolded and native

proteins through solid-state nanopores as a function of electric driving force," *American Chemical Society Nano*, vol. 5, no. 5, pp. 3628-3638, 2011.

[96] B. Cressiot, A. Oukhaled, G. Patriarche, M. Pastoriza-Gallego, J. M. Betton, L. Auvray, M. Muthukumar, L. Bacri and J. Pelta, "Protein transport through a narrow solid-state nanopore at high voltage: Experiments and theory," *American Chemical Society Nano*, vol. 6, no. 7, pp. 6236-6243, 2012.

[97] C. Fuss, J. C. Palmaz and E. A. Sprague, "Fibrinogen: structure, function, and surface interactions," *Journal of Vascular and International Radiology*, vol. 12, no. 6, pp. 677-682, 2001.

[98] A. Han, G. Schurmann, G. Mondin, R. A. Bitterli, N. G. Hegel-bach, N. F. de Rooij and U. Staufer, "Sensing protein molecules using nanofabricated pores," *Applied Physics Letters*, vol. 88, pp. 093901-093903, 2006.

[99] A. Han, M. Creus, G. Schuermann, V. Linder, T. R. Ward, N. F. de Rooij and U. Staufer, "Label-free detection of single protein molecules and protein-protein interactions using synthetic nanopores," *Analytical Chemistry*, vol. 80, pp. 4651-4658, 2008.

[100] L. T. Sexton, H. Mukaibo, P. Katria, H. Hess, S. A. Sherrill, L. P. Horne and C. R. Martin, "An adsorption-based model for pulse duration in resistive-pulse protein sensing," *Journal of the American Chemical Society*, vol. 132, pp. 6755-6763, 2010.

[101] D. J. Niedzwiecki, J. Grazul and L. Movileanu, "Single-molecule observation of protein adsorption onto an inorganic surface," *Journal of the American Chemical Society*, vol. 132, pp. 10816-10822, 2010.

[102] P. Roach, D. Farrar and C. C. Perry, "Interpretation of protein adsorption: Surface-induced conformational changes," *Journal of the American Chemical Society*, vol. 127, pp. 8168-8173, 2005.

[103] M. Firnkes, D. Pedone, J. Knezevic, M. Doblinger and U. Rant, "Electrically facilitated translocations of proteins through silicon nitride nanopores: Conjoint and competitive action of diffusion, electrophoresis, and electroosmosis", *Nano Letters*, vol. 10, pp. 2162-2167, 2010.

[104] U. F. Keyser, S. van Dorp and S. G. Lemay, "Tether forces in DNA electrophoresis," *Chemical Society Reviews*, vol. 39, pp. 939-947, 2010.

[105] Elionix, Inc., 3-7-6 Motoyokoyamacho Hachioji, Tokyo 192-0063, Japan, http://www.elionix.co.jp/english/products/ELSF100.html#ag.

[106] S. A. Soper, A. C. Henry, B. Vaidya, M. Galloway, M. Galloway, M. Wabuyele, "R. L. McCarley, "Surface modification of polymer-based microfluidic," *Analytica Chimica Acta, Elsevier*, vol. 470, pp. 87-99, 2002.

[107] B. Luan, and G. Stolovitzky, “An electro-hydrodynamics-based model for the ionic conductivity of solid state nanopores during DNA translocation,” *IOP Nanotechnology*, vol. 24, pp. 195702-195710, 2013.